

Fabian Sommer

**Thermal insulation of high confinement mode with dominant electron heating in comparison to dominant ion heating and corresponding changes of torque input**

**IPP 1/352  
November, 2013**

---

Thermal insulation of high confinement mode with dominant electron heating in comparison to dominant ion heating and corresponding changes of torque input

Fabian Sommer

---



München 2013



# Thermal insulation of high confinement mode with dominant electron heating in comparison to dominant ion heating and corresponding changes of torque input

Dissertation zur Erlangung des akademischen Grades eines  
**Doktors der Naturwissenschaften (Dr. rer. nat.)**  
an der Fakultät für Physik der Ludwig-Maximilians-Universität München

durchgeführt am  
Max-Planck-Institut für Plasmaphysik, Garching bei München

vorgelegt von  
**Fabian H. D. Sommer**  
geboren am 04.09.1983 in München

München, den 12. September 2013





Erstgutachter:	Prof. Dr. Hartmut Zohm
Zweitgutachter:	Prof. Dr. Gregor Morfill
Tag der mündlichen Prüfung:	23.10.2013

# Zusammenfassung

Die Verteilung der Leistung der Plasmaheizung auf Elektronen und Ionen wird von einer gemischten Elektronen- und Ionen Heizung, wie sie bei derzeitigen Fusionsexperimenten üblich ist, bei zukünftigen Experimenten und Reaktoren in eine dominante Elektronenheizung übergehen. Um gültige Vorhersagen für zukünftige Kraftwerke treffen zu können, müssen die dabei auftretenden Änderungen des Ansprechverhaltens und der Leistung der Plasmen erforscht und verstanden werden: Verhalten sich elektronengeheizte Plasmen systematisch unterschiedlich oder wird die Änderung der geheizten Spezies vollständig durch Wärmeaustausch von Elektronen zu Ionen kompensiert? Wie beeinflusst der Teilchentransport das Dichteprofil? Reduziert sich die Energieeinschlusszeit und das H-Mode Pedestal mit reduziertem Drehmoment Eintrag? Verändert sich der turbulente Transport grundlegend? Die spezifischen Eigenschaften des ECRH Systems an ASDEX Upgrade ermöglichen durch Austausch von NBI durch ECRH Leistung genaue Untersuchungen der Veränderungen der geheizten Spezies und geben damit den Hintergrund zur Diskussion dieser und anderer Fragen.

Bei niedrigen Heizleistungen und entsprechend hohen Kollisionsalitäten löst der Übergang von gemischter Elektronen- und Ionenheizung zu reiner Elektronenheizung so gut wie keine Verschlechterung der globalen Plasmaparameter und der Randwerte der kinetischen Profile aus. Die Elektronendichte zeigt bei steigender ECRH Leistung eine zunehmende zentrale Zuspitzung. Die zentrale Elektronentemperatur bleibt konstant, während die Iontemperatur leicht sinkt. Die toroidale Rotation nimmt mit abnehmender NBI Leistung ab, hat aber keinen Einfluss auf die Stabilität der Profile. Die Leistungsbilanz-Analyse zeigt einen großen Energieübertrag von Elektronen zu Ionen, sodass der Wärmefluss der Elektronen am Rand gegen Null absinkt, während der Wärmefluss der Ionen unabhängig von der Zusammensetzung der Heizung bleibt. Das Wärmediffusionsvermögen der Ionen dominiert gegenüber dem der Elektronen.

Für Entladungen mit hoher Heizleistung und entsprechend niedriger Kollisionsalität zeigen die globalen Plasmaparameter bei zunehmender Elektronenheizung einen leichten Rückgang. Das Dichteprofil zeigt eine starke, jedoch unveränderte Zuspitzung, wenn die Zusammensetzung der Heizung geändert wird. Das Profil der Elektronentemperatur ist unverändert, während die zentrale Iontemperatur bei zunehmendem ECRH Anteil signifikant abnimmt. Der relative Beitrag des Wärmeaustauschs ist kleiner, sodass die Elektronen immer noch einen bedeutenden Teil der Wärme am Rand transportieren. Der Wärmefluss der Ionen ist auch in diesem Fall unabhängig vom Heizungsmix und das Wärmediffusionsvermögen der Ionen überschreitet das der Elektronen.

Das radiale elektrische Feld zeigt keine Veränderung bei Änderung des Heizungsmix. Die Analyse der gesamten Datenbank von Entladungen zeigt bei zunehmendem  $T_e/T_i$  eine Verschlechterung des Gradienten der Iontemperatur und einen Anstieg bei zunehmendem Gradienten der toroidalen Rotation. Diese Ergebnisse ergänzen frühere Studien.

Die Elektronendichte und die Elektronen- und Iontemperaturen wurden mit Computercodes modelliert, die auf physikalischen Grundprinzipien basieren. Das angewandte Sägezahnmodell konnte die experimentellen Beobachtungen reproduzieren. Die Form der Profile, das sich ändernde  $T_e/T_i$  und die Zuspitzung der Dichte- und Temperaturprofile stimmen sehr gut mit den experimentellen Daten überein. Mithilfe linearer gyrokinetischer Berechnungen wurde die Iontemperaturgradienten-Mode als dominierender Kandidat für den Wärmetransport ermittelt. Die Berechnungen können die im Experiment beobachteten Phänomene erklären, z.B. den unterschiedlichen Anstieg des Ionenwärmeflusses oder die Dichtezuspitzung bei verschiedenen Kollisionsalitäten.

Die Ergebnisse, die in dieser Arbeit vorgestellt werden, zeigen ein einheitliches Bild der beobachteten Phänomene und das Verständnis der zugrunde liegenden Physik. Letztere waren Ausgangspunkt für die Entwicklung der eingestetzten Computercodes, die so eine zuverlässige Vorhersage der Leistung zukünftiger Fusionsreaktoren ermöglichen.



# Abstract

The ratio of heating power going to electrons and ions will undergo a transition from mixed electron and ion heating as it is in current fusion experiments to dominant electron heating in future experiments and reactors. In order to make valid projections towards future devices the connected changes in plasma response and performance are important to be study and understand: Do electron heated plasmas behave systematically different or is the change of heated species fully compensated by heat exchange from electrons to ions? How does particle transport influence the density profile? Is the energy confinement and the H-mode pedestal reduced with reduced torque input? Does the turbulent transport regime change fundamentally? The unique capabilities of the ECRH system at ASDEX Upgrade enable this change of heated species by replacing NBI with ECRH power and thereby offer the possibility to discuss these and other questions.

For low heating powers corresponding to high collisionalities the transition from mixed electron and ion heating to pure electron heating showed next to no degradation of the global plasma parameters and no change of the edge values of kinetic profiles. The electron density shows an increased central peaking with increased ECRH power. The central electron temperature stays constant while the ion temperature decreases slightly. The toroidal rotation decreases with reduced NBI fraction, but does not influence the profile stability. The power balance analysis shows a large energy transfer from electrons to ions, so that the electron heat flux approaches zero at the edge whereas the ion heat flux is independent of heating mix. The ion heat diffusivity exceeds the electron one.

For high power, low collisionality discharges global plasma parameters show a slight degradation with increasing electron heating. The density profile shows a strong peaking which remains unchanged when modifying the heating mix. The electron temperature profile is unchanged whereas the central ion temperature decreases significantly with increasing ECRH fraction. The relative contribution of the heat exchange is smaller so that the electrons still carry a substantial fraction of heat at the edge. The ion heat flux is still independent of the heating mix and the ion heat diffusivity exceeds the electron one.

The radial electrical field does not show any variation with changing heating mix. The analysis of the whole database of discharges shows a degradation of the ion temperature gradient with increasing  $T_e/T_i$  and a steepening with increasing gradient of the toroidal rotation. These findings complement previous studies.

The electron density, and the electron and ion temperatures were modelled with a first principle code. The applied sawtooth model could reproduce the experimental observations. The profile shapes, the changing  $T_e/T_i$  and the peaking of the density and temperature profiles agree very well with the experimental data. Linear gyrokinetic calculations found the ion temperature gradient mode to be the dominant candidate for heat transport. The investigations can explain the observed phenomena in the experiment, like the different degree of increase of ion heat flux or density peaking for various collisionalities.

The results presented in this work show a consistent picture of the observed phenomena and the understanding of the main underlying physics. They allow a correct implementation in the applied computer codes and a reliable prediction of the performance of future fusion devices.



# Contents

<b>1</b>	<b>Introduction</b>	<b>1</b>
1.1	Nuclear fusion . . . . .	1
1.2	Magnetic confinement . . . . .	4
1.3	H-mode, Edge Localized Modes and sawtooth crashes . . . . .	6
1.4	Confinement time and density limit . . . . .	9
1.5	Motivation for this thesis . . . . .	10
<b>2</b>	<b>Heat transport theory and description of computer codes</b>	<b>13</b>
2.1	Classical transport . . . . .	14
2.2	Neoclassical transport . . . . .	15
2.3	Turbulent transport . . . . .	18
2.4	ASTRA . . . . .	20
2.5	TGLF . . . . .	24
2.6	GS2 . . . . .	25
<b>3</b>	<b>Heating systems at ASDEX Upgrade</b>	<b>27</b>
3.1	Neutral beam injection . . . . .	28
3.2	Ion cyclotron resonance frequency heating . . . . .	32
3.3	Electron cyclotron resonance heating . . . . .	34
<b>4</b>	<b>Diagnostics of ASDEX Upgrade</b>	<b>39</b>
4.1	Electron cyclotron emission spectroscopy . . . . .	39
4.2	Thomson scattering . . . . .	41
4.3	Charge exchange recombination spectroscopy . . . . .	42
4.4	Lithium beam emission spectroscopy . . . . .	44
4.5	DCN interferometer . . . . .	44
4.6	Bolometry . . . . .	46
4.7	Integrated data analysis . . . . .	47

## CONTENTS

---

<b>5</b>	<b>Experimental observations</b>	<b>49</b>
5.1	Discharge design . . . . .	49
5.2	Discharge performance . . . . .	56
5.3	Profile behaviour including power balance analysis . . . . .	61
5.3.1	Sensitivity of the power balance analysis to temperatures . . . . .	68
5.3.2	Sensitivity of the power balance analysis to plasma radiation . . . . .	71
5.4	Radial electric field . . . . .	73
5.5	Correlations and dependencies . . . . .	76
<b>6</b>	<b>Modelling results</b>	<b>79</b>
6.1	Modelling of kinetic profiles . . . . .	79
6.1.1	Treatment of sawtooth oscillations . . . . .	80
6.1.2	Modelling of electron and ion temperatures . . . . .	82
6.1.3	Simultaneous temperature and electron density modelling . . . . .	84
6.1.4	Sensitivity of TGLF modelling to starting and boundary conditions . . . . .	86
6.1.5	Sensitivity of TGLF modelling to $E \times B$ shear . . . . .	89
6.2	Comparison of all modelled discharges with the experimental database . . . . .	90
6.3	Linear gyrokinetic calculations . . . . .	95
<b>7</b>	<b>Summary and conclusions</b>	<b>101</b>
<b>8</b>	<b>Outlook</b>	<b>105</b>
<b>A</b>	<b>ASDEX Upgrade</b>	<b>111</b>
<b>B</b>	<b>Torbeam graphical user interface</b>	<b>113</b>
<b>C</b>	<b>Bibliography</b>	<b>115</b>
<b>D</b>	<b>Abbreviations</b>	<b>125</b>

# Chapter 1

## Introduction

### 1.1 Nuclear fusion

During the last years the discussion has increased significantly of how to provide the growing population of at present over seven billion people worldwide in a sustainable way with their daily needs [1]. The destruction of the environment and the global warming by manmade emissions of green house gases is more and more acknowledged by individuals as well as governments around the world and leads to increasing regulations and intensified research in this field [2]. A very important task is the development of large scale energy sources, which can substitute the base load power plants of today. Mainly there are coal, gas and nuclear power plants which have a huge footprint in the environment by CO<sub>2</sub> emission or the necessity of safe storage of the nuclear waste for 10 000 to 1 000 000 years [3].

The further development and optimisation of renewable energies such as solar energy and wind or water power will definitely play an important role in the energy mix of the future. However, the energy from these sources is subject to a high degree of natural fluctuations of the weather within days or hours, so that a stable and reliable energy supply is very difficult to implement. To achieve this goal a huge amount of further research and development in grid and storage technologies is necessary. Nevertheless, renewable energy sources remain appropriate and valuable for niches and will definitely supply part of the total energy demand in the future.

One attractive candidate to contribute to the future power mix is fusion energy. Fusion is appealing for several reasons: It causes practically zero emission, uses cheap and virtually inexhaustible fuel supplies and leaves a significantly reduced amount of radioactive waste behind compared to fission. This especially counts for radioactive elements with long life



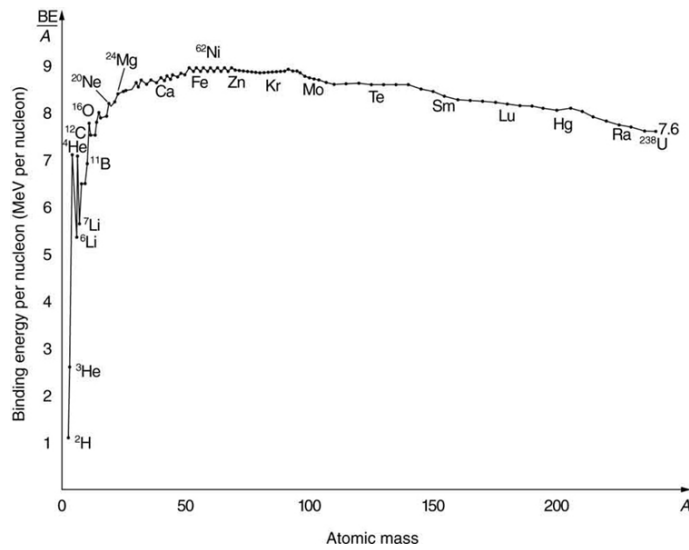
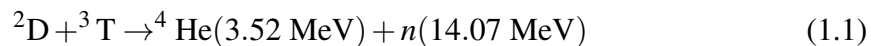


**Figure 1.1:** Binding energy per nucleon in MeV depending on the atomic mass [5].

times, so that the safe storage of radioactive structural material is reduced to maximum 100 years [4]. This is still a long time, but roughly 3 orders of magnitude less than in fission. A safe storage can be guaranteed for this period of time with immense increased probability.

In fusion a similar mechanism is used as in fission reactors nowadays, namely the varying binding energy per nucleon with the atomic mass (see figure 1.1). In contrast to nuclear fission, which releases energy by splitting heavy elements (usually Uranium) into medium heavy ones, energy is produced by fusing isotopes of the lightest element hydrogen into helium. It has been found that the fusion of deuterium and tritium, the two heavy isotopes of hydrogen, is the most suitable reaction. The cross section of their fusion process exceeds the reactions of other isotopes by one to two orders of magnitude, especially in the range of temperature achievable in fusion, which is a few  $10 \text{ keV}^1$ . One fusion reaction of a deuterium with a tritium atom releases 17,59 MeV, which is distributed among the fusion products helium and neutron according to their inverse masses [6]:



Since the binding energy depends on the atomic weight, this fusion reaction releases about five times more energy per gross fuel mass than fission of Uranium. Since uranium fuel rods are enriched with  ${}^{235}\text{U}$  only by about 2 % the energy production by fusion is larger by a factor of 200 compared to fission.

The outstanding advantages of fusion are the following:

- Deuterium is available in bound form in almost unlimited quantities in the water of our oceans and does not have to be recovered from ore and enriched like uranium

<sup>1</sup>1 keV  $\approx$  11 600 K

at high cost. Tritium can be bred from lithium with neutrons produced in the fusion reaction.

- Both deuterium as fuel and helium as ash do not bear any health hazards. Only tritium is radioactive, but can be bred directly in the reactor. Moreover, tritium has a half life of only 12.3 years. Hence its radioactivity subsides far earlier than the radioactivity from starting substances and end products of fission.
- The reactants only merge if they collide with a sufficient high energy and no chain reaction is employed to maintain the energy production. This difference in the central concept of fusion reactors compared to fission reactors provides a much higher level of inherent safety. Besides the strong reduction of storage time of the radioactive waste and the global availability of fuel, this is the fundamental advantage of a fusion reactor.

For the fusion of hydrogen both reactants have to overcome their Coulomb barrier of 415 keV. Although this is favoured by the tunnel effect, the hydrogen gas has to be heated to temperatures at which the atoms in the Maxwell tail have sufficient energy to do so (a few 10 keV). Hereby the fourth state of matter, a plasma, is reached in which the electrons are not bound to the nuclei, but move independently of them. Due to its very high temperature, a plasma cannot be held in conventional containers, but has to be confined by other means. Basically two methods exist to do so and to obtain energy through nuclear fusion:

- Inertial fusion  
One method is inertial fusion, which is explored e.g. at Laser Megajoule (LMJ) near Bordeaux, France [7] and at the National Ignition Facility (NIF) in Livermore, USA [8]. This method is based on irradiating a deuterium/tritium pellet of a few milligrams extremely homogeneously and heating it up to such high temperature with high power laser light or heavy ion beams that the outer shell is ablated explosively. Due to conserved inertia the centre is compressed and heated and fuses comparable to a small hydrogen bomb. This research is not solely oriented to energy production. The military has an interest to test its computer codes for nuclear bombs by means of the experimental results of inertial confinement fusion.
- Magnetic confinement  
The other method is the confinement of a deuterium/tritium plasma applying an appropriate magnetic field. A toroidal field structure is applied by external coils, which incorporates the plasma and separates it from the plasma facing walls. Devices with a toroidal symmetry and planar field coils are called tokamak. This concept, which experiences the largest progress between all fusion machine designs, is also employed at ASDEX Upgrade in Garching, Germany [9].

## 1.2 Magnetic confinement

The following sections follow the descriptions in [6, 10, 11]. The fundamental confinement concept of magnetic fusion is the gyration of electrons and ionised atoms around magnetic field lines as a result of the Lorenz force:

$$\vec{F}_L = q \cdot (\vec{v} \times \vec{B}) \quad (1.2)$$

$q$  stands for the charge of the particle,  $\vec{v}$  for the velocity,  $\vec{B}$  for the magnetic field vector. The resulting force is perpendicular to the magnetic field. The resulting frequency is called cyclotron frequency:

$$\omega_c = \frac{q \cdot B}{m} \quad (1.3)$$

$m$  stands for the mass of the considered particle. The radius of the gyration, which is called Larmor radius, is defined as the fraction of the perpendicular thermal velocity  $v_\perp$  and the cyclotron frequency:

$$r_L = \frac{v_\perp}{\omega_c} = \frac{m \cdot v_\perp}{|q| \cdot B} \quad (1.4)$$

The Larmor radius of electrons and ions is also denoted as  $\rho_e$  and  $\rho_i$ . For typical values in magnetic confinement experiments the ion cyclotron frequency lies in the range of a few 10 MHz. The ion Larmor radius lies in the range of a few mm for magnetic fields of a few Tesla, which are typically applied in fusion research. For electrons  $\omega_c$  lies around 100 GHz while  $r_L$  lies in the range of a few 10  $\mu\text{m}$ . Assuming a homogeneous and linear magnetic field the particles are trapped perpendicular to the field lines, but the particle losses at the ends of such a device would be tremendous.

One possibility to reduce these end-losses is to narrow the magnetic field at both ends of the linear device and to introduce in such a way a magnetic mirror. By increasing the magnetic field strength at both ends of the linear device, the parallel motion  $v_\parallel$  is transferred into perpendicular motion, since the magnetic moment  $\mu$  remains an invariant:

$$\mu = \frac{m \cdot v_\perp^2}{2B} \quad (1.5)$$

Additionally the total energy conservation applies:  $\frac{1}{2}m \cdot v^2 = \frac{1}{2}m(v_\perp^2 + v_\parallel^2) = \text{const}$ . If the parallel energy is small enough, the parallel velocity  $v_\parallel$  approaches zero and the particle is reflected. Particles with large parallel energies are still lost. The velocity space at large parallel velocities is filled continuously by collisions of particles with high total energy but small parallel velocity. Accordingly, this configuration too results in large particle losses as well as large energy losses at the ends. In addition turbulent transport can play a significant role, e.g. thermally excited magnetostatic modes for the electron heat transport which can even exceed the classical transport and the end losses [12]. Therefore its use as an energy producing device is not applicable.

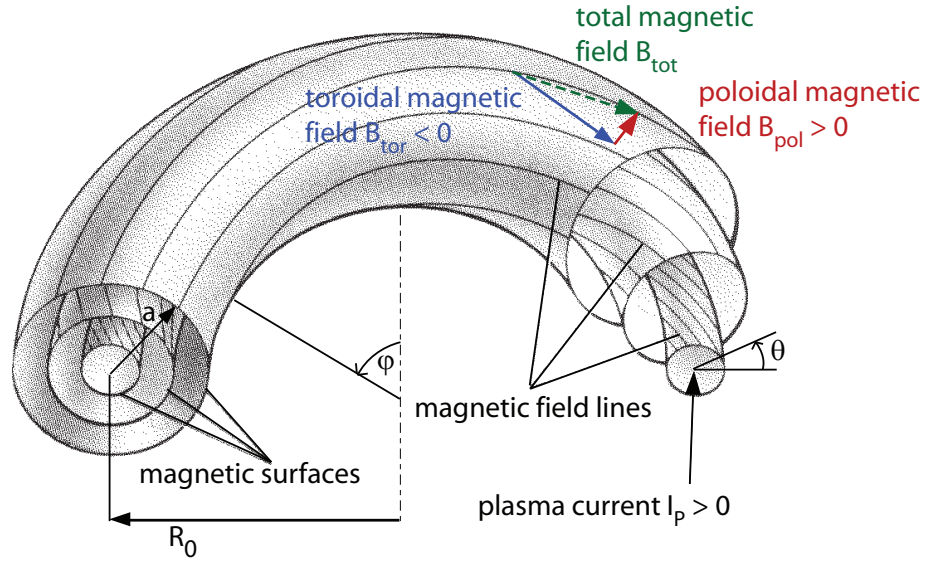


**Figure 1.2:** Magnetic field structure, definition of the toroidal ( $\varphi$ ) and poloidal ( $\theta$ ) angles and typical orientations of the plasma current  $I_p > 0$  and the toroidal magnetic field  $B_t < 0$  at ASDEX Upgrade.

To avoid the parallel losses at the ends of such devices, the magnetic structure can be bent into a toroidal form (plasma ring) in which all magnetic field lines are closed in themselves. The resulting structure is called a tokamak (**T**oroidal**n**aja **K**amera ss **M**agnitnimi **K**atuschkami is the Russian term for "toroidal chamber with magnetic coils" [13]) for toroidal symmetric geometry and planar field coils. The bending of the magnetic field lines causes several additional effects: The resulting radial decay of the toroidal magnetic field ( $B_t = B_0 \frac{R_0}{R}$ ) produces a vertical charge separation due to  $\nabla B \times \vec{B}$  drift, which is charge dependent. The resulting vertical electric field entails a radial particle transport due to  $\vec{E} \times \vec{B}$  drift, which leads to a loss of confinement if no further measures are taken. To avoid these losses a toroidal current is applied in tokamaks introducing a poloidal magnetic field component. Superposed to the externally applied toroidal magnetic field it results in a helical magnetic field structure in which only field lines lying on rational surfaces close in themselves. This configuration shortcuts the upper and lower parts of the plasma lying on the same magnetic surface. Due to this helical structure potential differences between upper and lower part of the plasma along the magnetic field lines can be balanced force free, so that no noteworthy  $\vec{E} \times \vec{B}$  drift occurs.

The plasma current is flowing in the entire plasma cross section resulting in a radially increasing poloidal magnetic field. This leads to nested flux surfaces with decreasing angle between the magnetic field lines and the horizontal plane towards the edge, the so called pitch angle. The magnetic field structure is shown in figure 1.2 together with the definitions of the major and the minor radius  $R_0$  and  $a$  and the toroidal and poloidal angles  $\varphi$  and  $\theta$ . Also the typical orientations of the plasma current  $I_p > 0$  and the toroidal magnetic field  $B_t < 0$  at ASDEX Upgrade are displayed. This layout produces a left handed system with toroidal and poloidal mode numbers  $n$  and  $m$ . For a better comparison of results of different devices but also between diagnostics at different poloidal angles the

radial variable

$$\rho_{tor} = \sqrt{\frac{\Phi - \Phi_a}{\Phi_s - \Phi_a}} \quad (1.6)$$

is introduced to map all radial dependent quantities on a common grid.  $\Phi$  denominates the toroidal magnetic flux while the index  $a$  stands for the axis and  $s$  for the separatrix. The Separatrix represents the last closed flux surface separating the confined plasma from the region intersecting with the walls.

The safety factor  $q$  is introduced as quantity describing the stability of the plasma against magneto hydrodynamic (MHD) modes [6]. For a circular tokamak with a large aspect ratio of major to minor radius  $A = R_0/a$  it can be approximated as:

$$q = \frac{r \cdot B_\varphi}{R \cdot B_\theta} \quad (1.7)$$

### 1.3 H-mode, Edge Localized Modes and sawtooth crashes

The first step to obtain a plasma in a tokamak is to induce a strong current inside the pre-ionised gas inside the torus via the central solenoid. The Ohmic losses by the finite resistance of the gas heat it to up to typically 1 to 2 keV. The Low Confinement Mode (L-mode) is formed, which has an electron pressure profile ( $p_e \propto T_e \cdot n_e$ ) shown in figure 1.3 (a). In this plasma state both the particle and the energy confinement are not sufficient enough for profitable energy production, hence its name. Targeted shaping of the magnetic structure changes the plasma from a circular into an elliptic cross section, which enhances the stability of microturbulences at the edge and leads to a better confinement of the plasma.

Further shaping can introduce a magnetic null, typically at the bottom, called the X-point. At this point the pitch of the magnetic field lines approaches zero asymptotical. Field lines further outside are not closed but intersect with a special plasma facing component (PFC) in the lower part of the device, the divertor. The vessel structures including the divertor and the magnetic cross section of a typical ASDEX Upgrade discharge can be seen in figure 1.3 (b). Due to this magnetic field structure the boundary of the confined plasma region is not a physical limiter, but the last closed flux surface, also called separatrix. It separates the inner, confined part of the plasma from the outer part, which has contact to the walls. By this measure the region of interaction between the plasma and the plasma facing components can be located further away from the plasma. This results in a highly reduced impurity influx from the walls into the plasma and improved energy and particle confinement in the edge region, since the connection length between confined plasma and walls is raised considerably.

The conductance of the plasma increases with  $T_e^{3/2}$ . This leads to a decreasingly efficient heating of the plasma by Ohmic losses of the plasma current. Therefore additional heat-

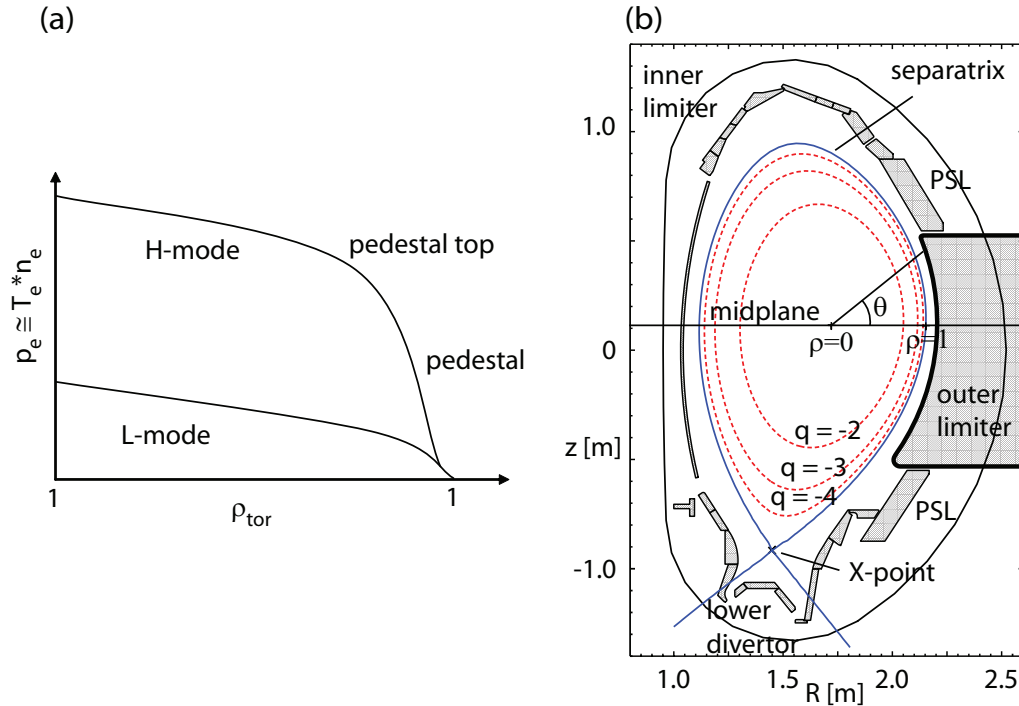


**Figure 1.3:** Plot (a): schematic comparison of pressure profiles of L-mode and H-mode. Plot (b): cross section of the vacuum vessel of ASDEX Upgrade including plasma facing components and a typical plasma equilibrium with X-point and rational  $q$ -surfaces.

ing by auxiliary systems is needed e.g. neutral beam injection (NBI, see chapter 3.1), ion cyclotron resonance heating (ICRH, see chapter 3.2) or electron cyclotron resonance heating (ECRH see chapter 3.3). Their application also allows to reach the High confinement mode (H-mode). Directly inside the separatrix a localised transport barrier is formed of a width of only a few cm in which the turbulent transport (see chapter 2.3) is suppressed. One possible candidate for this effect is perpendicular flow shear generated for example by differential perpendicular rotation [14]. The strongly reduced particle and heat transport allows significantly larger temperature and density gradients in this small region, resulting in high pressure gradient. The increased pedestal values shift the entire central density and temperature profiles upwards via stiffness leading to a significantly improved particle and energy confinement. Stiffness describes the resilience of especially the temperature profiles to changes when changing the heating power. Additional heating power mainly increases the heat flux and not so much the normalised gradients of the temperatures. This edge structure is called pedestal, see figure 1.3 (a).

The high edge pressure gradient and the large current density of the bootstrap current (see chapter 2.2) at the edge drive a severe plasma instability, the Edge Localised Mode (ELM) [15]. The edge gradients collapse, the high particle and energy confinement disappears for a short time and large amounts of particles and energy are expelled from the confined region in a few milliseconds. The expelled energy is typical in the range of 10 % of the stored energy but can reach up to 30 % of that in extreme situations. Following a crash the gradients recover until the stability limit is reached again and the next ELM occurs



typically about 5 to 50 ms later at ASDEX Upgrade. The ELM frequency increases with the energy flux through the separatrix. Following the field lines the expelled plasma intersects with the divertor material in a narrow region, which produces high heat loads on the PFCs in the order of a several MW/m<sup>2</sup>. In experiments nowadays typical the structural materials do not suffer from melting, since the time averaged heat fluxes are well below the material limits of the order of 10 MW/m<sup>2</sup> [16]. For future devices like ITER (International Thermonuclear Experimental Reactor, [17–19]) or DEMO (DEMONstration power plant, [20]) ways have to be found to avoid or mitigate ELMs.

In the current understanding the ELM crash is triggered by a current and pressure gradient driven MHD mode, a so called peeling-ballooning instability. In this peeling-ballooning model [21, 22] the pressure gradient is limited by high- $n$  ballooning modes [23]. The ELM is destabilised when the current density, mainly consisting of the bootstrap current, exceeds the critical value and low- $n$  external peeling modes occur. They limit the maximum pressure gradient in the pedestal and thereby the maximum achievable density and temperature values in the entire plasma. The experimental findings of the pressure at the pedestal top are close to the stability limits predicted by theory, but the crash itself cannot yet be described in its full complexity. Thus in the greater part of this work, only the stable inter ELM phases are considered and analysed.

Additionally to the ELM crash, which is affecting the edge of the plasma, also an instability in the core of the plasma was present in most of the analysed discharges, the so called sawtooth oscillation. This instability is an internal kink mode with the mode numbers  $m = 1$  and  $n = 1$ . It flattens peaked temperature and density profiles due to a redistribution of plasma. The sawtooth frequency typically ranges from 10 to 100 Hz while the central temperature can drop by up to 40 %. The density is not affected greatly, since its profiles are typically flat in the centre.

For a better comparison of the experimental data from phases with different heating mix a reduction of the sawtooth influence on the kinetic profiles would have been desirable. One possible option to achieve this is an increase of the frequency of the sawtooth oscillation and thus a decrease of their amplitude. Another possibility is a decrease of their frequency (ideally stabilising them entirely) and thus obtaining stable, equilibrated conditions between two crashes. Possible techniques include modifications of the  $q$ -profile by additional current drive of the ECCD or in exotic operation modes like improved H-modes or high  $q$ -scenarios. However, these measures depend crucially on the choice of heating systems, especially on the amount of tailored current drive by ECRH. A specific set of ECRH injection angles is mandatory for that hence it does not allow the variation of the heating mix from dominant NBI to dominant ECRH heating. Since exactly this should be performed in this work, no attempt could be made to reduce the influence of sawtooth oscillations. On the contrary, an operation mode of the ECRH was chosen which has as little as possible impact on the sawtooth behaviour.

## 1.4 Confinement time and density limit

One important quantity for fusion reactors is the condition for ignition which leads to the triple product for fusion. This condition is met if the energy loss is equal to  $1/5$  of the fusion power, since  $4/5$  of  $P_{fusion}$  is lost to the plasma by neutrons. The fusion and loss powers are given by

$$P_{fusion} = 0.2 \frac{n_{DT}^2}{4} \langle \sigma v \rangle_{DT} \cdot Q_{DT} \cdot V; \quad P_{loss} = 3/2 \frac{(n_e + n_{DT}) k \cdot T_i}{\tau_E} V \quad (1.8)$$

$n_{DT}$  stands for the deuterium-tritium mix density. The quasi neutrality of the plasma leads to  $n_e = n_{DT}$ . The reaction rate  $\langle \sigma v \rangle$  is proportional to  $T_i^2$  in the considered temperature range of a few 10 keV, which leads to  $P_{fusion} \propto n_e^2 T_i^2$ . Together with the loss power the triple product  $n_i \cdot T_i \cdot \tau_E$  can be defined, which has to exceed  $5 \times 10^{21} \text{m}^{-3} \text{keVs}$  for plasma ignition. Since the temperature is fixed to values above 10 keV the product  $n_e \cdot \tau_E$  is determined as well. The pressure  $n_e \cdot T_i$  can be seen as a free parameter, if the energy confinement time  $\tau_E$  is modified accordingly. This leads to the two concepts of fusion power production:

1. Very short confinement times with huge densities in inertia confinement fusion:  
 $\tau_E \approx 10^{-10} \text{s}; n_e \approx 10^{31} \text{m}^{-3}$
2. Moderate pressure with considerable confinement times in magnetic fusion:  
 $\tau_E \approx 5 \text{s}; n_e \approx 10^{21} \text{m}^{-3}$

The experimentally achievable steady state density is limited by the phenomenological Greenwald density [24]:

$$n_{e,GW} = \frac{I_p}{\pi \cdot a^2}; \quad n_{e,GW} [10^{20} \text{m}^{-3}], I_p [\text{MA}], a [\text{m}] \quad (1.9)$$

The plasma typically disrupts when the line integrated density exceeds the Greenwald limit. However, recent studies presented in [25] show the accessibility of a peaked high density regime exceeding this limit by a factor of 1.6 in the core with pellet injection. The discharge remains stable and is not terminated. Since the pedestal electron density profile remains unchanged the Greenwald limit is likely connected to the edge values of the electron density or its gradient. However, the physical mechanism behind this limit is not yet fully understood.



## 1.5 Motivation for this thesis

In present day experiments the heating deposition is usually equally distributed between electrons and ions. For high performance plasmas it is even dominantly going to the ion channel [26]. In future experiments and power producing fusion reactors like ITER and DEMO this will change towards dominant electron heating. However, the experimental basis of the influence of this change on the plasma performance is very limited caused by the lesser development of the heating systems delivering energy only or mainly to the electrons compared to the ones mainly heating the ions. In this study a systematic characterisation of the influence of the heated species on the plasma is performed. It was made possible by the recent upgrade of the ECRH system at ASDEX Upgrade.

Nowadays the workhorse of plasma heating is typically the NBI or ICRH system (see chapter 3.1 and 3.2). Both methods heat roughly half the ions and half the electrons, depending on plasma condition and applied heating scenario. However, in future the fraction of electron heating will grow considerably and dominate the heating power. The main reasons are:

1. The beam energy of NBI systems will increase to values in the range of 1 MeV to reach the inner part of the plasma for heating and current drive. Due to a larger minor radius of future devices, currently operating low voltage beams would be attenuated entirely in the outer region of the plasma. This fast decay would prevent central power deposition and make it difficult to reach sufficient temperature and density conditions in the core of the plasma. However, this objective is absolutely necessary for power plants or even successful operation of next step devices, so the application of high voltage NBI beams is inevitable. The large increase of beam energy will lead to a growth of the fraction between  $E_{beam}$  and  $E_{crit} \approx 18.6 T_e$ . As a result the cross sections for energy transfer from fast ions to electrons and ions will change in such a way, that the fraction of electron heating will increase significantly (see section 3.1).
2. The contribution of  $\alpha$ -particle heating due to fusion reactions of D and T to the overall heating composition will increase significantly. The fast helium nuclei have a birth energy of 3.52 MeV and heat the electrons even more than the NBI with increased beam energies. Simple calculations presented in figure 3.3 of chapter 3.1 show that the direct heating fraction of electrons by  $\alpha$ -particles assuming volume averaged electron temperatures of 10 keV in ITER [6] lies in the range of 95 %.
3. The ECRH is an option, which is currently under discussion as the main heating system for future devices like ITER. Besides the lower ECCD current drive efficiency compared to other heating systems (NBI, lower hybrid) ECRH has several convincing benefits: The development progress in recent years lead to gyrotrons reaching now 1 MW in steady state and 2 MW in pulsed operation. Current developments are going towards 2 MW in steady state operation. Compared to the other heating methods, the localised and well controllable energy and current deposition,

the small space required in the vacuum vessel ports, the high flexibility by steerable front ends and the higher wall plug efficiency are strong arguments to enhance the use of ECRH.

As it is outlined above the transition from partly ion heating to dominant electron heating in the near future is inevitable. However, resulting from the principles of heating systems commonly still used today, not many studies investigating the influence of the heating systems on the plasma could be executed (e.g. [26–28]). Therefore relevant data on this subject have been rare. Yet the progress of development in design and construction of gyrotrons in recent years allows from that time onward experiments with a relevant amount of electron heating. For that reason the experimental basis of dominant electron heated plasmas is still limited. The upgrade of the old ECRH system at ASDEX Upgrade, which delivers 2 MW for 1 s was started in 2007 but finished only during the conduction of the experiments for this work. Step by step 4 additional gyrotrons were installed in the last years, each delivering 1 MW heating power for 10 s. After this upgrade the routinely achieved peak power inside the plasma is 4 MW and allows a detailed analysis of dominant electron heated discharges with high heating powers for the first time. The results of this analysis are reported in this thesis.

"The experimental base on pedestal parameters is specifically poor for heating method alternative to NBI" [29]. This statement was made by a study group (AG-2) in 2010 which had the task to consider the heating mix of ITER. It shows precisely the importance of extending the experimental basis and increase the theoretical understanding of dominantly electron heated discharges and summarises the motivation for this thesis in one sentence.

The fusion triple product contains the ion temperature as one of the key quantities to reach an ignited plasma, and not the electron temperature. Furthermore the distribution of heat to electron and ion channel is determined by the combination of turbulent transport and heat exchange due to Coulomb collisions between the two channels. Therefore the understanding of the interplay of these mechanisms during electron heating dominated discharges is important. In addition the reduction of the torque input by the replacement of neutral beams will lead to a reduced rotation of the entire plasma. The analysis of the change of the electric field at the edge and a possibly accompanying degradation of the pedestal is also covered in this work.

This thesis, describing the studies about the influence of the heating mix on the plasma is structured as follows:

Chapter 2 contains the theoretical background of radial heat transport in a tokamak and an overview of the used codes. The classical transport, neoclassical transport and turbulent transport are presented and an introduction to the codes ASTRA, TGLF and GS2 is given. Chapter 3 specifies the heating systems. The diagnostics at ASDEX Upgrade and their impact respectively their special requirements with regard to the performed experiments and analysis are presented in chapter 4. Chapter 5 presents the experimental observations obtained during this work before the modelling results are shown in chapter 6. The summary and conclusion of the observed experimental phenomena and the modelling is given

## CHAPTER 1. INTRODUCTION

---

in chapter 7. The work is concluded with an outlook to future work in the last chapter 8. In the end the appendix presents the tokamak ASDEX Upgrade, of which the data of this theses were recorded (appendix A) and an introduction to the GUI for Torbeam calculation, which was developed for this thesis (appendix B). In the very end the bibliography (appendix C) and the used abbreviations (appendix D) are given.

## Chapter 2

# Heat transport theory and description of computer codes

This chapter follows the descriptions in [6, 10, 11]. For the ignition of a fusion reactor the fusion triple product  $n_i \cdot T_i \cdot \tau_E$  has to be greater than  $5 \times 10^{21} \text{m}^{-3} \text{keVs}$ . The expected central peak temperatures are typically 5 orders of magnitude larger than the tolerable limits of the vessel materials. The understanding and prediction of the radial particle and heat transport is essential to design the size and structure of a fusion device correctly. Various mechanisms of particle and heat transport in a plasma were identified in a tokamak. Since they are inevitable they limit the performance of the discharges and determine the size of the plasma chamber. The standard description of transport in a plasma comprises two terms. Here the formula for particle transport is given, but a similar structure applies for heat transport as well:

$$\vec{\Gamma} = -D\nabla n + n\vec{v} \quad (2.1)$$

$\vec{\Gamma}$  stands for the particle flux and  $D$  for the diffusion coefficient. The first term depicts diffusion, which is proportional to the gradient of the considered quantity  $\nabla n$ . The second term describes the transport due to a finite velocity  $\vec{v}$  of the considered quantity  $n$ . For heat transport the second term is usually considered to be not relevant, whereas for particle transport a so called particle pinch is regularly observed. See reference [30] for more details on particle transport. In general the transport along field lines is almost force free in a fusion plasma, since the thermal conductivity increases with temperature ( $\kappa_e \propto T^{5/2}$ ). Only a small magnetic force  $\nabla B$  acts upon the particles parallel to the field. No considerable gradients of temperature and density can be built up in that direction.

The transport in a plasma device can be divided up into three categories:

- Classical transport
- Neoclassical transport
- Turbulent transport

The classical transport (see chapter 2.1) is produced by collisions in the absence of any inhomogeneity of the magnetic field. It can be described by a simple collisional model assuming a homogenous magnetic field. The neoclassical transport (see chapter 2.2) is the additional transport produced by collisions in the presence of the inhomogeneous magnetic field of toroidal fusion devices e.g. tokamak. It can be described by a collisional model including in addition all drifts and phenomena arising from a radially decaying magnetic field in toroidal geometry. The turbulent transport deals with fluxes arising from various incoherent micro fluctuations in tokamak geometry. In general the turbulent transport (see chapter 2.3) is the main contributor to the radial transport of heat and particles. In the following the term transport always denotes radial transport perpendicular to the magnetic field lines. The parallel transport is typically a factor  $10^{12}$  to  $10^{13}$  larger than turbulent perpendicular transport for typical plasma parameters of  $T_e \approx 10 \text{ keV}$ ,  $n_e \approx 10^{20} \text{ m}^{-3}$ .

In the course of this work, several codes were used to analyse and model the experimental data in order to compare them with the present theory: ASTRA (see chapter 2.4) is used to perform power balance analysis and as a framework for the temperature and density modelling. TGLF (see chapter 2.5) is used to model the electron and ion temperature and electron density profiles according to the current understanding of turbulent transport to test these models and possibly to find its limitations in the experimental space covered by the investigations of this thesis. GS2 (see chapter 2.6) is used to calculate the most unstable microinstability responsible for the radial heat transport.

## 2.1 Classical transport

No considerable density or temperature gradients can be built up in lab plasmas without confining magnetic field due to an increase of particle and thermal conductivity with temperature. The same holds for linear and homogeneous magnetised plasmas along the field lines, since the Lorentz force has no parallel component (see chapter 1.2). This force ensures that the transport perpendicular to the field is reduced greatly, since a single particle will gyrate around the field line and not make larger excursions than the Larmor radius in perpendicular direction. Several processes modify this simple picture in a tokamak.

The classical transport arises from collisions of particles gyrating around neighbouring field lines. It is described by a simple collisional model using the random walk Ansatz.

Simplifying this model to one dimension with a fixed step width of  $\Delta x$  in every time interval  $\Delta t$  and a probability of  $1/2$  to go in each direction the following results are obtained: The mean of the particle movement is zero, so it does not have a directed motion. However, its standard deviation is increasing with the number of steps:  $\sigma = 1/2\sqrt{N}$ . After a time  $\tau = N \cdot \Delta t$  the average distance of the particle from the starting point is  $\delta \propto \sqrt{N} \cdot \Delta x$ . The diffusion coefficient  $D$  is independent of the number of steps  $N$ :

$$D = \frac{\delta^2}{\tau} \propto \frac{N\Delta x^2}{N\Delta t} = \frac{\Delta x^2}{\Delta t} = \text{const.} \quad (2.2)$$

Introducing a density gradient the total flux is the difference between the flux to the right and to the left:  $\vec{\Gamma} = \vec{\Gamma}_{12} - \vec{\Gamma}_{21} = \frac{(n_1 - n_2)\delta}{\tau} = D \cdot \frac{(n_1 - n_2)}{\delta}$ . In the limit of  $\delta \rightarrow 0$  the flux is given by  $\vec{\Gamma} = -D\nabla n$ . Knowing the typical collision frequency  $\nu = \frac{1}{\delta\tau}$  and the displacement length  $\Delta x$  generated by collisions, the flux can be estimated.

The classical heat transport is dominated by ion-ion collisions due to a larger ion Larmor radius. The classical ion heat diffusivity  $\chi_i = r_{L,i}^2 \nu_{ii}$  has values in the range of  $10^{-5}$ - $10^{-4}$  m<sup>2</sup>/s for typical ion temperatures and magnetic fields are ASDEX Upgrade. For a targeted energy confinement time of  $\tau_E = 5$  s for a future fusion reactor this would lead to a minor radius  $a$  of only 7 mm using  $\tau_E = \frac{a^2}{\chi}$ . This finding stands in extreme contrast to experimental observations which predict a minor radius of around 2 m. Hence other mechanisms have to play the dominant role in the radial heat transport in fusion devices.

## 2.2 Neoclassical transport

In the tokamak concept the plasma tube is bent into a ring to reduce the losses at the open ends of a linear plasma device. All magnetic field lines are closed in themselves and no parallel losses can occur. However, the resulting toroidal topology of the field, especially the decaying magnetic field with  $1/R$  leads to several additional transport phenomena due to collisions, the so called neoclassical transport [6].

In general the drift directions of electrons and ions depend on the polarity of plasma current and toroidal magnetic field. In the following the typical orientations at ASDEX Upgrade are assumed: counterclockwise for plasma current and clockwise for toroidal magnetic field. As explained in chapter 1.2 the magnetic field lines have a helical structure due to the induced plasma current in the torus. Particles travelling along field line also fulfil a poloidal motion and experience a higher magnetic field towards the inside of the plasma column. Hereby particles with low parallel velocity are reflected and travel back

if they fulfil the mirror condition:

$$\frac{v_{\parallel}^2(R_0 + r)}{v_{\perp}^2(R_0 - r)} < \frac{B_{max}}{B_{min}} - 1 \quad (2.3)$$

Due to the gradient of the magnetic field the particles experience a  $\nabla B$  drift, which is directed vertically upwards for ions and downwards for electrons for the typical magnetic configuration at ASDEX Upgrade and is described by:

$$\vec{v}_{\nabla B} = -\frac{m \cdot v_{\perp}^2}{2 \cdot q \cdot B^3} \nabla B \times \vec{B} \quad (2.4)$$

The drift can be understood figurative by imagining a smaller Larmor radius at high magnetic field and a larger radius at lower magnetic field. Together, this leads to a particle drift perpendicular to the magnetic field and its gradient which is always directed opposite for electrons and ions.

Additionally the field is bent into a torus, so the particles feel a centrifugal force, which points towards  $\nabla B$ . The resulting curvature drift is pointing in the same direction as the  $\nabla B$  drift. In the low  $\beta$  limit the simplified expression reads as:

$$\vec{v}_{D,curv} = -\frac{m \cdot v_{\parallel}^2}{q \cdot B^3} \nabla B \times \vec{B} \quad (2.5)$$

They can be combined to the drift velocity  $\vec{v}_D$ , which is roughly proportional to the energy of the particles and is directed vertically upwards for ions and downwards for electrons:

$$\vec{v}_D = -\frac{m}{q \cdot B^3} \left( v_{\parallel}^2 + \frac{1}{2} v_{\perp}^2 \right) \nabla B \times \vec{B} \quad (2.6)$$

The orbit of a trapped particle in a circular poloidal cross section is shown in figure 2.1 (a). The particular shape of the particle orbits in the form of a banana gives them their name "banana orbits". A trapped ion starting at the bottom at point (A) drifts inwards on its poloidal path to point (B) due to upwards drift. On its way to the upper turn back point (C) it will drift back to its original flux surface. After the reflection it is travelling back down to its original position (A) and will first drift outwards (point (D)) and then back inwards to complete the banana orbit. In 3D the trapped particles describe a path as shown in figure 2.1 (b) due to the finite poloidal magnetic field. The maximum radial excursion is given by particles of which the turn back points (A) and (C) lie in the middle plain on the high field side. With  $\varepsilon$  being the inverse aspect ratio  $a/R_0$  the resulting banana width  $w_B$  is given by

$$w_B = r_L \frac{q}{\sqrt{\varepsilon}} \quad (2.7)$$

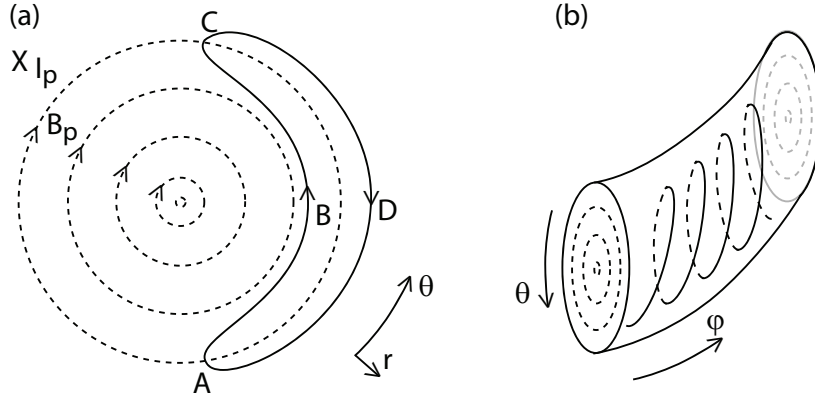


**Figure 2.1:** Plot (a): Schematic of the poloidal projection of the banana orbits in a circular cross section. Plot (b): 3D representation of the course of a trapped particle.

For the neoclassical transport the banana width replaces the Larmor radius as the displacement radius of the collisions in the concept of the collisional model described in the last chapter. The resulting neoclassical diffusivity is roughly 2 orders of magnitude larger compared to the classical one and can be estimated to:

$$D_{neo} = w_B \cdot v_{eff} \frac{n_t}{n} \approx \frac{q^2}{\epsilon^{3/2}} D_{class} \quad (2.8)$$

$v_{eff} = \frac{v_{ei}}{2\epsilon}$  stands for the effective collisionality,  $v_{ei}$  for the electron ion collision frequency and  $\frac{n_t}{n}$  for the trapped particle fraction. However, this increased value cannot explain the experimentally observed transport either. The real particle transport is one order of magnitude and the electron heat transport is two orders of magnitude larger. The experimental ion heat transport is still a factor 3 to 5 larger. These data indicate that neoclassical effects can play a certain role for particle and ion heat transport under special discharge conditions such as transport barriers but again are normally not sufficient enough to explain the experimental observations.

Some additional consequences besides the increased particle and heat transport develop with the transition from a linear to a toroidal geometry.

As soon as a density gradient exists in the region of trapped particles, the plasma itself produces an additional toroidal current, the neoclassical bootstrap current [31]. In the poloidal plane in average more ions move downwards on a flux surface (coming from the banana path further inward) than move upwards (from the banana further outwards) due to this density gradient when the standard orientations of plasma current and magnetic field at ASDEX Upgrade are applied. This produces a small current along the field lines which is proportional to the pressure gradient since the banana orbits are mainly oriented along the field lines:  $j_{BS} \propto -\frac{(\nabla p)}{B_{pol}}$ . Additionally the velocities of passing electrons and ions are adjusted by collisions with the trapped particles, which leads to an enhancement of the current. The bootstrap current consists of both these parts, where the contribution



of the free particles is by far the greater one. The bootstrap current normally flows in the direction of the main plasma current. Nowadays the bootstrap current mainly plays a role in the high gradient zone of the H-mode barrier at the edge. There it provides roughly  $2/3$  of the current density [32]. The contribution to the total current is typically only in the range of 5 to 10 % for the analysed discharges. However, with specific scenarios steady state discharges have been already realised with 100 % of Bootstrap current, e.g. at the tokamak TCV [33]. In future fusion devices the bootstrap current will have considerable values in the main plasma also for standard scenarios due to higher gradients of kinetic profiles. A contribution of more than 20 % to the total plasma current is expected for ITER. For scenarios with reversed shear and a build-up of an internal transport barrier bootstrap current fraction of up to 50 % are envisaged [29].

Another neoclassical effect concerns the collision frequency. Due to the trapping of particles in toroidal geometry a new collision frequency is introduced for tokamaks. The collisionality is defined as the frequency of electron ion collisions  $\nu_{ei}$  divided by the banana bounce frequency  $\omega_{DE}$ :

$$\nu^* = \frac{\nu_{ei}}{\varepsilon \cdot \omega_{DE}} = \frac{\nu_{ei} \cdot q \cdot R}{\varepsilon^{3/2} \cdot \nu_{th,e}}; \quad \nu_{ei} = \frac{5 \cdot 10^{-11} \cdot n_e \cdot Z_i}{T_e [\text{eV}]^{3/2}} \left( \frac{\ln \Lambda}{17} \right) \text{s}^{-1} \quad (2.9)$$

For  $\nu^* < 1$  the diffusivity is in the banana regime and the definition of the neoclassical diffusivity from above is valid.

Using this formula and the expected plasma parameters of ITER for the different scenarios from reference [34] we obtain the following collisionalities at mid radius:

Reference scenario:	$\nu^* = 0.01$
Reversed shear scenario:	$\nu^* = 0.005$
Hybrid scenario:	$\nu^* = 0.008$

## 2.3 Turbulent transport

As seen in the last two chapters, the classical transport alone is far too small to substantiate the experimentally observed behaviour of the particle and heat transport. Also the neoclassical transport is not sufficient to explain the experimental observations. Accordingly other transport mechanisms play the most significant role for these quantities, which were long summarised under the term anomalous transport. Today we know that they are caused by microturbulences.

The most important candidates are ion temperature gradient mode (ITG [35, 36]), trapped electron mode (TEM [37, 38]) and the electron temperature gradient mode (ETG [39]). They are temperature and density gradient driven microturbulences and arise from the stochastic fluctuations of the plasma. The ITG and TEM have radial scales of the ion

Larmor radius, the ETG of the electron Larmor radius. In the following a pictorial view of these instabilities is given. A detailed description can be found in reference [40].

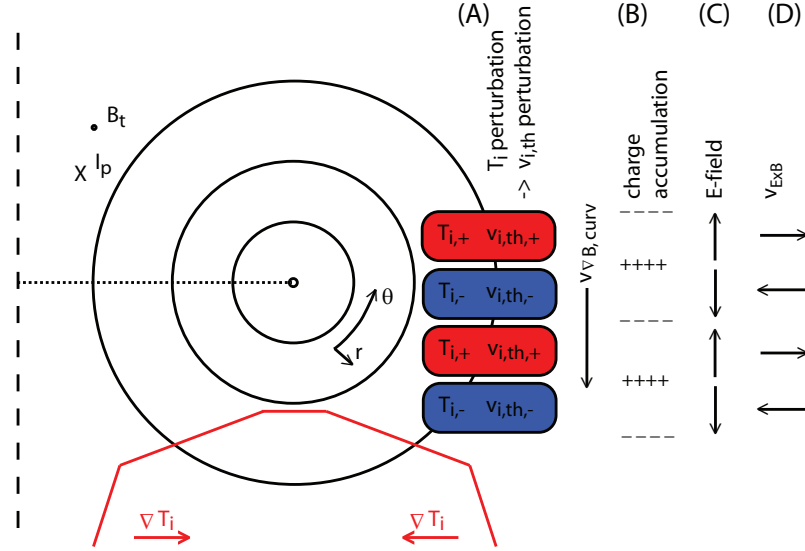


**Figure 2.2:** Schematic view of the mechanism of the ITG drive.

The ITG is mainly driven by the ion temperature gradient, as the name already suggests. A schematic representation of the underlying mechanism is depicted in figure 2.2. We assume an initial vertical periodic temperature modulation on the low field side of the plasma (A). Higher ion temperatures ( $T_{i,+}$ ) lead to higher thermal velocities ( $v_{i,th,+}$ ). Since the vertical downward drift of the ions due to  $\nabla B$  and field line curvature drift is dependent on the particle energy, the ions drift faster in the hotter than in the cooler zones. This leads to an accumulation of positive ions at the bottom of the hotter zone (B). The passing electrons compensate this charge accumulation due to need for quasi neutrality. However, due to their much higher thermal velocity they try to balance the density modulation along the field lines and accumulate at the top of the hotter zones. This charge separation creates a vertical electric field in the hotter zones, which is directed upwards (C). Hotter plasma from further inside is pulled outwards due to charge independent  $E \times B$  drift and enhances the primary perturbation (D). In the cooler regions the electric field is directed downwards, which pulls in cooler plasma from further outside. Both effects enhance the primary perturbation on the low field side which leads to a growth of the instability and radial heat transport in the ion channel.

On the high field side the resulting electric fields point in the same directions as on the low field side but the gradients of the temperatures point in the opposite direction. As a consequence cold plasma is pulled into hotter regions and at the same time hot plasma in cooler regions. Accordingly the initial perturbation is damped and the ITG cannot grow on the high field side. Instead the ITG stays only unstable on the low field side. The ITG has a radial extent of a few ion Larmor radii. Besides the drive of the instability by the ion temperature gradient, it is destabilised by an increase of  $T_e/T_i$  [41] and stabilised by an increase of the inverse gradient length of the electron temperature  $RL_{T_e} = R \cdot \frac{dT_e}{dr} \frac{1}{T_e}$ , the electron density  $RL_{n_e} = R \cdot \frac{dn_e}{dr} \frac{1}{n_e}$  [42] and the magnetic shear [41].

The electron temperature gradient mode (ETG) is similar to the ITG on much shorter scales and higher frequencies, only that in this case the electrons take the role of the ions as disturbed species. Their initial modulation leads to an accumulation at the top of the hotter region due to their opposite  $\nabla B$  and curvature drift direction. The ions build a positive background distribution. Their larger mass leads to a larger inertia, so that they cannot follow the fast modulation of the electrons. The resulting  $E$  field is pointing in the same direction as for the ITG mode. This drags hot plasma in the hotter regions and cold plasma in the cooler regions on the low field side. Through this mechanism, the primary perturbation is enhanced. On the high field side the same effect as for the ITG occurs, namely that the fluctuations are not enhanced but stabilised. The ETG has a radial extent of a few electron Larmor radii. The ETG is stabilised by an increase of  $RL_{n_e}$  [42],  $T_e/T_i$  and the magnetic shear [41].

A third microinstability possibly responsible for heat transport in tokamaks is the trapped electron mode (TEM). As the name suggests, they occur in the presence of trapped electrons. A similar mechanism as for the ITGs applies with the difference, that the slower parallel motion is generated by the slow precession in toroidal direction of the banana orbits of trapped electrons and not by the ion inertia. Besides an electron temperature gradient, also a density gradient can act as a drive for this mode: The electron motion on banana orbits interacts with a positive density perturbation which is always elongated along the field lines due to higher parallel mobility of electrons and ions in that direction. This leads to a charge separation similar to the previously described situation for ITGs and ETGs. Positive charges accumulate at the bottom of the density blob and negative charges at the top. The resulting electric field drags plasma from further inside into the density blob and enhances the primary perturbation. The TEM is destabilised by an increase of  $T_e/T_i$  [42] and stabilised by an increase of  $RL_{T_i} = R \cdot \frac{dT_i}{dr} \frac{1}{T_i}$  and the magnetic shear [41].

## 2.4 ASTRA

Besides the direct interpretation of the experimental data of the performed experiments some extended analyses were performed. For this purpose the transport code ASTRA (Automated System of TRansport Analysis) was used [43]. This code was developed to provide a framework for the computation and analysis of transport equations in nowadays tokamak fusion experiments. It is designed in a modular way that allows the use of numerous existing routines for analyses and computations of transport properties or plasma quantities. Additionally the implementation of user defined routines is elementary and straightforward. It allows a fast design of the code to suit the needs of a special analysis and the development of complex models step by step. A graphical user interface provides a practical way to evaluate the computations and offers the possibility to vary the parameters of the calculations during runtime. All these attributes qualify ASTRA as a suitable tool for the analysis of the transport phenomena observed in this work.

ASTRA is designed in a flexible and universal way in order to apply it to different experiments by only changing a few relevant geometric parameters characteristic for each experiment such as major and minor radii, elongation and triangularity. The radial transport is treated as flux surface averaged quantities and ASTRA solves the 1D local transport of particles, heat and momentum. The poloidal magnetic equilibrium can be prescribed in a realistic 2D way. The newest version of ASTRA (ASTRA 7) is coupled with the equilibrium code Spider [44], which can solve the plasma equilibrium for a realistically prescribed numerical boundary with X-point geometry. Since the use of ASTRA in this work concentrates on heat transport the most important transport equations are presented in the following. A deeper introduction to the programme package can be found in reference [43].

The transport equations for particles and heat are already included in ASTRA and are calculated automatically. This fundamental set of equations includes the electron and ion temperatures  $T_e$  and  $T_i$ , the electron density  $n_e$  and the poloidal flux  $\Psi$ . The fluxes of these quantities (electron and ion particle flux  $\Gamma_e$  and  $\Gamma_i$ , electron and ion heat flux  $q_e$  and  $q_i$ ) are expressed by a set of coupled differential equations in the following form:

$$\begin{aligned}
\frac{1}{V'} \left( \frac{\partial}{\partial t} - \frac{\dot{B}_0}{2B_0} \frac{\partial}{\partial \rho} \rho \right) (V' n_e) + \frac{1}{V'} \frac{\partial}{\partial \rho} \Gamma_e &= S_e \\
\frac{3}{2} (V')^{-\frac{5}{3}} \left( \frac{\partial}{\partial t} - \frac{\dot{B}_0}{2B_0} \frac{\partial}{\partial \rho} \rho \right) [(V')^{\frac{5}{3}} n_e T_e] + \frac{1}{V'} \frac{\partial}{\partial \rho} \left( q_e + \frac{5}{2} T_e \Gamma_e \right) &= P_e \\
\frac{3}{2} (V')^{-\frac{5}{3}} \left( \frac{\partial}{\partial t} - \frac{\dot{B}_0}{2B_0} \frac{\partial}{\partial \rho} \rho \right) [(V')^{\frac{5}{3}} n_i T_i] + \frac{1}{V'} \frac{\partial}{\partial \rho} \left( q_i + \frac{5}{2} T_i \Gamma_i \right) &= P_i \\
\sigma_{\parallel} \left( \frac{\partial \Psi}{\partial t} - \frac{\rho \dot{B}_0}{2B_0} \frac{\partial \Psi}{\partial \rho} \right) &= \frac{J^2 R_0}{\mu_0 \rho} \frac{\partial}{\partial \rho} \left( \frac{G_2}{J} \frac{\partial \Psi}{\partial \rho} \right) - \frac{V'}{2\pi \rho} (j_{BS} + j_{CD})
\end{aligned} \tag{2.10}$$

$S_e$  stands for the source of the electrons,  $\sigma_{\parallel}$  stands for the parallel conductivity and  $\rho$  stands for the effective minor radius. Following definitions are used:  $V' = \partial V / \partial \rho$ ,  $G_1 = \langle (\nabla \rho)^2 \rangle$ ,  $G_2 = V' / 4\pi^2 \langle (\nabla \rho / r)^2 \rangle$ ,  $J = I / (R_0 \cdot B_0)$ . One important coupling mechanism of electron an ion channel is the heat exchange term from electrons to ions due to Coulomb collisions:

$$P_{e \rightarrow i} = 3 \cdot \frac{m_e}{m_i} v_{ei} \cdot n_e \cdot (T_e - T_i) \tag{2.11}$$

The difference between electron an ion temperature reaches considerable values in the experiments conducted during this thesis. Accordingly this term has to be taken into account when calculating the sources of electron and ion heat  $P_e$  and  $P_i$ , which consists of the heating contributions of Ohmic, NBI, ICRH and ECRH and the radiated power as loss term:

$$\begin{aligned}
P_e &= P_{OH} + P_{NBI,e} + P_{ICRH,e} + P_{ECRH} - P_{rad} - P_{e \rightarrow i} \\
P_i &= P_{NBI,i} + P_{ICRH,i} + P_{e \rightarrow i}
\end{aligned} \tag{2.12}$$

In ASTRA the transport matrix of the convective terms for the computation of kinetic quantities and fluxes reads as follows:

$$\begin{pmatrix} \frac{\Gamma_e}{n_e} \\ \frac{q_e}{n_e \cdot T_e} \\ \frac{q_i}{n_i \cdot T_i} \end{pmatrix} = -V' \cdot G_1 \begin{pmatrix} D_n & D_e & D_i \\ \chi_n^e & \chi_e & \chi_i^e \\ \chi_n^i & \chi_e^i & \chi_i \end{pmatrix} \cdot \begin{pmatrix} \frac{1}{n_e} \frac{\partial n_e}{\partial \rho} \\ \frac{1}{T_e} \frac{\partial T_e}{\partial \rho} \\ \frac{1}{T_i} \frac{\partial T_i}{\partial \rho} \end{pmatrix} \quad (2.13)$$

For most applications and for the calculations in this thesis as well, the non diagonal terms of the transport coefficient matrix are set to zero. The then effective particle and heat diffusivities  $D_n$ ,  $\chi_e$  and  $\chi_i$  depend on the quantity itself.

One part of the investigation was the analysis of the experimental data with a power balance analysis. In this standard technique in fusion research, the heating and loss powers of electrons and ions are integrated over the volume inside a flux surfaces. This provides the profiles of heat fluxes of each species if the power transferred from electrons to ions due to Coulomb collisions is taken into account. From the heat fluxes the effective experimental heat diffusivities of the electron and ion channel can be inferred [45]:

$$\chi_e^{PB} = -\frac{q_e}{V' \cdot G_1 \cdot n_e \cdot \partial_\rho T_e} \quad (2.14)$$

For the power balance analysis ASTRA is provided with the following quantities as input parameters:

- Shape of the separatrix from 2D magnetic equilibrium calculations, providing the shape and the volume of the plasma. The flux surface structure is calculated internally by the equilibrium solver SPIDER.
- Geometric quantities of vessel and plasma
- Time traces of plasma current  $I_p$ , magnetic field  $B_t$  and loop voltage  $u_{loop}$
- Profiles of the ECRH power deposited to the electrons  $P_{ECRH}$
- Profiles of the NBI power deposited to the electrons and ions  $P_{NBI,e}$  and  $P_{NBI,i}$
- Profiles of the ICRH power deposited to the electrons and ions  $P_{ICRH,e}$  and  $P_{ICRH,i}$
- Profiles of the driven currents by ECRH, NBI and ICRH  $j_{ECRH}$ ,  $j_{NBI}$  and  $j_{ICRH}$
- Profile of the plasma radiation  $P_{rad}$
- Kinetic profiles of electron density  $n_e$ , electron and ion temperatures  $T_e$  and  $T_i$  and toroidal plasma rotation  $v_{tor}$
- Profiles of the effective charge  $Z_{eff}$

The magnetic equilibrium originates from Clite calculations which determine the flux surface structure from external measurements of the magnetic field [46, 47]. Geometric quantities of the vessel are taken from the ASDEX Upgrade database. Geometric quantities of the plasma like minor and major radius, elongation, triangularity and the time traces of plasma current  $I_p$ , magnetic field  $B_t$  and loop voltage  $u_{loop}$  are read from the ASDEX Upgrade shotfile system, which allows the access to the majority of experimental measurements.

The radial profiles of the ECRH power deposited to electrons ( $P_{ECRH}$ ) and the driven current ( $j_{ECRH}$ ) are calculated by the beam tracing code Torbeam (see chapter 3.3) [48]. The profiles of the electron and ion heating by NBI are calculated by NUBEAM (see chapter 3.1) [49].

The radial distribution of the plasma radiation is deduced from a deconvolution of the foil bolometers as described in chapter 4.6. The 2D radiation distribution is flux surface averaged to obtain a radial profile. The kinetic profiles of electron density  $n_e$ , electron and ion temperatures  $T_e$  and  $T_i$  and toroidal plasma rotation  $v_{tor}$  are read from shotfile, fitted with a spline function and used as time dependent input data. The input profiles to the various codes were checked against the output profiles to ensure a correct mapping to the same radial grid, namely the normalised toroidal flux coordinate  $\rho_{tor}$ .

Additionally to the interpretative operation, the ASTRA code package provides the framework for the trapped gyro-Landau fluid transport model TGLF (see next chapter 2.5). In the course of this modelling the necessity to use a correct description of the experimentally observed sawtooth crashes came to light to reproduce the kinetic profiles accurately.

The sawtooth instability is an internal kink mode with the mode numbers  $m = 1$  and  $n = 1$  as shortly presented in chapter 1.3. It occurs when the central q-value falls below unity. An island develops at the location of the  $q = 1$  surface, grows and displaces the original central region of the plasma. The plasma current is redistributed, the former core region disappears by reconnection and the central q-value stays above unity. Peaked temperature and density profiles are flattened in this process due to redistribution of the plasma. The central q-value slowly decreases due to current diffusion into the core of the plasma until the next crash occurs. The density is not affected greatly, since its profiles are typically flat in the centre.

The code package to model the sawtooth crashes used in ASTRA (ASTSAW) applies the Kadomtsev-Porcelli model. It simulates a complete reconnection of the inner part of the plasma inside the  $q=1$  surface [6, 50]. It assumes the toroidal flux  $\Phi$  to be invariant, and applies relaxation of the helical flux

$$\Psi_* = \Phi - \Psi = \int (1 - q) d\Psi \quad (2.15)$$

and energy and particle conservation.  $\Phi$  stands for the poloidal flux. With this formalism the magnetic axis reconnects with the mixing radius to the mixing radius itself. The

inversion radius reconnects itself to the magnetic axis. During this process the dense and hot plasma of the core inside the inversion radius is redistributed further outside between the inversion and mixing radii. Additionally the model ensures a smooth transition of the equilibrium structure and the kinetic profiles between the reconnected area and the outer, unperturbed part. The reconnection is implemented as an instantaneous process, justified by typical experimental reconnection times of  $100 \mu\text{s}$ , which are much faster than any transport processes.

## 2.5 TGLF

Additionally to the direct interpretation of the experimental data and the power balance analysis with ASTRA the profiles of electron and ion temperature and electron density and their change with modified heating mix were modelled in a predictive way. For this purpose the trapped gyro-Landau fluid transport model TGLF was utilised [51, 52]. It is applied in a version that uses ASTRA as framework for an iterative approach leading to a self consistent solution of temperatures, densities, particle and heat fluxes and the corresponding diffusivities. TGLF builds up on the Gyro-Landau fluid equations (GLF), which are velocity moment equations of the gyro-averaged kinetic equations. The code solves the linear eigenmodes of trapped ion and electron modes, ion and electron temperature gradient modes and electromagnetic kinetic ballooning modes. Details about kinetic ballooning modes, which are high- $n$  magnetic turbulence can be found in [53]. Since they are not observed in the experiments presented in this work they are not considered further. TGLF is capable to compute the quasi linear fluxes of particles, heat, and toroidal and parallel viscous stresses. Additionally these equations are closed so that kinetic effects such as Landau damping are kept. Details can be found in references [54–61].

Additionally TGLF considers both trapped and passing particles in the same set of equations to the effect that computing power demands are not increased excessively while the representation of the physical relations is improved significantly. For that reason lowest frequency trapped ion modes can be handled in the same way as highest frequency electron temperature gradient modes. Electron collisions, which are not considered in the typically used closures of the equation systems are also included and improved [62]. This inclusion allows a better reproduction of diffusion coefficients depending on the collisionality, which is one of the key parameters in this thesis, which was varied. Free parameters of the model for the saturated mode amplitude and the electron-ion collision model have been fitted to an extensive database of gyrokinetic simulations performed with GYRO [63], a nonlinear tokamak micro turbulence package developed at General Atomics.

The non diagonal terms in the transport matrix 2.13 are kept at zero in the ASTRA notation. Their impact on the particle and heat fluxes is treated internally in TGLF and added to  $D_n$ ,  $\chi_e$  and  $\chi_i$ . TGLF describes the central part of the plasma from first principles, but cannot describe the reduced transport inside the H-mode steep gradient zone. For that rea-



son the experimental values of the electron density and the electron and ion temperatures at  $\rho_{tor} = 0.85$  are applied as boundary condition for the modelling.

## 2.6 GS2

During the process of this work some calculations were executed with the gyrokinetic code GS2 [64, 65]. The gyrokinetic approach averages over the gyro motion of electrons and ions reducing the dimensions from 6D to 5D. GS2 solves the gyrokinetic Vlasov-Maxwell equations system of a perturbed distribution function ( $\delta f$  code). It uses the  $\rho^* \rightarrow 0$  limit local flux-tube in toroidal geometry, and includes general axis symmetric magnetic equilibria, multiple species, trapped and passing kinetic electrons, electromagnetic fluctuations, collision operators and equilibrium scale  $E \times B$  shear flow [66]. GS2 is a nonlinear code but has been applied linearly in this work due to the huge computational saving by this approach.

The performed linear runs provide the possibility of calculating the dominant microinstabilities which are responsible for the radial heat transport. Additionally their growth rates, frequencies and the resulting heat fluxes can be determined, latter arising from the quasi linear cross phase between pressure and potential fluctuations. GS2 provides a robust scheme to run linear gyrokinetic calculations due to its implicit scheme to solve the gyrokinetic equations of the distribution functions in time and poloidal angle.



CHAPTER 2. HEAT TRANSPORT THEORY AND DESCRIPTION OF COMPUTER CODES

---

# Chapter 3

## Heating systems at ASDEX Upgrade

The operation of a tokamak and the generation of the helical magnetic field structure requires a strong externally applied toroidal magnetic field and a large toroidal plasma current in the range of about one mega ampere in ASDEX Upgrade. A plasma with a temperature of a few keV has a small, but non-zero resistance of around 0.4 Ohm for one toroidal turn. The plasma current of 1 MA leads to a heating power by Ohmic losses of typically  $P_{Ohm} = RI^2 \sim 0.4$  MW for the plasmas analysed in this work. Since the electrical conductivity increases with temperature according to  $\sigma_e \propto T^{3/2}$ , the Ohmic heating loses efficiency when increasing the temperature. Therefore with Ohmic heating only typically maximum temperatures of 0.5 to 1 keV can be reached. Consequently additional heating systems are required to increase the temperatures towards fusion relevant values.

At ASDEX Upgrade three different auxiliary heating systems are installed:

1. Neutral beam injection (NBI) [67], which heats both electrons and ions depending on the beam energy and the electron temperature
2. Ion cyclotron resonance frequency heating (ICRH) [68], which also heats both species with a similar power distribution between electrons and ions as the NBI, depending on the energy of the resonantly accelerated ions
3. Electron cyclotron resonance heating (ECRH) [69], which heats only the electrons locally

The existing variety of heating systems provides a great flexibility to explore the influence of their specific heating characteristics on the plasma performance in an experiment like ASDEX Upgrade. Depending on the used system the heated species, the amount and radial distribution of heating power, torque input and current drive can be varied. This

chapter presents the basic functionality of the different heating systems and describes the characteristics and differences between them which are relevant for this work.

The toroidal and poloidal location of the used heating systems are illustrated in figure 3.1 and figure 3.2. In addition also the diagnostics are shown which are presented in chapter 4.

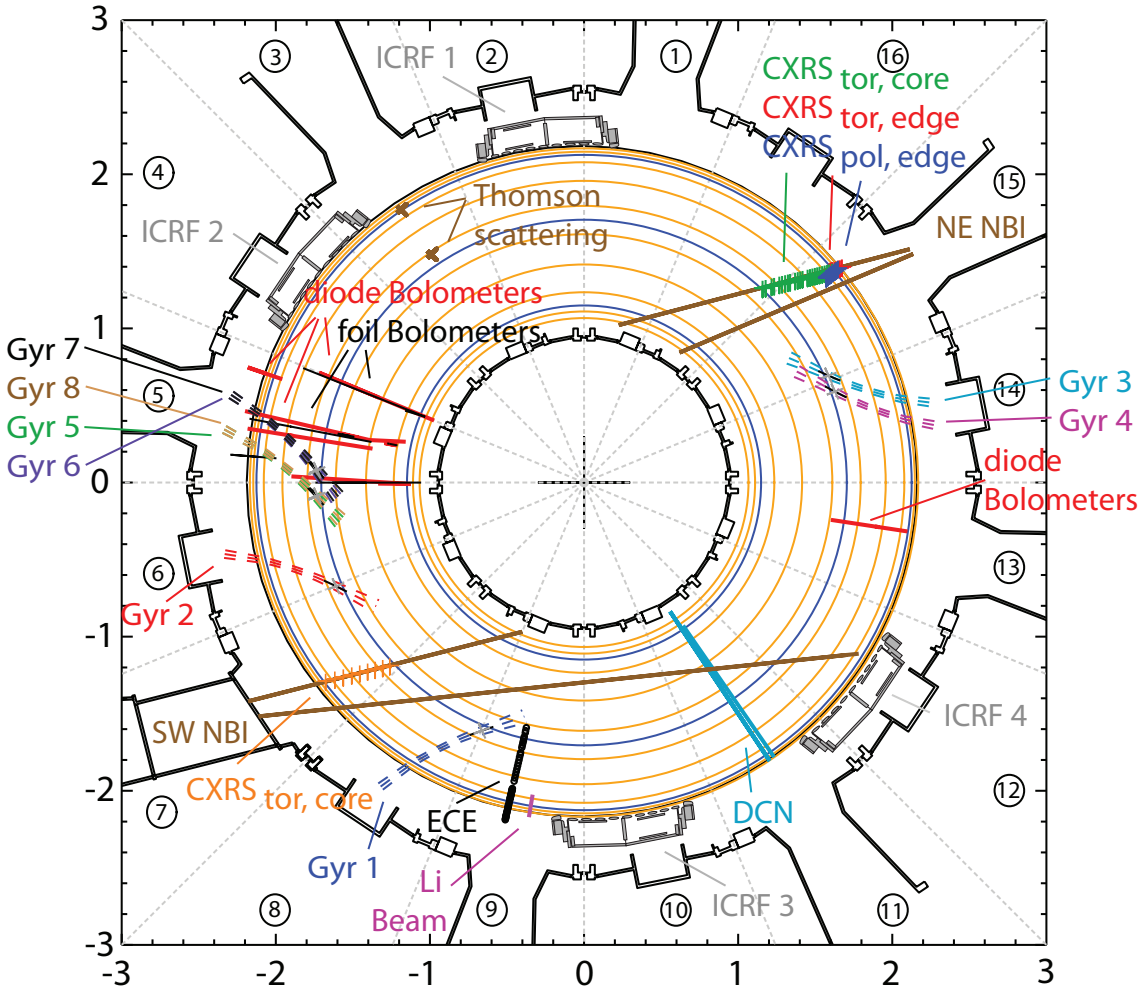
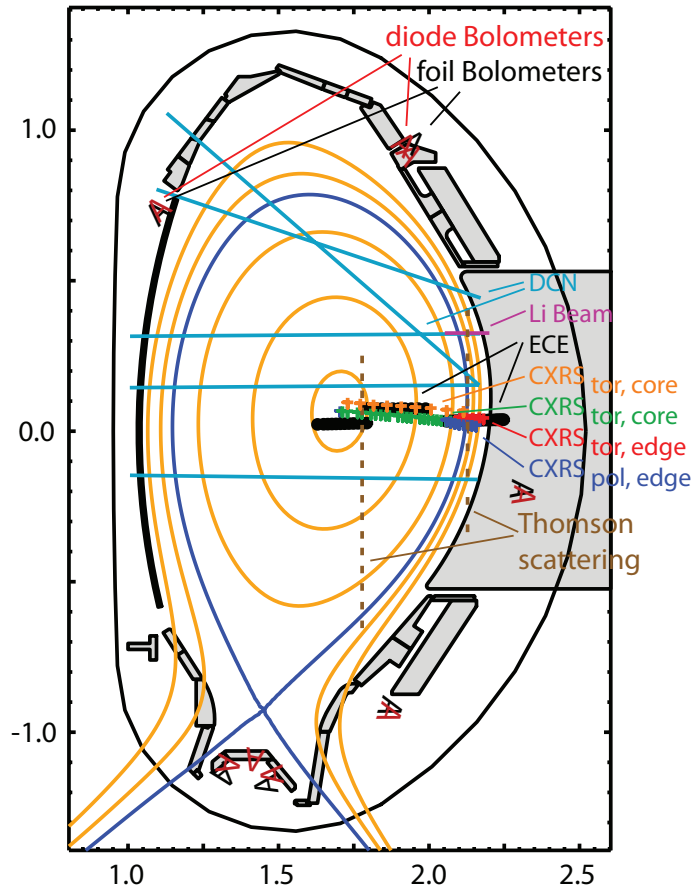


Figure 3.1: Toroidal scheme of the used heating and diagnostic systems.

### 3.1 Neutral beam injection

The most widely used heating system in fusion research is the neutral beam injection (NBI) [67]. It is the work horse also at ASDEX Upgrade and consists of two systems, called injector boxes. Each one is equipped with 4 beams at 2.5 MW heating power adding up to a maximum power of 20 MW delivered to the plasma. The fundamental



**Figure 3.2:** Poloidal scheme of the used heating and diagnostic systems.

principle of the two systems is the same, but the technical implementation differs slightly. The primary plasma for ion production in the southeast neutral beam injector (SE NBI, beam 1 to 4) is created by an arc source which needs regular replacement and extensive cooling. The northwest neutral beam injector (NW NBI, beam 5 to 8) however uses a radio frequency driven source, which has a cheaper and significantly simpler design. The ions are extracted from the primary plasma and accelerated in an electric field to energies of 60 keV for the SE NBI and 93 keV for the NW NBI. A decrease of the acceleration voltage is possible to reduce the power per beam and to be able to vary the total NBI heating power in smaller steps. The beams are directed towards the plasma after neutralisation of the fast ions by collisions with neutral hydrogen gas in the source. The neutralisation step is extremely important since otherwise the beam would be deflected by the strong toroidal magnetic field and would not enter the plasma but intersect with the vessel structures damaging them. The beam paths are shown in figure 3.1 as brown solid lines. In the toroidal projection two beams lie always on top of each other, having slightly different poloidal angles.

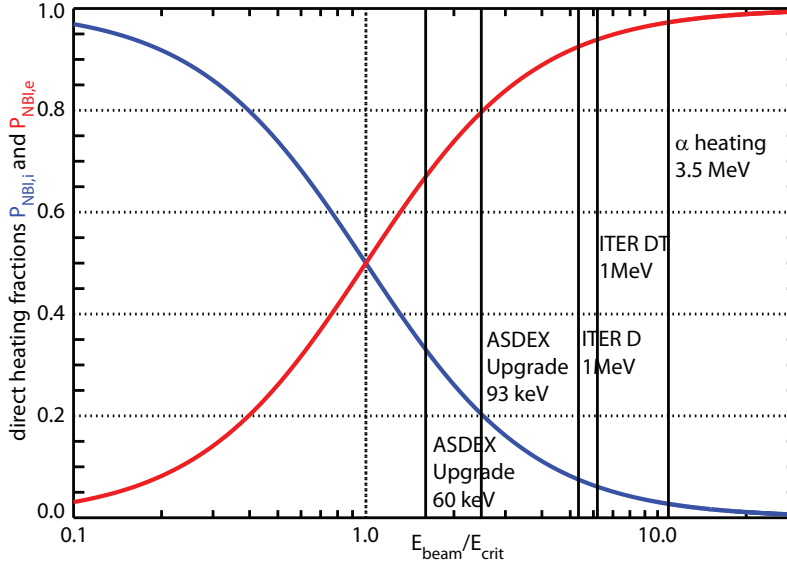


**Figure 3.3:** Fraction of direct NBI power going to ions (red) and electrons (blue) depending on the fraction of  $E_{beam}$  and  $E_{crit}$ . The typical conditions at ASDEX Upgrade and the expected values for ITER and DEMO are indicated.

The neutral atoms are ionised in the plasma by three collisional processes:

- Charge exchange with hydrogen
- Ionisation by ions
- Ionisation by electrons

The combined cross sections of these three processes lead to the attenuation of the fast particle beam. The decay length depends on the line integrated density  $\int n dl$  and beam energy  $E_{Beam}$  and has a value in the range of 25 cm for typical plasma parameters. This is roughly half the minor radius of ASDEX Upgrade and allows central heating and slightly off axis current drive. The ionised hydrogen atoms are trapped in the magnetic field structure by gyration around field lines. They transfer their energy to the plasma by Coulomb collisions with electrons and ions and thermalise. The fraction of power deposited in each species is dependent on the beam energy and the temperature of the plasma. An important value is the critical energy:

$$E_{crit} = 14.8 \frac{A_{beam}}{A_{plasma}^{2/3}} T_e \quad (3.1)$$

It reduces to  $E_{crit} = 18.6 T_e$  for a deuterium beam into deuterium plasma, which is the typical operation mode at ASDEX Upgrade. The direct heating by an ion with critical energy is equal for both species while for lower ion energies mainly the ions and for higher energies mainly the electrons are heated [6]. The fraction of direct heating going to electrons and ions with respect to the fraction of beam energy  $E_{beam}$  to critical energy  $E_{crit}$  can be seen in figure 3.3. Examples of typical cases analysed in this

work and relevant for fusion research are also shown (ASDEX Upgrade: D,  $T_e = 2$  keV,  $E_{beam} = 60/93$  keV, ITER: D, D/T mix,  $T_e = 10$  keV,  $E_{beam} = 1$  MeV,  $\alpha$ -heating: D/T mix,  $T_e = 10$  keV,  $E_\alpha = 3.5$  MeV). The actual power distribution between electrons and ions differs from the fraction presented above since several relevant plasma and beam quantities do not stay constant along the beam path of the NBI. First, the power fraction depends on the particle energy which is a mixture of the three different energy components ( $1 \cdot E_{beam}$ ,  $1/2 \cdot E_{beam}$ ,  $1/3 \cdot E_{beam}$ ) which arise from a coextraction of  $D_2^+$  and  $D_3^+$  besides  $D^+$  from the primary plasma at the same acceleration voltage. Second, the particle energy is reduced along its path through the plasma due to successive slowing down of the ions by collisions. Third, the power fraction depends on the electron temperature profile and the attenuation of the beam along its path, for which also the electron density profile is relevant.

Due to the variety of variables in the calculation, most of them having radially changing values, numerical methods are used to calculate the deposition profiles of the NBI power to electrons and ions. These calculations have to include the exact description of ionisation, charge exchange and slowing down processes which lead to the birth profiles of fast ions from the injected neutrals. For this work they were calculated time dependent for each individual discharge with the Monte Carlo code NUBEAM [49]. It is embedded in the code package TRANSP, which is a "large comprehensive time dependent tokamak transport data analysis code" developed at the Princeton Plasma Physics Laboratory [70–72]. The code is provided with the time dependent plasma equilibrium, kinetic profiles and geometric details of the NBI system and calculates among various other quantities the profiles of the energy deposition to electrons and ions and the profiles of the driven current by the fast particle beam.

The computation shows that the SW NBI (60 keV) delivers roughly 50 % of its energy to electrons and 50 % to ions for a typical discharge with a central electron temperature  $T_e \approx 2$  keV and an electron density  $n_e \approx 9 \cdot 10^{19} \text{m}^{-3}$ . Since the voltage of the NW NBI (93 keV) was reduced for most experiments to vary the heating mix in small steps, the power distribution between electrons and ions was similar. Typically the beam voltage was reduced to values of around 52 keV. By this means one gyrotron could replace one beam source, which delivers only 800 kW to the plasma under these conditions. The voltage of the SW NBI was kept at its maximum value of 60 keV to increase the signal of the charge exchange recombination spectroscopy and to allow measurements up to the core (see chapter 4.3).

The deposition profiles of the NBI power to electrons and ions are broad and span the entire plasma radius since the density profile is rather flat for the entire core of the plasma inside the pedestal of the H-mode. Since the electron heating fraction is larger for high energy ions and low electron temperatures, their heating profiles are typically rather flat inside mid radius. The ions are heated less at the edge, while their power deposition profiles peak centrally, where the fast ions slow down more and more and the electron temperature is higher. A comparison of the power deposition profiles to electrons and ions of the NBI heating with the other heating methods like ICRH and ECRH is made in figure 3.5.

The minor radius of future fusion reactors will be significantly larger (ITER: 2.0 m compared to 0.5 m at ASDEX Upgrade [67]) whereas the electron density is expected to have similar values as today. Therefore the beam energies have to be increased dramatically to enable the necessary amount of heating and current drive in the centre of the plasma. This trend is even more true for future fusion devices like DEMO (minor radius  $a \sim 2.5$  to 3 m). For that reason beam sources are currently under development which are in the range of 1 MeV acceleration voltage. The temperatures in future devices are not foreseen to increase equally which leads to an increased electron heating. Going towards a fusion reactor will also bring an increased contribution of  $\alpha$ -heating with an energy of 3.5 MeV. This will lead to a predominant electron heating of more than 80 %. For that reason the analysis of mostly electron heated plasmas and their theoretical understanding in nowadays experiments is a very important task and the main motivation for this thesis.

## 3.2 Ion cyclotron resonance frequency heating

Additionally to the Ohmic heating and the NBI injection the plasma is also heated by electromagnetic waves in the radio frequency and microwave range.

The ion cyclotron resonance frequency heating (ICRH [68]) couples to the plasma via the cyclotron frequency of the ions  $\omega_{c,ion}$ . To first order it is independent of the velocity of the ions and thus their thermal energy. At ASDEX Upgrade mainly the minority heating scheme at the fundamental harmonic is applied [73]. The heated ion species is hydrogen typically also present in deuterium discharges by a few percent. The resonant frequency for central power deposition to hydrogen is  $f = 36,5$  MHz for a typical 2.5 T discharge.

ASDEX Upgrade is furnished with 4 ICRH systems. In each system the primary wave is produced by a 20 mW oscillator and the power is amplified in 4 stages up to 2 MW and fed into the transmission lines. They are equipped with numerous matching elements, which align the impedance of the generators with the transmission lines. At ASDEX Upgrade 4 antennas are installed, each consisting of two straps of 0.8 m forming a dipole. Their toroidal location is shown in figure 3.1 in grey. Due to imperfect coupling to the plasma some percent of the power are reflected at the antennas back into the transition lines. Two antennas each are connected with directional couplers, which redirect this reflected power to the other antenna. These measures avoid the load of the e.m. generators with power coming from their outlet and circumvent the damage of the system [68]. At each antenna a fast magnetosonic (compressional Alfvén [6]) wave is excited, tunnelling the gap between the antennas and the plasma with densities above the cutoff density as an evanescent wave ( $k_{\parallel} > k_0$  [74]). The cutoff density can be written as [75]

$$n_{e,cutoff} \cong 5.2 \cdot 10^{16} k_{\parallel}^2 \frac{1}{(1+\varepsilon)} \frac{\omega_{c,ion}}{\omega} \left( \frac{1}{(1+\varepsilon)} \frac{\omega_{c,ion}}{\omega} + 1 \right) \frac{A}{Z} \quad (3.2)$$



### 3.2. ION CYCLOTRON RESONANCE FREQUENCY HEATING

---

It occurs typically in the range of  $5 \cdot 10^{18} \text{m}^{-3}$  which implies a few centimetre gap for ASDEX Upgrade. To reduce reflections at the cutoff this gap has to be minimised without exposing the metal limiter structures to unacceptable high heat fluxes. Especially under reactor conditions and in the presence of ELMs this is a difficult undertaking and needs a precise matching of the shape of the antenna and the separatrix. The design and development of suitable antennas is subject to present research [76]. As soon as the electron density is above the cutoff density the wave travels as a magnetosonic wave to the absorption area. The power deposition area is determined in radial direction by the resonance condition widened by Doppler broadening. The absorption width  $\Delta r = k_{\parallel} \cdot \frac{v_{th,i}}{\omega_{c,ion}}$  is typically a few centimetres. In the vertical plane the power deposition area is determined by the orientation of the antennas and their focussing capabilities. The mounting of the antennas around the mid plain leads to an illumination of the resonance layer in the centre of the plasma. Accordingly the power deposition is typically peaked in the centre.

A direct heating of deuterium at the fundamental cyclotron frequency is hampered by a small absorption of the wave due to an opposite rotation of the electric field with respect to the ions [6]. This direct heating contributes typically around 10 % of the power to the total heating. Additionally a few percent of the energy of typically 2 to 5 % is directly absorbed by electrons by Landau damping and transit time magnetic pumping due to parallel electric fields [77]. This is only valid for higher electron temperatures. In addition finite Larmor effects have to be taken into account. Apart from that, the fast wave transfers its energy mainly to the minority species hydrogen by Landau cyclotron damping. Fast ions are produced inside the plasma with a strong tail in the distribution function. These fast ions thermalise similar to the fast ions of the NBI by Coulomb collisions with electrons and ions. They transfer their energy to both species depending on the electron temperature and the energy distribution of the fast hydrogen. For this thesis the deposition profiles to electrons and ions were calculated with the RF wave deposition model TORIC4 inside the TRANSP code package [78]. The distribution is shared roughly half between electrons and ions in the experiments performed during this work. The heating profiles of the ICRH are peaked more in the centre of the plasma compared to the profiles of the NBI and typically heating the innermost 15 cm of the plasma. Due to the large wavelength and the small focussing capabilities of the ICRH antennas, the broadness of the deposition profiles lies between the NBI and ECRH. The comparison of the power deposition profiles with the other heating methods like NBI and ECRH is shown at the end of the next chapter in figure 3.5.

Since the replacement of the plasma facing components at ASDEX Upgrade from carbon to tungsten, the operation of the ICRH led to a strong increase of the W concentration in the plasma [76]. Strong electric fields at the ICRH limiters induced a high sputtering yield and thus a high W influx which made the operation of the ICRH system in H-modes nearly impossible. The replacement of one antenna with broad limiters and narrow straps in 2011 and the coating of the side limiters of other 2 antennas with boron led to a strong reduction of the tungsten influx. These measures enable an operation of the ICRH system with up to 3 MW with only a moderate increase of the tungsten concentration in the plasma.

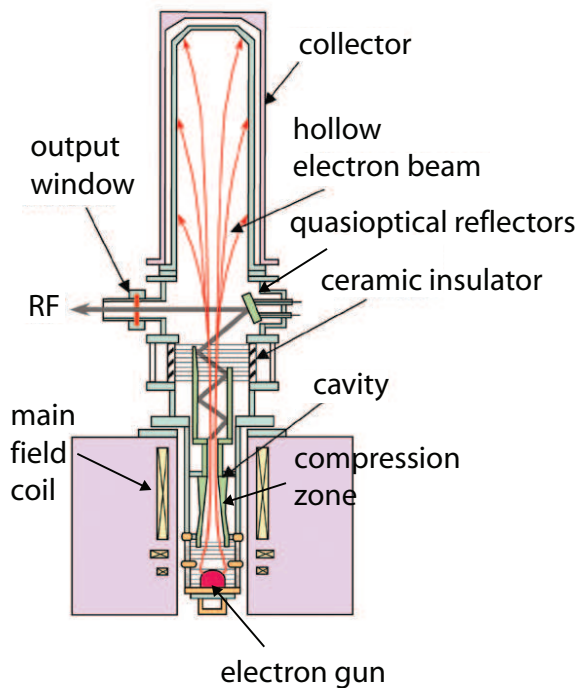


Apart from the differences in the power deposition profiles, the main difference to NBI heating is the absence of any torque input and particle fuelling by the ICRH. Hence the comparison of NBI and ICRH discharges permits the analysis of the influence of rotation on the plasma behaviour and the decoupling of fuelling and particle pinch when replacing NBI/ICRH by ECRH power.

### 3.3 Electron cyclotron resonance heating

The second wave heating system at ASDEX Upgrade is the electron cyclotron resonance heating (ECRH) consisting of microwaves of 140 (or 105) GHz which are generated by gyrotrons [69]. Gyrotrons are maser in which a microwave resonator is excited by electrons gyrating with the microwave frequency in an axial magnetic field [79].

(a) schematic of a gyrotron



(b) # 28117,  $t = 4.30$ , gyrotron 6

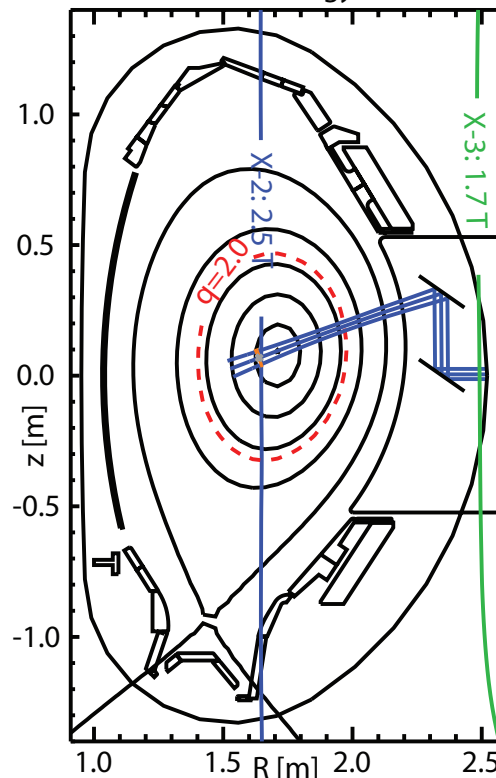


**Figure 3.4:** Plot (a): Schematic representation of a gyrotron [80]. Plot (b): Beam tracing calculation of one gyrotron at ASDEX Upgrade with experimental equilibrium. Shown as grey cross is the point of maximum absorption, as orange band the area of 99.99 % power deposition. Added as sketch is the mirror system which can steer the microwave in poloidal and toroidal direction.

A schematic representation of a gyrotron can be seen in figure 3.4 (a). In an evacuated tube a hollow electron beam is produced by a ring shaped electron gun. The beam is

### 3.3. ELECTRON CYCLOTRON RESONANCE HEATING

---

accelerated to weakly relativistic speeds of 73 keV, focussed and directed into a compression zone. An axial magnetic field of 5.3 T is produced in this zone almost parallel to the electron motion by a superconducting magnet. The parallel motion is transformed into perpendicular gyration around the magnetic field lines due to increasing magnetic field and the invariant of the magnetic moment  $\mu$  (see chapter 1.2). The electrons emit cyclotron radiation and excite a resonant mode inside an oversized resonant cavity. The e.m. wave is reflected at both ends at the cut of the cavity. This occurs since the mode resides near the cutoff due to the large applied magnetic field, which influences the electron motion [81]. Only one particular mode is excited, i.e. the TE<sub>22,8</sub> mode [82] in the case of the gyrotrons at ASDEX Upgrade. The electrons gain a phase focus and slow down due to an energy transfer to the high frequency e.m. field. The electromagnetic wave is then decoupled from the cavity by a special design of the cavity outlet (Vlasov mode converter [83, 84]). Its directional design and metal reflectors inside the gyrotron allow a quasi optical direction of the microwave through a diamond disk window [85] towards the wave guides. The electron beam still carries a substantial fraction of the initial acceleration energy which has to be absorbed by the collector. Using a depressed collector gives the possibility to recover some of that lost energy to an overall efficiency increase from around 30 % to over 50 % [86]. The hollow electron beam is widened and swept vertically over the collector by additional coils to spread the remaining energy over a larger area.

The transmission of the microwave beam from the gyrotrons to the plasma can be either carried out by oversized hollow wave guides or in free space with quasi optical focussing metal mirrors. The launch of the beam into the plasma is achieved quasi optically. Steerable mirrors at the front end of the launching system allow a flexible and precise deposition of power. The launching mirror system, the beam path and the absorption area for one gyrotron are shown in figure 3.4 (b). The beam paths and absorption areas of all eight gyrotrons can be seen in figure 3.1 in the toroidal projection as coloured dashed curves, respectively black lines.

The typical operation mode at ASDEX Upgrade is the X2 mode. The wave is absorbed at the second harmonic of the cyclotron frequency and the polarisation of the wave is adjusted in such a way that the extraordinary contribution is maximised. This means that the wave is elliptically polarised, perpendicular to the background magnetic field. However, a small contribution of typically up to one percent of the ordinary polarisation cannot be avoided depending on the gyrotron and injection geometry [87]. This fraction of the radiation has a different resonance condition and is not absorbed directly. It can lead to high and localised power deposition on the plasma facing components. Metal surfaces inside the vessel reflect this ECRH stray radiation without notable energy absorption. However, other materials used in the vacuum vessel, such as plastic or rubber isolations, serve as good absorbers and can be damaged. Accordingly the avoidance and detection of stray radiation is an important task for machine protection and safe operation [88].

The electron cyclotron frequency  $\omega_{ce}$  in the centre of the plasma at a magnetic field of 2.5 T has a value of 70 GHz so the e.m. wave is absorbed at the second harmonic. The radial location is determined on one side by the strength of the magnetic field which decays with  $1/R$  and on the other side by the resonance frequency of the ECRH radiation.

Tilting the last mirror allows the steering of the beam up- and downwards which influences the vertical location of the absorption. This allows a large variation of the radial energy deposition location. At perpendicular injection the absorption length along the beam is a few mm. Perpendicular to the beam the absorption area is determined by the focus of the mirror system and lies in the range of 3 cm. The absorption volume is localised typically within less than  $10 \text{ cm}^3$  and allows a precise fine tuning of the heating. Depending on the injection angles the absorption area can be widened to up to 10 cm in radial direction. After deposition the energy is spread rapidly on the flux surface due to large parallel conductivity along the field lines.

The particular characteristic of the ECRH, namely heating only the electrons but not the ions, represents an important qualification for detailed physical studies in this work. It provides the unique advantage to simulate future reactor conditions in which the electron heating will dominate as pointed out in chapter 3.1. Additionally the ECRH system provides several other experimental advantages due to its flexible operation. A localised co- or counter-current can be driven by steering the beam in toroidal direction. This can be used to tailor the current distribution which modifies the q-profile. It is also possible to stabilise MHD modes like NTMs with the fast responding mirrors by heating or driving current inside the island or even only inside the O-point of the island [89]. However, for this work only the heating of the ECRH system was utilised. The transient behaviour produced by heat pulses travelling through the plasma can be studied by fast modulation of the ECRH power of up to 500 Hz [90]. Localised heating in the centre of the plasma enhances the radial outward transport of heavy elements significantly and accumulation of impurities can be avoided or cured. This technique is applied regularly since the inner wall of ASDEX Upgrade is completely covered with tungsten heat shield tiles. Despite the low sputtering yield of tungsten the large area of all plasma facing components of  $35 \text{ m}^2$  leads to a significant tungsten source [91]. Without countermeasures this results typically in impurity accumulation, increased radiation, MHD activity and finally disruption of the discharge. For that reason NBI or ICRH only discharges without a small ECRH contribution in the core for impurity flush out are not feasible.

At ASDEX Upgrade 2 systems of Gyrotrons are installed. The first one consists of 4 units, gyrotron 1 to 4. Each one is able to deliver up to 400 kW for maximum 2 seconds [92]. The second system consists of 4 units, gyrotron 5 to 8, each designed to deliver up to 1 MW for maximum 10 seconds [82]. However, the design values of the second system were not reached during this thesis and not the full capacity of the ECRH could be exploited. The high performance gyrotrons suffered from flashovers at the internal isolator and quenches of the superconducting 5 T magnets. Accordingly they were not constantly available for experiments. One gyrotron had to be shipped back to Russia to the manufacturer Gycom to repair it within its warranty. At high powers electrical arcs can occur in the transition lines, preferentially at dust particles. Therefore the lines have to be conditioned with increasing pulse length and power level, which is a tedious process. In addition the microwave beams suffer from various losses on their way from the gyrotrons to the plasma, e.g. mirrors, transmission lines, polarisers and windows. For these reasons the injected power into the plasma was in the range of 700 to 800 kW per gyrotron, an

### 3.3. ELECTRON CYCLOTRON RESONANCE HEATING

amount, which can be substituted by one neutral beam with reduced acceleration voltage.

The deposition profiles of power ( $P_{ECRH}$ ) and current ( $j_{ECRH}$ ) can have various shapes and positions due to flexible injection geometry and multiple operation parameters of the ECRH system. At ASDEX Upgrade they are calculated for each case with the beam tracing code Torbeam [48]. It accounts the path and absorption of a Gaussian ECRH wave front for real experimental equilibria in the short wavelength limit. The path of the central beam is computed via ray tracing while for the wave front also wave effects such as diffraction are considered. This description allows to take into account the diffractive broadening of the ECRH beam, which leads to a wider absorption profile compared to the only geometrical considerations used in ray tracing.

A comparison of the typical power deposition profiles of ICRH, NBI and ECRH going to electrons and ions is shown in figure 3.5. The power profiles of each heating system sums up to 1 MW absorbed power. The NBI heating profiles show the calculations for beam 3 of the SE NBI with  $E_{kin} = 60$  keV. For the ECRH two individual cases are shown. One with perpendicular injection and most localised central absorption and the other one with large toroidal and poloidal injection angles to maximise the width of the deposition. The central case was scaled down by a factor 50 to enable a better comparison with the other profiles. All shown cases have central electron temperatures of around 2 keV and central electron densities of around  $9 \cdot 10^{19} \text{m}^{-3}$ .

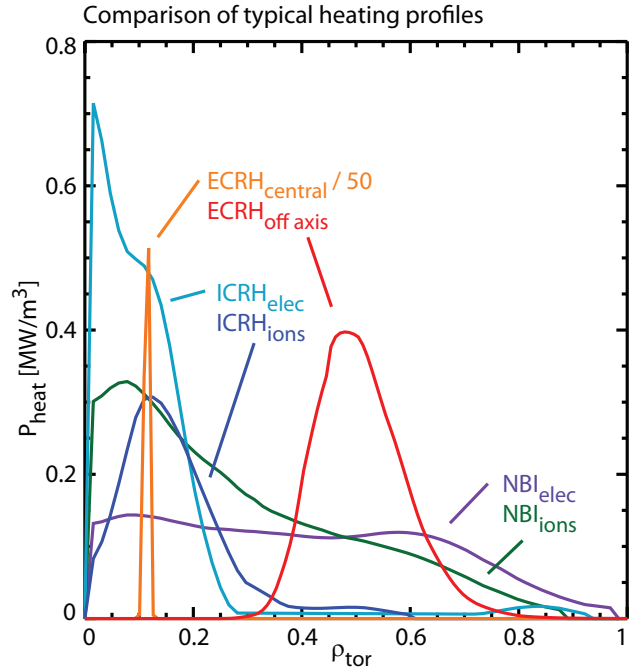


**Figure 3.5:** Comparison of the power deposition profiles to electrons and ions by ICRH, NBI and ECRH. The profiles are normalised to 1 MW of total heating power per system going to the plasma. The central ECRH case was divided by 50 to enable a comparison in the same plot.



# Chapter 4

## Diagnostics of ASDEX Upgrade

Besides the flexible heating systems, ASDEX Upgrade is equipped with a large number of diagnostics measuring a wide range of different plasma parameters and operational quantities. This work is mainly based on the measurement of the electron temperature and density, the ion temperature and rotation and the plasma radiation. In this chapter the relevant diagnostics are presented which are most important for this work. Additionally special requirements of them in the scope of this work are discussed.

The toroidal and poloidal location of the presented diagnostics are illustrated together with the heating systems in figure 3.1 and figure 3.2.

### 4.1 Electron cyclotron emission spectroscopy

The electron temperature  $T_e$  is typically measured with the Electron Cyclotron Emission (ECE) spectroscopy at ASDEX Upgrade [93]. This diagnostic uses a process inverse to the ECRH. It measures the cyclotron radiation, which is emitted by the electrons during their gyration around the magnetic field lines. If the plasma is optical thick ( $\tau \geq 1$ ), the emission frequency  $\omega_{ce}$  is only dependent on the strength of the magnetic field. Due to the decline of the magnetic field with approximately  $1/R$  the frequency of the emitted radiation decreases with increasing radius. In fusion experiments the main part of the plasma is typically optical thick. Therefore the intensity of the radiation  $I_{RJ}$  depends only on the electron temperature and can be approximated by the Rayleigh-Jeans formula since typically the condition  $\hbar\omega_{ce} \ll k_B T_e$  is fulfilled [6]:

$$I_{RJ} = \frac{\omega_{ce}^2}{8\pi^3 c^2} k_B \cdot T_e \quad (4.1)$$

Accordingly a spectrally resolved measurement of the intensity leads to a radial profile of the electron temperature along the line of sight.

The emission frequency is broadened due to Doppler effects and relativistic mass increase. Most regions of the plasma are optically thick at the respective microwave frequency and the description of the plasma as a black body radiator is valid. Parts of the broadened emission profile, which are created further inside the plasma are reabsorbed near the cold resonant locations. For that reason the emerging emission is narrowed and close to the cold resonance. Under these conditions, the electron temperature is equal to the observed radiation temperature. However, in regions where the density is too small and the plasma becomes optically thin ( $\tau \leq 1$ ), these approximations are not valid anymore and the broadening of the emission profiles has to be taken into account. For the second harmonic of the X mode, which is measured by the ECE, the optical depth can be approximated by

$$\tau_{X2} \approx 3.9 \cdot 10^{-19} n_e [\text{m}^{-3}] \cdot T_e [\text{keV}] \quad (4.2)$$

For the analysed discharges this transition lies typically around the separatrix. A forward modelling was recently developed at ASDEX Upgrade which allows the analysis under these conditions and a correct interpretation of the radiation profiles [93]. This analysis could not be performed on a regular basis for this work. For that reason the electron temperature of the ECE outside the separatrix was excluded from the analysis. A second limitation of the ECE system applies to densities above the cutoff density [11]:

$$n_c = \frac{\epsilon_0 \cdot m_e}{e^2} \approx 1.94 \cdot 10^{19} B^2 \quad (4.3)$$

The ECE radiation of a specific frequency coming from further inside is reflected at this density layer and cannot reach the diagnostic. This limits the accessible densities to  $12.1 \cdot 10^{19} \text{m}^{-3}$  for 2.5 T and  $6.3 \cdot 10^{19} \text{m}^{-3}$  for 1.8 T discharges. Latter prohibits the electron temperature measurement by ECE in the low magnetic field discharges performed during this work.

At the edge a radial resolution of approximately 0.5 cm can be achieved, while the optics limit the resolution in the other two directions parallel to the flux surfaces to 5 to 7 cm [94]. The diagnostic has a fast sampling rate of up to 1 MHz which allows to resolve the fast changes of electron temperature during sawtooth cycles and ELM crashes. The systematic error resulting from the calibration of the diagnostic lies for discharges before 04.04.2012 in the range of 18 %, after that in the range of 10 %. These errors apply, if the data is averaged over a time period, which is applied in this work, and not taken from a single time slice only.

The toroidal and poloidal measurement locations of all channels are shown in figure 3.1 and figure 3.2 as black circles for a typical 2.5 T discharge.



## 4.2 Thomson scattering

At ASDEX Upgrade the electron temperature can also be measured with the Thomson scattering system [95, 96]. This method is based on the scattering of photons from a laser by free electrons in the plasma. The electron density can be determined by the number of scattered photons. The electron temperature can be inferred from the spectral distribution of the scattered light. Due to a Maxwellian velocity distribution of the electrons which are in thermal equilibrium, the scattered intensity is given by [77]:

$$I_{TS} \propto \sqrt{\frac{m_e}{2\pi \cdot T_e}} n_e \cdot e^{-\frac{m_e \cdot v^2}{2k_B \cdot T_e}} \quad (4.4)$$

The cross section of Thomson scattering is very small and lies in the range of the square of the classical electron radius:

$$r_e^2 = \left( \frac{e^2}{4\pi\epsilon_0 \cdot m_e \cdot c^2} \right)^2 \approx (2.8 \cdot 10^{-15})^2 m^{-2} = 8.0 \cdot 10^{-30} m^{-2} \quad (4.5)$$

With high beam power and minimised stray light a good signal to noise ratio is achieved. A recent upgrade of the system allows the measurement of the core and the edge simultaneously [96]. A Nd-YAG laser with a wavelength of 1065 nm propagates vertically through the plasma at two radial locations. Four lasers are in use for the core and 6 for the edge system, each emitting 1 J in 15 ns with a repetition rate of 20 Hz. This leads to a snapshot of the electron temperature profile every 12.5 ms for the core and every 8 ms for the edge. The toroidal and poloidal traces of the lasers and the measuring locations of the Thomson scattering system can be seen in figure 3.1 as brown crosses and in figure 3.2 as brown dashed lines. One laser passes through the edge close to the separatrix measuring the edge and the scrape off layer (SOL). The other one is located close to the core allowing a measurement of the core part of the plasma. Optics view the laser beams from the side and capture the scattered light.

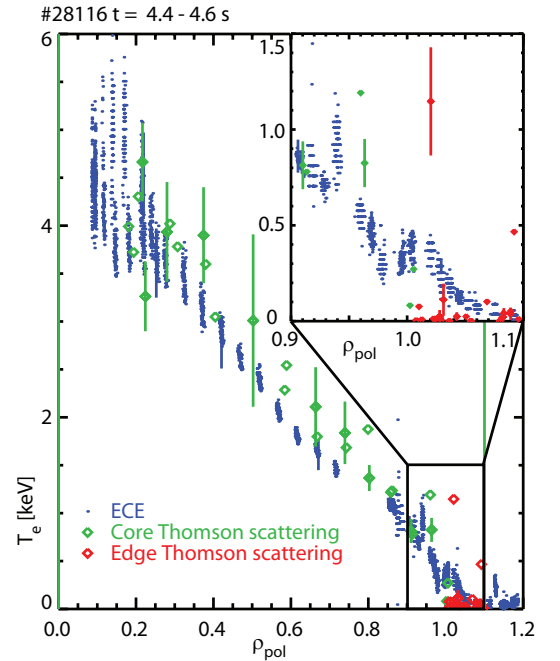


**Figure 4.1:** Comparison of ECE and Thomson scattering data.

The electron temperature deduced from Thomson scattering agrees very well with ECE data for the temperature range reached in this work (up to 5 keV). A comparison of the electron temperature measured with ECE and with Thomson scattering is shown in figure



4.1. The data is accumulated over a 200 ms time window in which the plasma parameters stay constant. Only taking the data between ELMs the two diagnostics agree very well within the error bars. Typically the Thomson scattering system has lower temporal resolution and larger uncertainties than the ECE. However, it is not hampered by high densities where ECE can be in cutoff and is not able to take measurements. Therefore Thomson scattering is only used for discharges where no data from ECE is available.

### 4.3 Charge exchange recombination spectroscopy

The ion temperature  $T_i$ , the toroidal plasma rotation in the core and at the edge,  $v_{tor}$  and  $v_{tor, edge}$ , and the poloidal rotation at the edge,  $v_{pol, edge}$ , is measured using the charge exchange recombination spectroscopy system (CXRS) at ASDEX Upgrade [97]. Additionally the impurity density can be inferred from the intensity of the observed radiation. This method uses charge exchange collisions of fast neutrals of the NBI beam with fully ionised impurity ions in the plasma, which are in thermal equilibrium with the main ion species (typically deuterium). During the charge exchange collision the electron is transferred from the neutral atom to the impurity ion. The impurity ion remains in an excited state, falls into the ground state and thereby emits a photon with a specific frequency. Electrons in different excited states form a particular spectrum for each element. The emission process is so fast, that the measured light holds the information of the fully ionised atom, such as the Doppler-shift due to the velocity of the ion. The temperature of the observed impurity ion can be deduced from the Doppler width of the spectral lines. The velocity along a line of sight can be calculated from the Doppler shift of the observed peak to their natural emission line frequency. Depending on the impurity content of the plasma, typically boron  $B^{5+}$  or carbon  $C^{6+}$  are observed.

The CXRS diagnostic at ASDEX Upgrade consists of four different systems: One toroidal core system looking at beam number 8 has a rather poor resolution and low sensitivity and is only used in this work if the other systems are not available (CHZ). The other three systems are looking at beam 3: all systems deliver the ion temperature and impurity concentrations in the region covered by the optics. Additionally the toroidal core system (CEZ) delivers the toroidal rotation of the core plasma, the toroidal edge system (CMZ) measures the toroidal rotation at the edge and the poloidal edge system (CPZ) provides the poloidal rotation at the edge. In this work the ion temperature data of the edge systems are combined with the data of the core system to one single profile if both measurements are available.

The core systems CEZ and the toroidal edge system CMZ have been upgraded recently to increase the spatial resolution and the signal level, which allows a higher temporal resolution [97]. The core system has a radial resolution of 2 to 2.5 cm. It covers the plasma cross section at the midplane on the low field side from the plasma edge up to the core with 30 lines of sight. The minimum exposure time can be as low as 4 ms

### 4.3. CHARGE EXCHANGE RECOMBINATION SPECTROSCOPY

---

if the concentration of the observed impurity species is high enough to obtain a decent signal to noise ratio. The edge system has 8 LOS covering the outermost 9 cm of the plasma up to the separatrix which leads to a radial separation of the channels of 1.1 cm. The radial extension of the measurement region is only 3 mm. For that reason a radial sweep of the separatrix position on the low field side  $R_{out}$  by about 1.5 cm is performed regularly to utilise the full capacity of the diagnostic. To this end the ion temperature and rotation profiles are swept past the measurement volumes to gain a better radial resolution and an overlap of the measurements of the channels. This allows a cross calibration between channels and a precise evaluation of the gradients of ion temperature, density and rotations. The new poloidal edge system covers the outermost 10 cm of the plasma with 8 LOS, which leads to a radial separation of the channels of 1.3 cm and a radial extension of the measurement of only 5 mm. For the poloidal system the radial resolution is also increased by performing radial sweeps of the low field side plasma position. The exposure time is 2.2 ms for both edge diagnostics.

As mentioned in chapter 3.1 the beam voltage and thus the beam power of the NW NBI injector was reduced in order to vary the NBI heating power in smaller steps. The voltage of the SW NBI was kept at its maximum value of 60 keV to increase the signal of the CXRS measurements. A lower acceleration voltage would lead to a stronger attenuation of the beam and it would not reach the core of the plasma. This would hamper ion temperature and plasma rotation measurements in the central part of the plasma, which would mean the loss of one of the major diagnostics of this work. However, the ion temperature and rotation should also be measured in periods of the discharges with low NBI powers, which did not allow the use of the full 2.5 MW heating power from one source with full acceleration voltage. For that reason 16 ms long beam blips with full voltage from beam 3 of the SE NBI injector were introduced allowing CXRS measurements up to the core [98]. Owing to the short duration of the beam blips and a duty cycle of 15 %, their energy deposition could be kept small enough to leave the plasma temperature and rotation as unperturbed as possible while allowing reasonable  $T_i$  and  $v_{rot}$  measurements. For each analysed phase with beam blips the time averaged power injected by the beam blips  $\langle P_{NBI,blips} \rangle$  is less than 10 % of  $P_{aux, total}$  and the on-time of the beam  $\tau_{blip}$  is less than 15 % of  $\tau_E$ . The timing of the 16 ms beam blips was done in a way that the first half of the first 4 ms frame of the CXRS core system lies in the rising edge of the beam power. The second half is in the full power phase in which the beam is still stabilising. Due to the accompanying fluctuations this frame cannot be used for the analysis. The next three frames provide  $T_i$ ,  $v_{tor}$ ,  $v_{tor, edge}$  and  $v_{pol, edge}$  measurements and are used for the analysis. The last frame is covering the switch-off of the beam and is discarded. However, the introduction of beam blips prevents the analysis of the radial electric field  $E_r$  (see chapter 5.4). Despite the timing of the beam blips with the radial sweeps of the plasma edge the data points are radially not dense enough to allow a sufficient precise evaluation of the edge impurity density gradients. Additionally the signal to noise ratio drops considerably when using beam blips. For that reason the analysis of the electric field was only possible in discharge phases with a constant NBI power of 2.5 MW from beam 3.

The systematic error of the CXRS system depends strongly on the specific discharge con-

dition e.g. the density and beam voltage (NBI beam attenuation), the boron concentration (signal strength) or stability of the NBI beam (beam blips). For the analysed discharges typically the errors range from 3 % around mid radius to 10 % in the center and at the edge for good measurement conditions. For beam blip analysis these errors can increase to 20 to 30 %. The systematic error of the rotation measurement is slightly higher by 1 to 2 % arising from an additional source of error from the wavelength calibration.

The toroidal and poloidal measuring locations of all four systems are shown in figure 3.1 and figure 3.2 as orange (CHZ), green (CEZ), red (CMZ) and blue (CPZ) crosses.

## 4.4 Lithium beam emission spectroscopy

The electron density at the edge is measured with the Lithium beam emission spectroscopy (LIB) [99]. A neutral Lithium beam is injected horizontally into the plasma at the mid plane from the low field side with energies of up to 60 keV. The lithium atoms are excited by collisions with electrons. The beam is viewed vertically by the optics. They measure the intensity of the  $Li_I(2s - 2p)$  line which is dependent on the electron density and the local intensity of the beam. The local intensity of the beam itself depends on the initial intensity and the attenuation on its path further inside the plasma. The attenuation depends on the density and is modelled taking into account the excitation and ionisation of Lithium atoms by collisions with electrons, but also with deuterium and impurities. Especially at high beam energies the  $Li_I$  states are also de-excited by collisions which has to be taken into account. The profile of the electron density can be reconstructed from the local form of the emission intensity profile. Details on the computation of the electron density profile can be found in reference [100].

The optical lines of sight cover the entire SOL and roughly the outermost 5 cm of the confined plasma depending on the separatrix position. For high electron densities the beam is attenuated completely before reaching the innermost channels, so that the radial extent of the measurement depends on the plasma density itself. A radial resolution of 0.5 cm and a sampling rate of up to 20 kHz can be achieved while densities up to  $8 \cdot 10^{19} \text{m}^{-3}$  can be measured. The beam is shown in figure 3.1 and figure 3.2 as magenta lines.

## 4.5 DCN interferometer

The Lithium beam determines the edge profile of the electron density with great accuracy but does not penetrate far enough into the plasma to give any information about the core part. The electron density in the main plasma region is measured with the DCN interferometer system [101], which delivers the electron density line integrated along the line of

sight. The fundamental principle of this diagnostic is based on the phase velocity change  $v_{ph}$  of an electromagnetic wave in a plasma with changing plasma frequency :

$$v_{ph} = \frac{\omega}{k} = \frac{c}{\sqrt{1 - \frac{\omega_p^2}{\omega^2}}} \quad (4.6)$$

$\omega_p$  stands for the plasma frequency:

$$\omega_p = \sqrt{\frac{e^2 \cdot n_e}{\epsilon_0 \cdot m_e}} \quad (4.7)$$

The plasma frequency depends only on the electron density while all other contributions of this relation are constant. The increasing plasma frequency with increasing density leads to an increasing phase velocity and a phase difference  $\phi$  between the beam going through the plasma and a reference beam. By integration of the density along the line of sight and expansion in  $\frac{\omega_p}{\omega}$  this phase change can be calculated:

$$\phi = 2\pi \frac{L_{geometry} - L_{optic}}{\lambda_0} = \lambda_0 \cdot r_e \int_0^{l_{geometry}} n_e(x) dx \quad (4.8)$$

$\lambda_0 = \frac{2\pi c}{\omega}$  stands for the vacuum wavelength of the laser and  $r_e$  for the classical electron radius. Using an interferometer, this change in phase can be detected and the line integrated electron density can be calculated.

Since the phase change is proportional to the wavelength of the laser it should be maximised. However, electromagnetic waves in the mm-range (microwave range) suffer from deflection by transversal density gradients. On the other side of the spectrum infrared or visible light suffers from phase changes by vibration of the optical system of the order of  $2\pi$  or more which are typically unavoidable. Both effects hamper the measurement and huge technical efforts have to be performed to compensate for each effect in a real experimental environment. Hence a deuterium cyanide laser was chosen which lies between these two extreme values. It has a wavelength of  $195 \mu\text{m}$  (1.5 THz).

ASDEX Upgrade is equipped with five lines of sight which are tangential to different flux surfaces. The laser is shot through the plasma, reflected at the inner wall and travels back to the detection system almost on the same path to increase the measuring length. The phase change is detected with a Mach-Zehnder-type heterodyne interferometer. The toroidal and poloidal paths of the lasers are shown in figure 3.1 and figure 3.2 as cyan lines. With an Abel inversion, the core density profile can be reconstructed. When taking only the data of the DCN interferometer, an exponential decay of the profile is routinely assumed for the edge at ASDEX Upgrade.

## 4.6 Bolometry

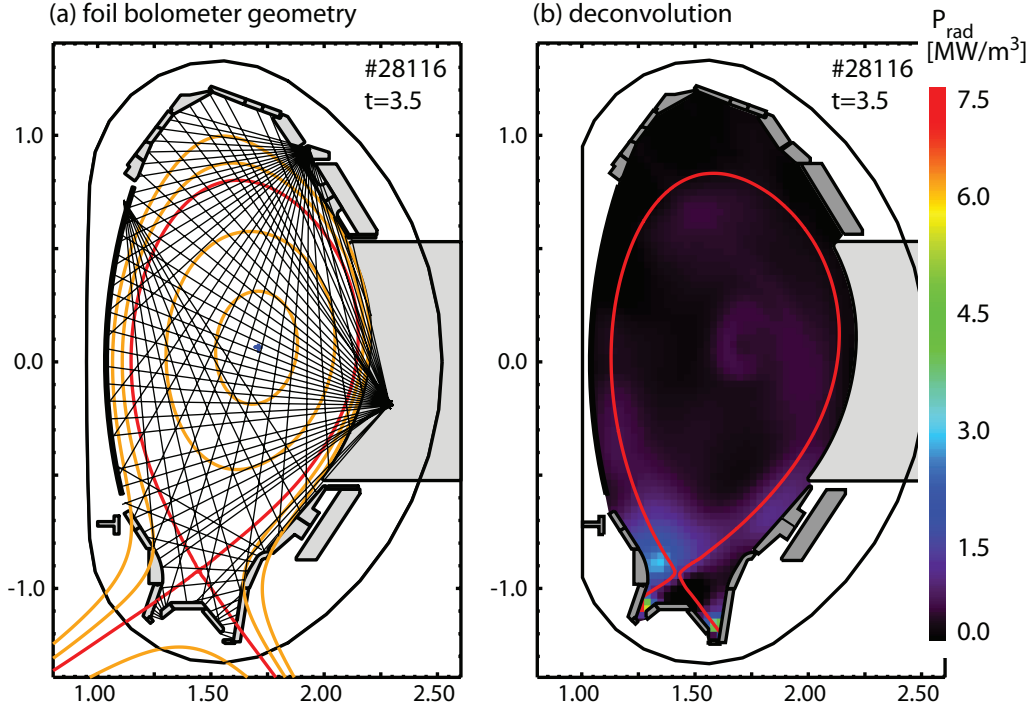


**Figure 4.2:** Plot (a): Poloidal view of the lines of sights of the foil bolometers. Plot (b): Example of a 2D deconvolution of the radiation pattern at ASDEX Upgrade.

The radiated power of the plasma  $P_{rad}$  at ASDEX Upgrade is measured in a broad photon energy range ( $\sim 1$  eV to 8 keV) with absolute extreme ultraviolet radiation (AXUV) diode and foil bolometers [102, 103]. The diode bolometers allow in comparison to the foil bolometers a much higher temporal resolution and also have a better spatial resolution, but they cannot measure absolute radiation values. Their response is not constant over the spectrum of the emitted radiation, which depends on the plasma composition and temperature. Furthermore, they degrade with time in a non linear way, so that the extraction of a quantitative radiation from the measured signals is not directly possible [102]. However, they are suitable for the localisation of fast radiation events and for the relative comparison of different phases during one discharge and also between different discharges.

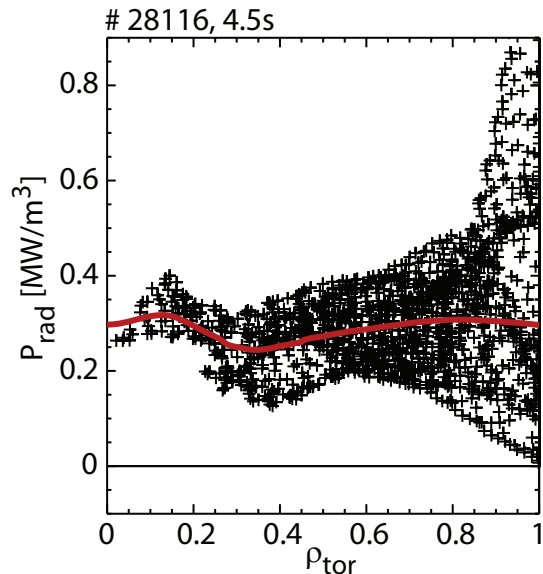


**Figure 4.3:** Radial profile of the plasma radiation obtained by mapping the poloidal deconvolution on a radial grid.

The foil bolometry system detects the radiation by the measurement of the temperature increase of a  $4.5 \mu\text{m}$  thin gold or platinum foils, exposed to the plasma radiation. This system is used in this work to detect the quantitative level of radiation. The toroidal and poloidal positions of the measurements of both bolometry systems are indicated in figure 3.1 and 3.2. The poloidal locations of the lines of sight of the foil bolometers is shown in more detail in figure 4.2 (a). The cameras are mounted at different poloidal locations in the vacuum vessel with crossing lines of sights. Due to the resulting grid of lines of sight a 2D representation of the emitted radiation can be calculated by a deconvolution of the line integrated measurements. An example can be seen in figure 4.2 (b). The increased radiation at the target plates in the divertor and near the X-point is clearly visible. In the centre a small increase of the radiation is visible, which probably arises from an accumulation of heavy ions. By mapping the poloidal deconvolution on a radial grid a poloidally averaged radial profile of the plasma radiation is obtained (see figure 4.3). The black crosses represent all points of the 2D deconvolution mapped on  $\rho_{tor}$ . The red line shows the spline fitted radial profile of the plasma radiation which is used as input for the power balance analysis performed with ASTRA in chapter 5.3 and the modelling of the kinetic profiles with TGLF in chapter 6.1. The upper limit of the error of the radial profile can be estimated by the variation of the data at one radial location caused by the poloidal asymmetry of the radiation. Except in the very edge this spread lies in the range of roughly 30 % [104].

## 4.7 Integrated data analysis

Instead using an exponential decay at the edge, the core electron density profile from the DCN can also be combined with the edge profile measured by the LIB diagnostic. The exact experimental shape of the edge profile replaces the assumption of an exponential decay and changes the result of the Abel inversion. Additionally the value of the electron density affects the determination of the electron temperature from the radiation temperature especially at the edge [93]. For that reason at ASDEX Upgrade an integrated data analysis (IDA) was developed, which includes a forward modelling of the measured quantities and combines them in a probabilistic model [105]. This approach includes the data of the ECE, the LIB and the DCN interferometer and can be extended also to the Thomson Scattering, if no data are

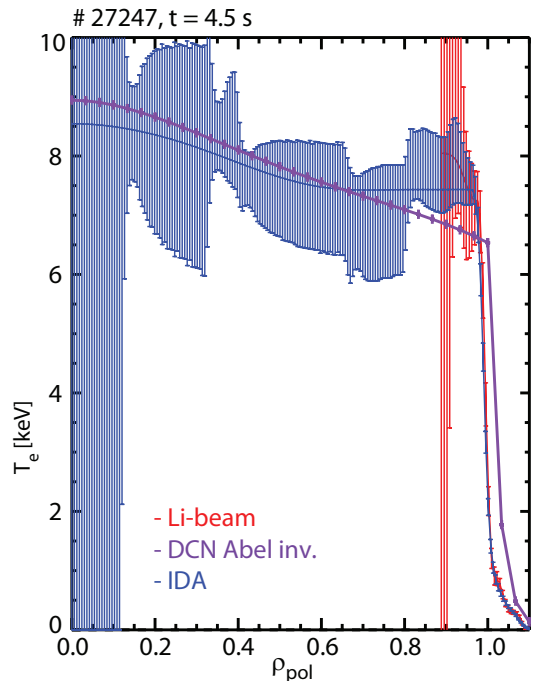


**Figure 4.4:** Comparison of a density profile obtained from the IDA approach with the ones obtained from the Lithium beam and DCN interferometer only.

available from the other diagnostics. Also the profile of the effective charge of the plasma  $Z_{eff}$  can be calculated with this method. As an example the independent LIB edge data (red) and the DCN deconvolution (purple) is compared with the combined IDA approach in figure 4.4. The vertical lines are the error bars of the LIB and a confidence interval of the IDA diagnostic. Clearly visible is the determination of the edge profile from the Lithium beam, which typically results in higher edge values than from the DCN interferometer. This localisation of density lowers the central part of the profiles slightly in the IDA approach.



# Chapter 5

## Experimental observations

This chapter reports the experimental observations which were conducted during this thesis. The underlying intention was to analyse the influence of the change of the heated species from dominant ion heating to dominant electron heating in an ELMy H-mode. This was achieved by modifying the heating mix from dominant NBI to dominant ECRH power, which is possible resulting from the upgraded and recently available heating resources of ASDEX Upgrade. Nowadays the workhorses of plasma heating are typically the NBI (see chapter 3.1) or ICRH (see chapter 3.2) heating systems. Both methods typically heat roughly half the ions and half the electrons, depending on plasma condition and applied heating scenario. At high plasma temperatures especially the NBI heats more and more the ions.

The aim of this work is to understand the influence of the transition from dominant ion heating to dominant electron heating on the discharge performance of high power H-modes. First results are already published in [106–108].

Chapter 5.1 describes the design of the discharges and the experimental considerations, taken into account. Following in chapter 5.2 the global discharge performance and the profile behaviour in the core of two exemplary discharges are discussed. Chapter 5.3 presents the pedestal profiles and chapter 5.4 concentrates on the analysis of the electric field  $E_r$ . The final chapter 5.5 shows parametric dependencies between various physics and engineering parameters for the database including all discharges performed.

### 5.1 Discharge design

In the course of the experimental investigations made in 2011 and 2012 a total of 36 successful discharges were performed at ASDEX Upgrade. In each discharge the total



heating power was kept constant during the discharge, while the relative contributions of NBI or ICRH and ECRH were varied to achieve the transition from mixed electron and ion heating to dominant electron heating. For each phase of one particular heating mix almost all plasma and control parameters were kept constant for a period of 1 s. This time resembles 5 to 10 energy confinement times  $\tau_E$  and is in the range of the current diffusion time:  $\tau_R$  [6].

$$\tau_R = \mu_0 \frac{r_1^2}{\eta} = \mu_0 \frac{r_1^2}{1.96 \cdot Z_{eff} \cdot \eta_S} = \mu_0 \frac{r_1^2}{1.96 \cdot 2.8 \cdot 10^{-8} \cdot Z_{eff} \cdot T_e^{3/2}} \quad (5.1)$$

Under these conditions a stable and equilibrated phase of plasma parameters was generated which could be analysed in detail. Typically in each phase a scan of the plasma position on the low field side  $R_{out}$  of around 1 cm was performed. This allows to gain a better radial resolution of the edge diagnostics with measurements at fixed radial positions like CXRS or the Lithium beam. In each discharge several control parameters were varied like magnetic field  $B_t$ , plasma current  $I_p$ , neutral density in the divertor  $n_0, div$ , total heating power  $P_{aux, total}$  or heating mix.

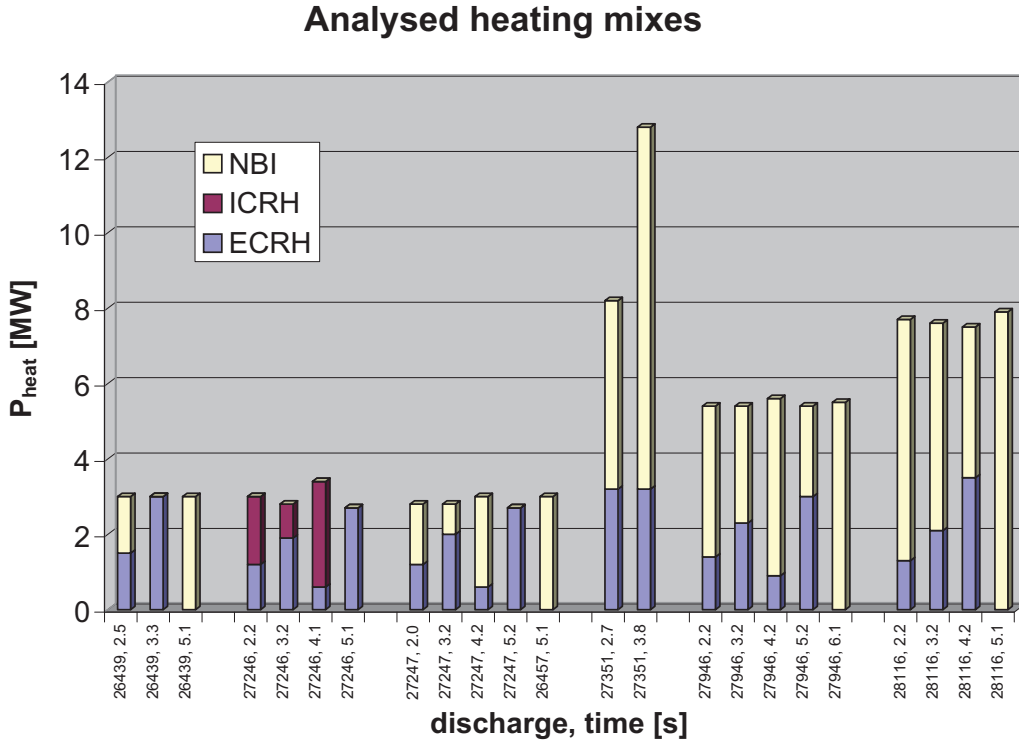


**Figure 5.1:** Overview of all analysed phases of the discharges analysed in in detail in chapter 5 comparing the heating mix of NBI, ICRH and ECRH: # 26439 comparing ECRH vs. ICRH at high collisionality, # 27246 comparing ECRH vs. ICRH at high collisionality, # 27247 comparing ECRH vs. NBI at high collisionality, # 27351 verification of TGLF and sawtooth model, # 27946 optimisation of edge measurement for radial electrical field calculations, # 28116 comparing ECRH vs. NBI at low collisionality.

An overview of all analysed phases of the six exemplary discharges presented in more detail in the following is shown in figure 5.1. All cases consist of a phase with at least 500 ms of constant, equilibrated plasma parameters. The analysed phases were taken from the end of the 1 s periods with constant control parameters to allow an equilibration of the plasma, e.g. current and heat fluxes. The heating mix consisting of NBI, ICRH and ECRH is plotted against the discharge number and time of occurrence in the discharge. The overall range of discharges covers a total auxiliary heating power between 2 and 13 MW, while the discharges with best comparability are clustered around 3 MW and 8 MW:

- # 26439: comparison of ECRH vs. NBI at high collisionality also showing the W accumulation in the NBI only phase;
- # 27246: comparison of ECRH vs. ICRH at high collisionality;
- # 27247: comparison of ECRH vs. NBI at high collisionality;
- # 27351: sawtooth free H-mode to verify TGLF and sawtooth modelling;
- # 27946: optimisation of edge measurement for radial electrical field calculations;
- # 28116: comparison of ECRH vs. NBI at low collisionality.

The ranges of the most relevant parameters and quantities that are covered by the whole database of all performed discharges are shown in table 5.1.

quantity		min. value	max. value	quantity		min. value	max. value
$P_{aux, total}$	[MW]	1.1	7.8	$v_{\rho_{tor}=0.2}^*$		0.07	0.88
$P_{NBI}$	[MW]	0.0	7.8	$v_{\rho_{tor}=0.5}^*$		0.035	0.35
$P_{ECRH}$	[MW]	0.0	3.5	$v_{\rho_{tor}=0.8}^*$		0.11	1.03
$P_{ICRH}$	[MW]	0.0	4.6	$\varepsilon$		0.06	0.27
$P_{rad}$	[MW]	1.5	5.5	$\delta_{up}$		0.03	0.11
$I_p$	[MA]	0.62	1.04	$\delta_{down}$		0.35	0.46
$W_{MHD}$	[MJ]	0.25	0.7	$f_{ELM}$	[Hz]	10	140
$B_t$	[T]	1.78	2.54	$f_{ST}$	[Hz]	0	105
$\beta_N$		0.8	3.1	$n_{0,div}$	[ $10^{20} \text{ m}^{-3}$ ]	0.5	10
$H_{98}$		0.6	1.3	gas puff	[ $10^{21} \text{ D/s}$ ]	0.8	35
$\tau_E$		0.05	0.16				
$n_{e,\rho_{tor}=0.2}$	[ $10^{19} \text{ m}^{-3}$ ]	5.9	9.8	$n_{e,\rho_{tor}=0.8}$	[ $10^{19} \text{ m}^{-3}$ ]	3.9	8.1
$T_{e,\rho_{tor}=0.2}$	[keV]	0.9	3.7	$T_{e,\rho_{tor}=0.8}$	[keV]	0.3	1.2
$T_{i,\rho_{tor}=0.2}$	[keV]	0.9	3.3	$T_{i,\rho_{tor}=0.8}$	[keV]	0.3	1.0
$v_{tor,\rho_{tor}=0.2}$	[km/s]	20	150	$v_{tor,\rho_{tor}=0.8}$	[km/s]	0.0	50

**Table 5.1:** Range of most relevant parameters and quantities covered in this thesis.

Heating phases with NBI only lead in general to a strong tungsten accumulation, a situation regularly observed at ASDEX Upgrade when no central ECRH is applied. A strong increase of the concentration of tungsten  $c_W$  can be seen in figure 5.2 at 4.9 s as soon as the central ECRH power is switched off leaving the NBI the only heating source. Empirical

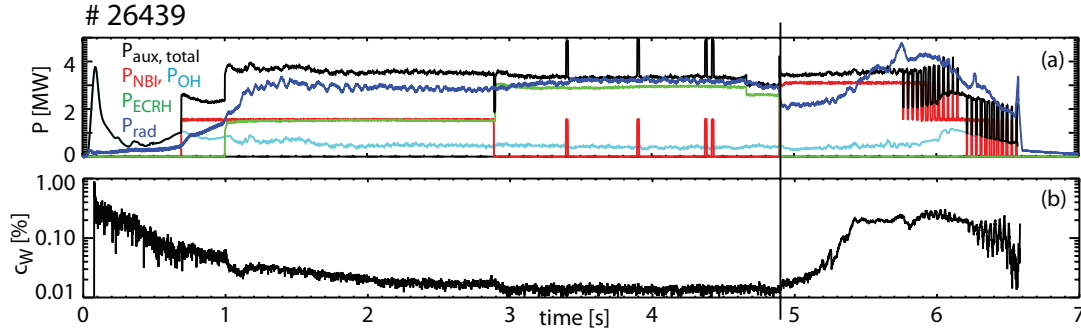


**Figure 5.2:** Plot (a): Total heating power (black), ohmic (light blue), NBI (red), central ECRH (green) and radiated power (dark blue). The total power was kept constant at 3 MW while the contributions of NBI and ECRH were modified. Plot (b): tungsten concentration in the inner part of the plasma on a logarithmic scale. A strong increase of the tungsten concentration can be observed as soon as the ECRH power is switched off completely at 4.9 s, leading to an increased plasma radiation.

observations show that deposition of the ECRH power inside the  $q = 1$  surface increases the radial  $W$  transport and minimises the  $W$  accumulation. For that reason phases without ECRH power could only be run at the very end of the discharges since they lead to MHD activity, unstable discharges and disruptions in many cases [109]. The impurity accumulation in the centre of the plasma normally results in a pronounced increase of the plasma radiation, an energy drop and reduced electron and ion temperatures. This produces a severe modification of the power balance, which is not directly related to the change of heated species but solely caused by increased radiation due to modified plasma composition. In these cases only the first few tens of milliseconds can be analysed before the effects of impurity accumulations become too large so that the comparability with other phases is not given anymore. However, the plasma is not equilibrated in this short time for which reason the comparison of these periods is very delicate and drawn conclusions have to be considered carefully.

The situation for phases with pure ICRH is even more difficult due to additional strong tungsten influx from the  $W$ -coated ICRH antennas. In the campaign 2011 this influx in ICRH only phases was too large so that the comparison to mixed cases was not given anymore. The replacement of the limiter tiles of two ICRH antennas with boron coated tiles in the campaign 2012 led to a strong decrease of the tungsten influx, so that these experiments could be conducted [76]. However, the limiters of two antennas are still covered with tungsten limiting the total ICRH power with acceptable small tungsten influx to 3 MW. Higher heating powers which require the use of both antenna pairs lead to a considerable tungsten influx from the non boron coated limiter tiles. Similar consequences as in the NBI only cases apply. Therefore phases heated by ICRH only could not be compared meaningfully.

The time traces of the most important control parameters are shown in figure 5.3 for discharge # 27247, a typical example for the low power discharges performed. The experiments for this work are derived from the standard H-mode scenario at ASDEX Upgrade

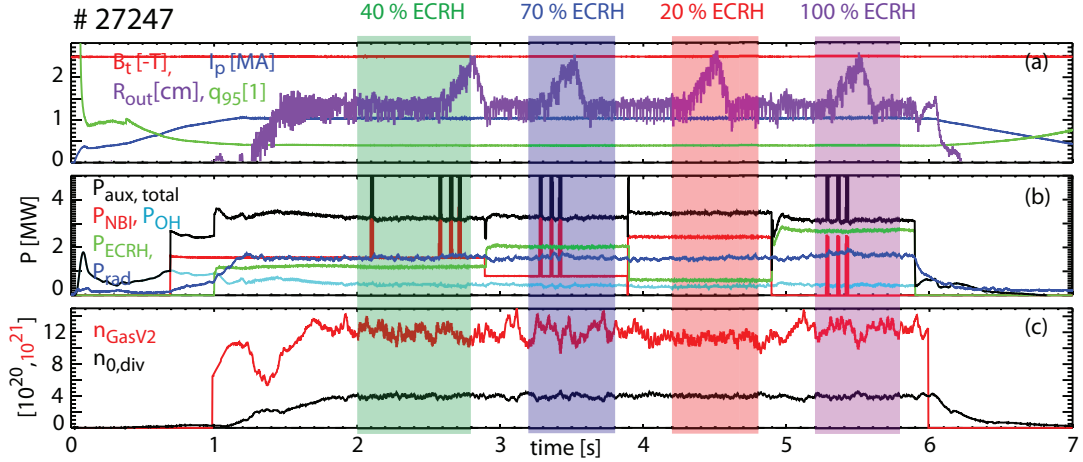


**Figure 5.3:** Overview plot of the most important control parameters of a typical discharge.

Plot (a): magnetic field  $B_t$ , plasma current  $I_p$ , the position of the separatrix on the low field side  $R_{out}$  and the safety factor at the edge  $q_{95}$ . Plot (b): total heating power  $P_{aux, total}$  (black) and the contributions of the different heating systems  $P_{OH}$  (light blue),  $P_{NBI}$  (red) and  $P_{ECRH}$  (green). The plasma radiation  $P_{rad}$  is shown in dark blue. Plot (c): actual gas puff rate  $n_{GasV2}$  and neutral density in the divertor  $n_{0,div}$ .

which is a lower single null type I ELMy H-mode. It has a magnetic field of 2.5 T and a plasma current of 1 MA. This leads to a safety factor at the edge of  $q_{95} \approx 4.1$  (all shown in figure 5.3 (a)). The shape of the separatrix on the low field side was adjusted to the contours of the outer limiter and optimised for the edge diagnostics by fine tuning the current distribution of the shaping coils. It is called edge optimised configuration (EOC shape). The scans of the Separatrix position on the low field side  $R_{out}$  which were performed to increase the radial resolution of the edge diagnostics are also shown in plot (a). It is plotted in cm with an offset of 2.13 m to make the small variations visible. A total heating power of 3.3 MW was chosen for the first discharges due to limited reliably available ECRH power at that time. Central electron density which is usually strongly coupled to the applied plasma current was in the range of  $n_e = 9 \cdot 10^{19} \text{ m}^{-3}$ . Central electron and ion temperatures of  $T_e \approx 2 \text{ keV}$  and  $T_i \approx 1.5 \text{ keV}$  were achieved. The limited total heating power allows to have phases with pure ECRH besides pure NBI and mixed cases. The NBI power per beam was reduced to 0.8 MW per source by decreasing the acceleration voltage of the NW NBI box to 52 keV as presented in chapter 3.1. In principle this allows 5 steps in heating power mix. The strong tungsten accumulation in the NBI only phase prohibits a proper analysis of the data in this case. For that reason it was sacrificed for a prolongation of the other phases and to allow smaller steps in the variation of the heating mix.

The total heating power  $P_{aux, total}$  which was kept constant throughout the entire discharge is shown in figure 5.3 (b) in black. The contributions of the different heating methods are also shown:  $P_{OH}$  in light blue,  $P_{NBI}$  in red and  $P_{ECRH}$  in green. The ECRH was typically deposited in the centre of the plasma around  $\rho_{tor} = 0.1 \pm 0.05$  inside the  $q = 1$  surface to prevent W accumulation. The phases of different heating compositions are highlighted

with coloured vertical bars. The radiated power  $P_{rad}$  is shown in the same plot in dark blue. It is constant over the entire discharge.

Due to reduced penetration depth of the NBI heating beams with reduced voltage beam blips from beam 3 were introduced for CXRS measurements in every phase in which beam 3 was not continuously used for heating, see chapter 3.1 for details. In each phase three beam blips were timed in such a way that they corresponded to the scan of the outer separatrix position  $R_{out}$  to maximise the resolution of the edge diagnostics, see chapter 4.3. Another control parameter kept as constant as possible was the neutral density in the divertor  $n_{0,div}$  which controls the gas flux into the divertor  $n_{GasV2}$  (see figure 5.3 (c)).  $n_{0,div}$  was chosen since  $n_e$  in the main chamber changes in H-modes only slightly by less than 20 % when changing the gas fluxes by an order of magnitude. The neutral divertor density follows the gas puff more closely (factor 5). In addition the pedestal top values of the electron density should be kept constant throughout the different heating phases to observe the influence of the heating mix on density peaking.

One goal of this work was to approach ITER relevant values of the Greenwald density fraction  $n_e/n_{GW}$  and the collisionality  $\nu^*$  and analyse the change in plasma response with the change of heating mix. These two quantities are correlated inversely. Accordingly the goal of this first series of discharges was to reach ITER relevant values of  $n_e/n_{GW}$  at rather low heating powers of about 3 MW. A central value of up to  $n_e/n_{GW} = 0.7$  was achieved which lead to high central collisionalities around  $\nu^* = 0.22$ . On the other side, several discharges were conducted with higher heating powers of 5 and 8 MW and possibly lower densities to approach ITER relevant collisionalities. In addition they were motivated by the following considerations:

First, the analysis of the low power discharges showed that the main changes in the plasma response occur when going from total NBI or very low ECRH fractions to about 1/2 of ECRH. Increasing the ECRH power from about 50 % to 100 % changed the performance and the kinetic profiles only marginally. Applying higher heating powers prohibits the exchange of the total amount of NBI power by ECRH which is however not a major drawback from this consideration. Consequently in further experiments the SE NBI beam with full voltage ( $E_{beam} = 60$  keV) was kept on the whole time to improve the CXRS data ( $T_i, \nu_{tor}, E_r$ ) and to rule out any disturbances of the plasma by beam blips. A total power of 5 to 8 MW was used.

Secondly, the collisionality of ITER is expected to be much smaller than nowadays namely in the range of  $\nu^* \approx 0.01$ . The main reason for this trend is the strong increase of electron temperature and only a modest increase of density. To decrease the experimental collisionality either the density can be reduced or the temperature can be increased ( $\nu^* \propto n_e/T_e^2$ ).

In general two methods are available to decrease the density of the plasma: Decrease of the gas puff and decrease of the plasma current.

1. Decrease of gas puff

The decrease of the gas puff leads to a reduction of the neutral density  $n_{0,div}$  and the pressure in the divertor. However, decreasing the density of the main plasma does function only limited. The reason for that is a strong coupling between the electron density and the plasma current both of which have a roughly linear dependency. Experimentally a decrease of the gas puff by a factor of 11 decreases the neutral density in the divertor by a factor of 5. This leads to a moderate reduction of the central density by only 20 % and of the edge density by only 10 %. This variation is too small to resolve changes of the heat transport with changing collisionality.

2. Decrease of plasma current

Due to strong coupling of density and plasma current a decrease of the current leads to a similar decrease of the density [110]. However, changing the plasma current to lower values causes a different equilibrium configuration with an increased safety factor profile when the magnetic field  $B_t$  is kept constant. This changes the stability of the plasma and introduces an additional variation of discharge conditions making the analysis of the dependency between control parameters and plasma response more complex and masking the main dependencies. The magnetic field can also be reduced to have the same q-profile as in the standard 1 MA, 2.5 T operation to avoid this added complexity. However, this demands a modified setup for the ECE diagnostic with reduced measurement frequency leading to a cutoff of the measurement for all analysed cases in this magnetic configuration. This results in the inability to determine the electron temperature, which is one of the key measurements for this work. Accordingly decreasing the current to reduce the electron density prevents any sensible analysis of discharges and is not applicable.

Therefore the density can be modified only limited and a more pronounced variation of the collisionality  $\nu^*$  can only be achieved by a variation of the temperature. It enters the formula of the collisionality with a power of 2 and can be modified easily by changing the heating power. For that reason a second series of discharges was conducted in which the total heating power was stepwise increased to  $P_{aux, total} = 8$  MW. In these discharges half of the power could be substituted by ECRH while the basic scheme of the discharge design of the low power experiments remained unchanged. The central electron densities cluster around  $n_e = 8 - 9 \cdot 10^{19} \text{ m}^{-3}$ , the central electron and ion temperatures are in the range of  $T_e = 3$  to 4.5 keV and  $T_i = 2$  to 3 keV. The increase of the heating power and decrease of the gas puff lead to a variation of the collisionality by a factor of 11. It's value ranges from 0.03 to 0.35 at mid radius.



## 5.2 Discharge performance

This chapter presents the experimental observations of the global discharge performance for two exemplary discharges. First the results from a low power, high collisionality discharge are presented. In the second part of this chapter a high power, low collisionality case is discussed. Finally, a NBI heated discharge is compared to an ICRH discharge. The typical behaviour observed in the conducted low power discharges is shown in the

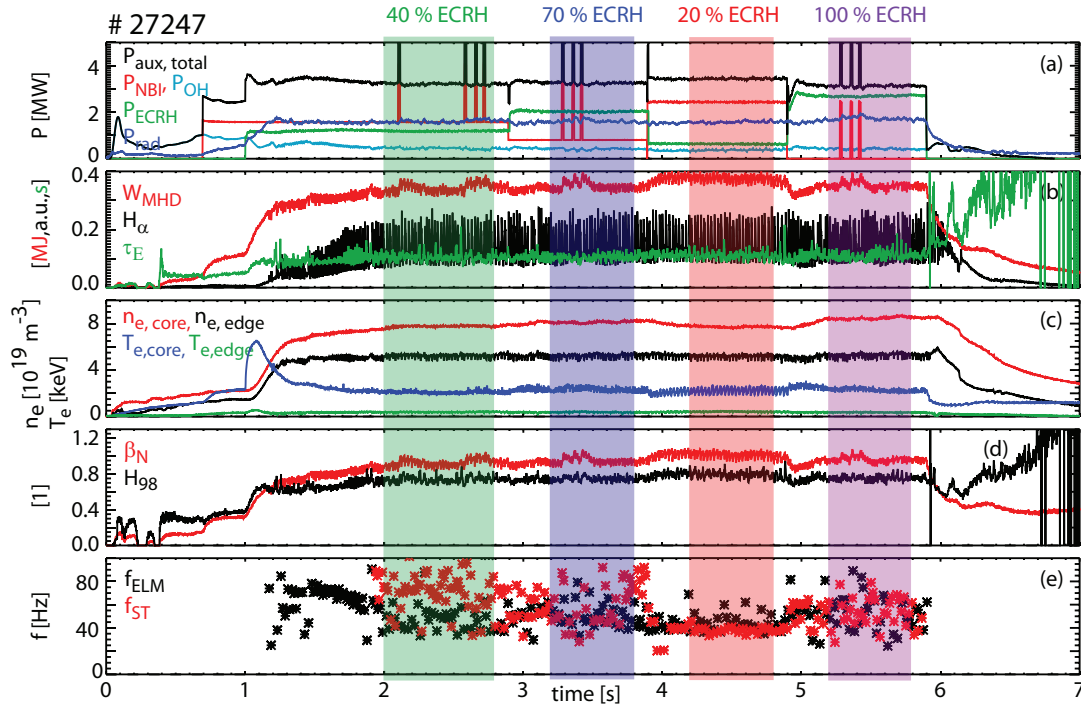


**Figure 5.4:** Overview plot of low power, high collisionality discharge # 27247:

Plot (a): total auxiliary (black), NBI (red), central ECRH (green), Ohmic (light blue) and radiated power (blue); plot (b): stored energy  $W_{MHD}$  (red) and  $H_\alpha$  radiation in the divertor (black); plot (c): line integrated density in the core (red) and at the edge (black); plot (d): normalised beta (red) and confinement factor (black); plot (e): ELM (black) and sawtooth frequency (red).

overview plot of discharge # 27247 in figure 5.4. The analysed phases of constant plasma parameters are highlighted with vertical coloured bars. The total auxiliary heating power  $P_{aux, total}$  is shown in the uppermost plot (a) in black together with the contributions of the different heating systems:  $P_{NBI}$  in red,  $P_{ECRH}$  in green and  $P_{OH}$  in light blue. The total plasma radiation  $P_{rad}$  is drawn in dark blue. The fraction of ECRH to the total plasma heating was increased from 20 % to 100 % which corresponds to an increase of the total power going to electrons from 60 % to 100 % (roughly 50 % electron heating by NBI). The total heating power was kept constant within 10 %. The only exceptions are the beam blips for CXRS measurements. The heating power level of 3.3 MW is around 2 times larger than the H-mode power threshold at these densities [111]. The total plasma radiation is constant over all heating mixes with only a slight increase of 5 %

when applying NBI blips. The  $H_\alpha$  radiation in the divertor is shown in black in plot (b). It demonstrates the typical pattern of radiation bursts due to particle and energy expulsion by ELMs. The expelled plasma is directed into the divertor region where it neutralises and excites neutral deuterium. Both processes lead to enhanced hydrogen line radiation. The stored energy  $W_{MHD}$  which is shown in red in the same plot has a value of around 0.35 MJ. The beam blips lead to a short increase of the stored energy by 10 % with an equilibration time of 50 ms. This corresponds to about half the energy confinement time  $\tau_E$  which is shown in green in this plot and has a value of 100 ms. In the third NBI dominated phase the stored energy is increased by 10 %. Here the contribution to the stored energy from fast particles could play a role which is increasing with NBI heating.

The time traces of the core and edge values of the electron density which are both line integrated measurements and the local temperature in the core and at the edge are shown in plot (c). Both the electron density with a line of sight going through the pedestal top (black) and the electron temperature measured at the pedestal top (green) experience the periodic modification by ELMs. Especially in the third phase the strong variation of the central electron temperature (blue) by sawtooth oscillations can be seen. Its disturbance of the  $T_e$  value is in the same ballpark as the  $T_e$  difference between the different heating phases.

The normalised beta is shown in red in plot (d) and has a value of around  $\beta_N \approx 0.9$ . It shows the same trend as the stored energy on the variation of the heating mix and the beam blips of the NBI. The confinement factor  $H_{98}$  being the relation between the experimental energy confinement time  $\tau_E$  and a multi machine scaling of the energy confinement time for ITER  $\tau_{E, IPB98(y,2)}$ <sup>1</sup> has values around 0.8. It follows the same trend as  $\beta_N$  but in a less pronounced way, decreasing by 5 % going from dominant NBI to ECRH only heating. The ELM frequency is shown in black in the last plot (e). It does not change with a variation of the heating mix and resides around 50 Hz. The sawtooth frequency is shown in red also in the last plot. It has the same average value as the ELM frequency but a larger scatter. However, in the phase with mainly NBI heating the scatter is reduced significantly so that only one frequency of 40 Hz remains.

All these observations show no obvious reduction of the general plasma performance when going from mixed ion and electron heating to pure electron heating at rather large collisionalities of  $\nu^* \approx 0.22$ .

In the course of this work the total heating power was increased from 3 MW to 8 MW to reduce the collisionality. Discharge # 28116 which is presented in the following shows the highest heating power performed during this work. For this reason it is among the discharges with the lowest collisionality  $\nu^*$  with a value of 0.06. The same overview plot as before is shown in figure 5.5 for this discharge. Some scales are adjusted to the range of obtained values. The discharge shows the typical behaviour observed in all performed high power experiments. The analysed phases of constant plasma parameters are highlighted with vertical coloured bars. The total heating power which was kept

<sup>1</sup> $\tau_{E, IPB98(y,2)} = 0.145 \cdot I_p^{0.93} \cdot B_t^{0.15} \cdot n_{e,20}^{0.41} \cdot P_{aux, total}^{-0.69} \cdot R^{1.97} \cdot \kappa_a^{0.78} \cdot a^{0.58} \cdot A^{0.19}$  [6]



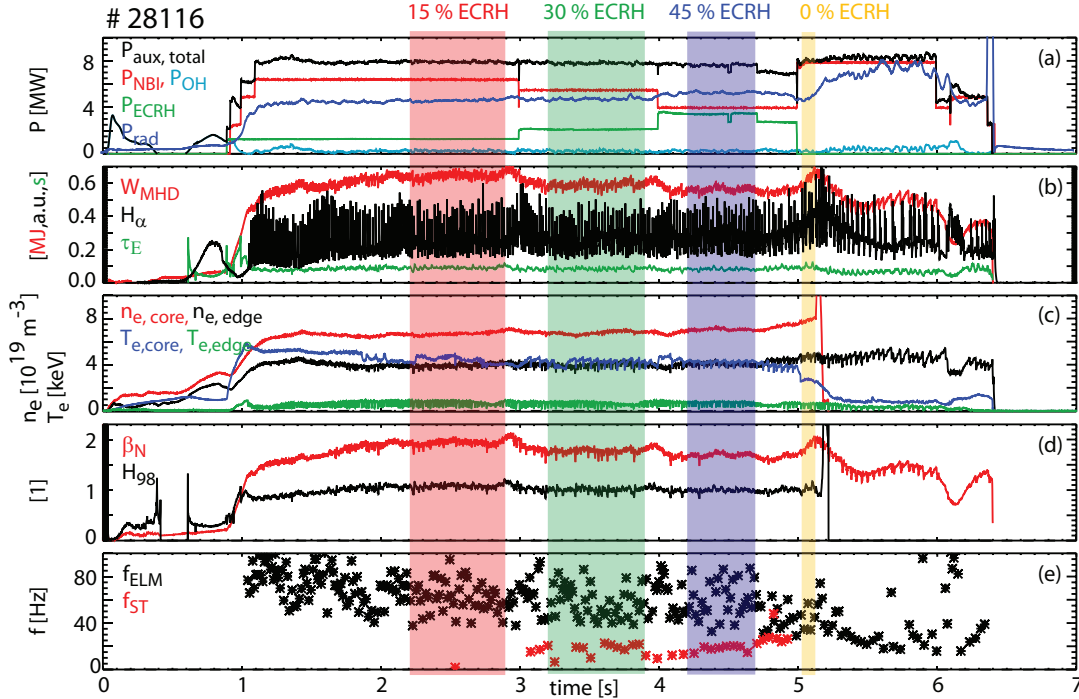


**Figure 5.5:** Overview plot of of high power, low collisionality discharge # 28116: Plot (a): total auxiliary (black), NBI (red), central ECRH (green), Ohmic (light blue) and radiated power (blue); plot (b): stored energy (red) and  $H_{\alpha}$  radiation in the divertor (black); plot (c): line integrated density in the core (red) and at the edge (black); plot (d): normalised beta (red) and confinement factor (black); plot (e): ELM (black) and sawtooth frequency (red).

constant within 5 % is shown in black in plot (a). In this discharge no beam blips were necessary due to continuous operation of the NW NBI beam 3 at a maximum beam energy of 60 keV for CXRS measurements. The fraction of ECRH power was varied between 15 % and 45 %. This corresponds to a transition from 45 % to 70 % electron heating due to distribution of NBI power to both species.

The NBI only phase in the high power discharges could not be analysed and compared to the other phases due to impurity accumulation of tungsten in the plasma which is even greater than in the low power ones. The concentration of W rises from a constant value of around 0.07 % throughout the discharge by more than a factor of 10 to roughly 1 %. A transient phase starts around 4.7 s when one gyrotron fails during the ECRH dominated phase. The change of parameters is increasing when the ECRH is switched off at 5.0 s and the NBI remains the only heating source. The density increases, the  $W_{MHD}$  shows a fluctuating behaviour and both the electron and ion temperature decrease significantly until the ECE diagnostic reaches cutoff. Finally, the discharge disrupts. Therefore the NBI only phase is excluded from the analysis of the time averaged profiles in chapter 5.3.

The radiation  $P_{rad}$  is around 5 MW throughout all heating mixes but increases by about 10 % in the third phase. The  $H_{\alpha}$  signal shows a constant ELM behaviour. The stored energy decreases by 10 % when increasing the electron heating. The fast particle con-

tribution, which is reduced with increasing ECRH fraction, could account for this effect. The energy confinement time decreases by 10 % from around 0.9 to 0.8 ms.

The edge values of the electron temperature (green in plot (c)) and density (black) are only affected by ELMs and not by the change in heating mix also in this discharge. The central electron temperature (blue) is affected by low frequency sawtooth crashes. The plasma beta shown in red in plot (d) is decreasing similar to the stored energy by 15 % with increasing electron heating. The confinement factor shows the same trend but less pronounced. The ELM frequency is centred around 60 Hz and has a large scatter of 20 Hz. The sawtooth crashes occur infrequent at a frequency of around 20 Hz in the phases with larger ECRH fraction.

In summary the global performance of the discharge (e.g.  $\beta_N$ , H-factor,  $W_{MHD}$ ) at lower collisionality is improved compared to discharge # 27247 considered before. This is expected due to increased heating power. However, the decrease of global performance with an increase of the ECRH fraction is more apparent than in the high collisionality cases but still not very pronounced.

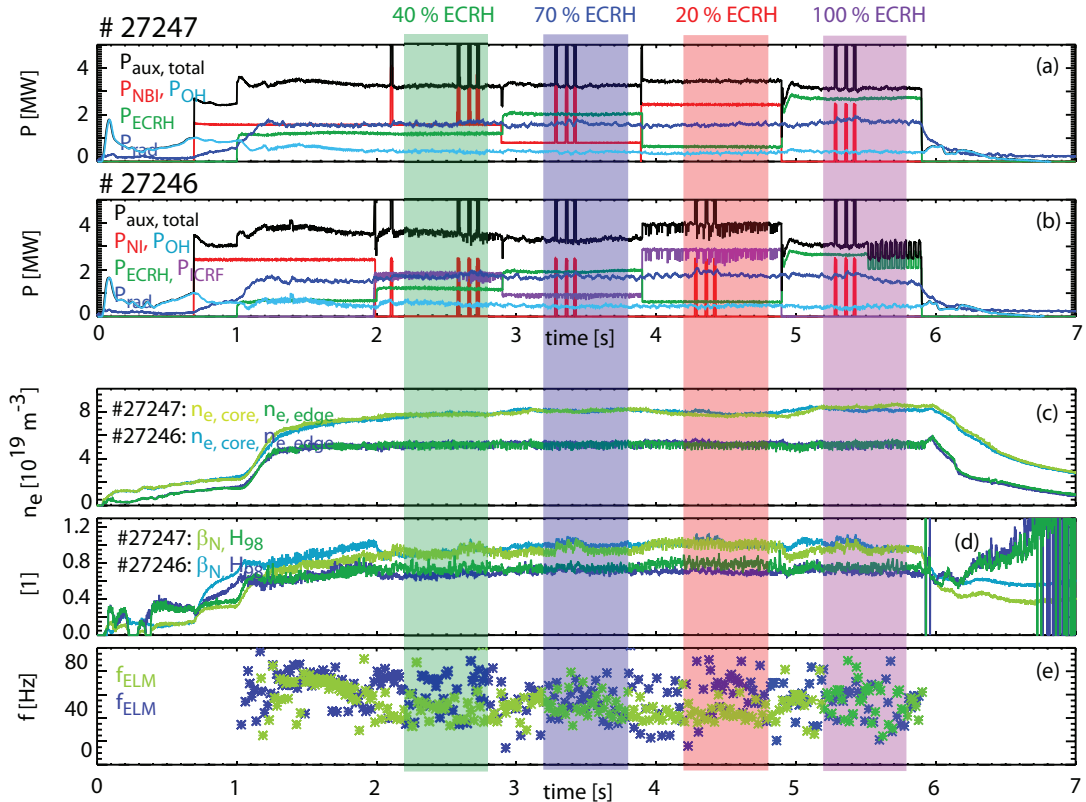


**Figure 5.6:** Comparison of NBI/ECRH (# 27247) and ICRH/ECRH (# 27246) discharge: Plot (a,b): total auxiliary (black), NBI (red), ICRH (purple), central ECRH (green), Ohmic (light blue) and radiated (blue) power of each discharge; in the following plots green corresponds to the NBI/ECRH and blue to the ICRH/ECRH discharge; plot (c): line averaged density in the core (light) and at the edge (dark); plot (d): normalised beta (light) and confinement factor (dark); plot (e): ELM frequency.

In addition to the exchange of NBI by ECRH power discharges were conducted in which ICRH was used instead of NBI and stepwise exchanged by ECRH. One disadvantage of exchanging NBI heating by ECRH is that not only the heating mix is varied but also the torque input and thus the rotation of the plasma is modified to a great extent. This rotation, its shear and thus the  $E \times B$  velocity shear are thought to be some of the key players in the reduction of turbulent transport. By shearing microturbulences and ripping them apart their radial extent is reduced and they are stabilised. The modelling presented in chapter 6.1.5 will also investigate the impact of the  $E \times B$  shear rotation on the kinetic profiles. In chapter 6.3 the experimentally observed stabilising effect will be compared quantitatively with the growth rates of microturbulences calculations. Also the comparison of partially ICRH with partially NBI heated discharges contributes to the analysis of the impact of the rotation on the shape of the kinetic profiles. The major difference between these heating methods is a modified torque input and thus a modified rotation.

The most relevant time traces of discharge # 27246 are shown in figure 5.6 (b) together with the according time traces from the low power NBI discharge # 27247 discussed at the beginning of this chapter (plot(a)). The key difference between both discharges is the replacement of NBI by ICRH. The power fractions between the mixed electron and ion heating systems (NBI or ICRH) and the only electron heating system (ECRH) were kept constant. In the ICRH + ECRH discharge the ECRH was mainly deposited in the centre at  $\rho_{tor} = 0.15$ . In the ECRH only phase the deposition location of roughly 40 % of the ECRH power is around mid radius ( $\rho_{tor} = 0.45$ ) due to a misunderstanding in programming the control system. This change however seems to have only a minor influence on the global plasma parameters and kinetic profiles as comparison to the ECRH only phase in # 27247 shows. The total heating power was kept around 3.6 MW, slightly above the value of discharge # 27247. Due to the common challenges to couple ICRH power into the plasma it is more difficult to keep the total power deposited in the plasma constant over the entire discharge. The plasma radiation in the ICRH case is larger by 100 kW ( $P_{rad} = 1.7$  MW) which can be explained by an increased tungsten concentration of 30 % compared to discharge # 27247.

The line averaged electron densities  $n_e$  of the ICRH (blue) and the NBI (green) heated discharge are compared in plot (c). The light colours depict the core and the dark colours the edge values. The edge values are exactly the same whereas the core values are slightly modified in the two extreme cases of dominant NBI/ICRH and ECRH only. The ICRH dominated case has a slightly higher density. This difference in the ECRH only phase can be explained by the more central deposition in discharge # 27247 and the following larger particle pinch. The  $\beta_N$  values are shown in plot (d) in light colours, the confinement factors  $H_{98}$  in dark colours. Again blue stands for the ICRH and green for the NBI discharge. All time traces are rather constant throughout the discharges and similar in both cases. Both values are slightly higher in the NBI dominated phases compared to the ICRH dominated case which results from a larger  $W_{MHD}$ . In discharge # 27247 the scatter of the ELM frequency is larger than in the ICRH discharge but the mean value is almost the same (plot (e)). The sawtooth frequency shows the same values and behaviour in both discharges with a large scatter around 60 Hz and a rather constant value of 30 Hz in the

ECRH dominated phase.

### 5.3 Profile behaviour including power balance analysis

In this chapter the influence on the kinetic profiles caused by the change of heating mix from dominant ion heating to dominant electron heating is presented. First a short explanation of the fitting procedure is given which was applied to all of the profiles. Afterwards the kinetic profiles of the low power discharge # 27247 (see figure 5.4) and the high power discharge # 28116 (see figure 5.5) will be analysed directly and by means of power balance analysis. In the final part the profiles of a NBI heated discharge (# 27247) are compared to the profiles from an ICRH discharge (# 27246).

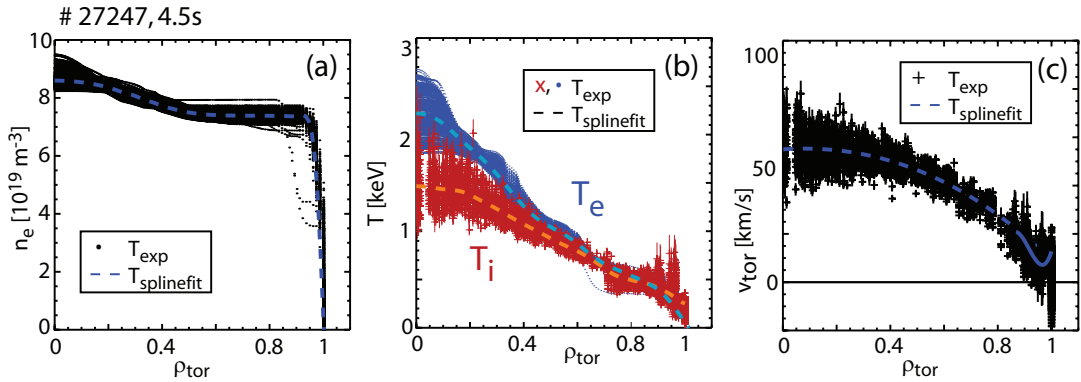


**Figure 5.7:** Exemplary profiles of  $n_e$ ,  $T_e$ ,  $T_i$  and  $v_{tor}$  taken during a 0.6 s time window of one heating phase. All available data are shown together with the resulting spline fits. Especially for the temperatures the variation of the signals in the core is visible due to strong sawtooth oscillations.

For each phase in which the time traces of heating, control and performance parameters are constant all data in a time window of around 0.5 to 0.7 s were used for the analysis. This approach was taken to smooth out disturbances produced by sawtooth and ELM crashes hence allowing the comparison of the profiles of the different heating compositions with each other. The time windows were chosen in such a way that all plasma parameters have at least 3 confinement times to find an equilibrated state after the change of heating mix. All available data of the kinetic profiles for these time windows were fitted with a spline interpolation. For the edge profiles the data during ELMs were excluded from the analysis and only measurements between 5 ms after an ELM up to 2 ms before the next ELM were taken into account. The original data and the fits for the electron density, the electron and ion temperatures and the plasma rotation can be seen in figure 5.7 for a 0.6 s time window. The strong variation of the signals in the centre due to sawtooth oscillations is evident especially for the temperatures. For a better comparison of the different heating phases a reduction of the sawtooth influence on the kinetic profiles

would have been desirable. As outlined in chapter 1.3 this is not possible. To provide compatibility of the data the spline fit approach presented in this paragraph was taken.

The long measurement period leads to relatively small statistical variations. The standard deviations of the electron density lies around 2 to 5 %, of the electron temperature around 3 to 6 %, of the ion temperature around 3 to 10 % and of the toroidal velocity around 3 to 10 km/s. In phases with beam blips for CXRS measurements, it lies between 5 to 15 %. The low values correspond in each case to the standard deviation around mid radius, the high values to the core, where the signal strength is lower and at the edge, where small absolute deviations lead to large total errors and ELMs affect the profiles. The influence of ELMs can be reduced by discarding the ELM crash phases from the analysis, but cannot be excluded entirely due to their strong impact on the edge.

The electron temperature and density were taken from the IDA diagnostic which utilises the DCN interferometer and the Lithium beam diagnostic for the electron density and the ECE spectroscopy for the electron temperature (see chapter 4.5). The ion temperature and the toroidal and poloidal velocities are taken from the various charge exchange spectroscopy diagnostics (see chapter 4.3).

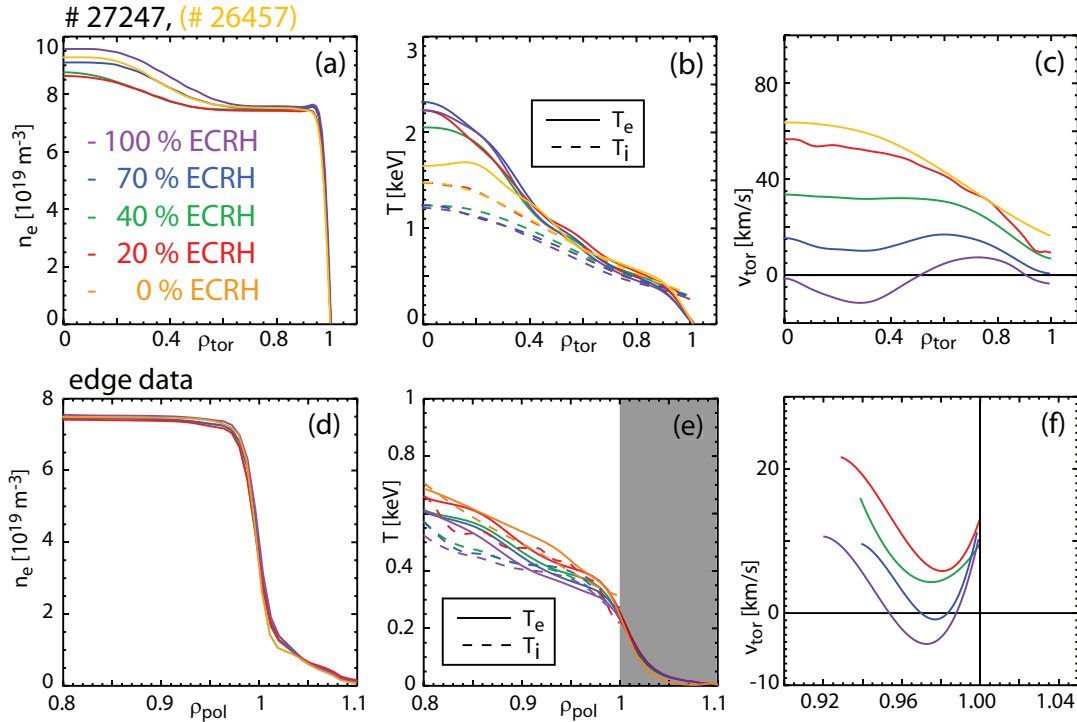


**Figure 5.8:** Averaged kinetic profiles of low power, high collisionality discharge # 27247 during different heating phases. Plot (a): electron density; plot (b): electron (solid) and ion (dashed) temperatures; plot (c): toroidal rotation. Orange traces of NBI only heating are taken from discharge # 26457. Plot (d,e,f): edge data in  $\rho_{pol}$ .

The kinetic profiles of the low power, high collisionality discharge # 27247 are shown in figure 5.8. The top row shows the profiles of the electron density (plot (a)), the electron and ion temperature (plot (b)) and the toroidal plasma rotation (plot (c)) for the entire



### 5.3. PROFILE BEHAVIOUR INCLUDING POWER BALANCE ANALYSIS

---

plasma. The second row shows the corresponding quantities enlarged for the edge region. This discharge covers the cases of 20 %, 40 %, 70 % and 100 % of ECRH. Additionally the NBI only case is taken from discharge # 26457 which was conducted in the same way (same  $I_p$ ,  $B_t$ ,  $n_e$ , plasma shape). No operational differences were observed which explain the differences in the resulting kinetic profiles. However, due to possibly changed machine conditions and the increasing impurity accumulation in NBI only heated plasmas the data of this period have to be evaluated with caution.

The electron density profiles show the effect of increased peaking with increased electron heating fraction very pronounced. The difference between the edge values outside of  $\rho_{tor} = 0.8$  is smaller than the line width, so that not all profiles can be seen in plot (d). This shows their perfect accordance. The central part of the density profile exhibits an increase with increasing fraction of ECRH power which leads to an increased average density. This reflects the typical observation of increased density peaking with increasing ECRH power in this high density, high collisionality regime at ASDEX Upgrade and is reported in detail in [112, 113]: The density peaking shows a maximum at collisionalities around 0.05. This point also coincides with the transition from TEM dominated to ITG dominated microinstabilities. The density peaking declines towards lower and higher values of  $v^*$ . Since the increase of ECRH induces a decrease of the collisionality the density peaking is increased with ECRH fraction when the collisionality is larger than 0.05. This is the case in this discharge.

The electron and ion temperatures are shown as solid and dashed curves in figure 5.8 (b). A jump of  $T_e$  by 20 % is evident from the plot when going from pure NBI to 20 % of ECRH. This change could also be attributed to the changed machine conditions or an increased impurity content of the plasma since this phase is taken from discharge # 26457. Further increase of the electron heating fraction to 100 % increases the electron temperature in the centre by another 10 % which however lies within the variation of the data by sawtooth oscillations. At high ECRH fractions no variation of the electron temperature can be measured. The ion temperature decreases by 15 % when applying at least 40 % of the total power by ECRH. This effect also saturates and the ion temperature profile stays constant even as the ECRH fraction is increased to 100 %. The gradual decline of the electron temperature inside the pedestal top of around 10 % when going from NBI only to ECRH only heating is shown in figure 5.8 (e). This change is only barely outside the scatter of the measured data at the edge. As presented in chapter 4.1 the identification of the electron temperature with the radiation temperature measured by ECE is no longer justified outside of the pedestal ( $\rho_{pol} > 1$ ) due to steep gradients and the low optical depth of the SOL plasma. Therefore no conclusion of the behaviour of the electron temperature in this region can be drawn (grey shaded area in plot (e)). The variation of the ion temperature at the edge lies well within the scatter of the original data and does not allow a conclusion on possible variations with changing heating mix. The decreasing fraction of NBI heating results in a reduced torque input by the neutral beams. This leads to the observed strong decrease of the toroidal rotation  $v_{tor}$  in the entire plasma (plot (c)). The toroidal rotation  $v_{tor}$  at the edge shows the same behaviour namely a decrease with reduced NBI heating fraction (plot (f)). However, the shape of  $v_{tor}$  at the edge is inde-

pendent of the heating mix. The local minimum of the toroidal rotation and the inversion of the rotation shear around 1 cm inside the separatrix is typically observed in H-mode plasmas at ASDEX Upgrade and described in [114]. The remaining rotation in the ECRH only case represents the intrinsic plasma rotation without external torque input. It is governed by residual stress [97, 113]. The poloidal rotation  $v_{pol}$  at the edge has small values and does not show any variation with changing the heating mix outside the uncertainties of the measurement (not shown). In chapter 5.4 the edge rotation will be used to calculate the radial electric field at the edge for different heating mixes.

The experimental kinetic profiles were used to perform a power balance analysis of the different phases in the discharge with the computer programme ASTRA (see chapter 2.4). ASTRA solves the 1D radial transport equations. The heat exchange between electrons and ions and the heat fluxes and heat diffusivities of the electron and ion channel were investigated. Several sensitivity studies were performed to evaluate the influence of errors in the measurement of the electron and ion temperature (see chapter 5.3.1) and the plasma radiation (see chapter 5.3.2) on the results of the power balance analysis. The analysis is performed for each heating phase separately. The provided profiles are averaged over the periods of constant experimental data and the code was run long enough to achieve convergence to equilibrated values of the calculated quantities.

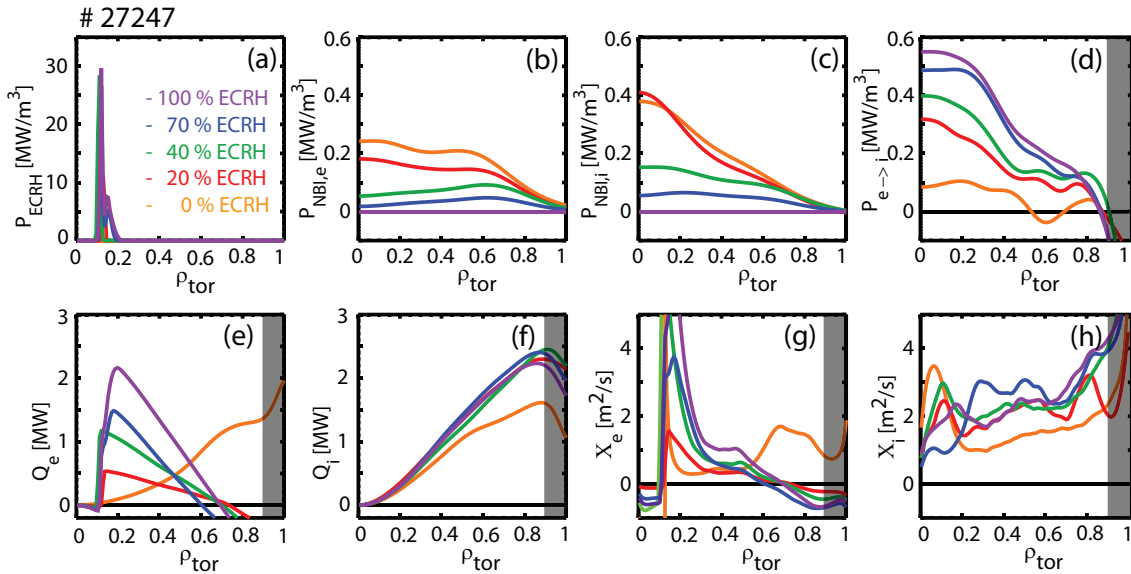


**Figure 5.9:** Power balance analysis of all heating mixes from 0 % to 100 % ECRH power for the low power, high collisionality discharge # 27247. Heating power of ECRH  $P_{ECRH}$  (plot (a)), NBI deposited to electrons  $P_{NBI,e}$  (plot (b)) and to ions  $P_{NBI,i}$  (plot (c)), energy exchange from electrons to ions due to Coulomb collisions  $P_{e \rightarrow i}$  (plot (d)), heat flux in electron  $Q_e$  (plot (e)) and ion  $Q_i$  (plot (f)) channel and heat diffusivities of electrons  $\chi_e$  (plot (g)) and ions  $\chi_i$  (plot (h)). Orange traces of 0 % ECRH power are taken from discharge # 26457.

The power balance analysis is performed for all phases of the high collisionality discharge # 27247 to compare the different heating mixes. Alike to the analysis of the kinetic

### 5.3. PROFILE BEHAVIOUR INCLUDING POWER BALANCE ANALYSIS

profiles the data of the NBI only phase is taken from discharge # 26457. The results of the power balance analysis are shown in figure 5.9. The radial power distribution of all Gyrotrons is summed up to one profile resulting in the total ECRH power  $P_{ECRH}$  deposited to the electrons shown in plot (a). The narrow and central deposition can be seen for all cases. The powers of the NBI heating deposited to electrons  $P_{NBI,e}$  and to ions  $P_{NBI,i}$  are shown in plot (b) and (c). The integrated NBI powers going to electrons and ions are similar for each heating phase. However, their radial distribution differs due to different absorption cross sections of electrons and ions (see chapter 3.1).

A strong increase of the heat exchange term due to Coulomb collisions  $P_{e \rightarrow i}$  with growing ECRH power can be seen in plot (d). This is due to the increasing difference between electron and ion temperature which is the main drive of this exchange term. The grey shaded area has to be excluded from the analysis since the radial grid of ASTRA cannot resolve the high gradients at the edge caused by the H-mode pedestal. The heat flux of the electrons is shown in plot (e). For this high collisionality discharge the increase of  $P_{e \rightarrow i}$  with increasing ECRH power leads to a complete energy transfer from electrons to ions towards the edge, so that the heat flux of the electrons approaches zero. In the very edge it reaches even negative values. These negative values are most likely non-physical. This topic will be treated in detail below in chapter 5.3.1 and 5.3.2 while discussing the sensitivity of the power balance analysis on input data. Furthermore the energy transfer from electrons to ions leads to an invariance of the ion heat flux  $Q_i$  (plot (f)) with the power deposition to electrons or ions.

The electron heat diffusivity  $\chi_e$  is shown in plot (g). Around mid radius it increases with increasing electron heating from low values of around 0.3 m<sup>2</sup>/s to around 1.2 m<sup>2</sup>/s.  $\chi_e$  exhibits a strong peak around  $\rho_{tor} = 0.2$  and is increasing with ECRH power. This can be partly explained by the local power deposition without a visible  $T_e$  increase. However, the extreme local deposition of the ECRH power corresponds in most cases to only 3 radial grid points in which the power drops to 1/e of its peak value at the maximum possible radial resolution of ASTRA. For that reason a correct calculation of the diffusivity cannot be expected due to numerical limitations. The ion heat diffusivity  $\chi_i$  which is at least a factor of 2 higher than the electron heat diffusivity is shown in plot (h). It shows a tendency towards higher values with increasing electron heating going from around 1.5 m<sup>2</sup>/s to 2.5 m<sup>2</sup>/s at mid radius. The overall increase of both heat diffusivities is consistent with a slight decrease of discharge performance with increasing ECRH power.

The same analysis presented in this chapter so far was also done for the high power, low collisionality discharge # 28116. The corresponding kinetic profiles can be seen in figure 5.10. The electron density profile (plot (a)) shows a strong peaking but no variation with changing heating mix when increasing the ECRH fraction from 15 % to 45 %. The slight rise at mid radius with ECRH fraction lies well within the scatter of the data. This different response to increased ECRH compared to the high collisionality case is in line with previous observations, in which the density peaking shows a maximum in this collisionality range of  $\nu^* \approx 0.06$  and does not change with a variation of  $\nu^*$  [112, 113]. The experimental observations are compared with TGLF and GS2 calculation in chapter 6.1 and 6.3.



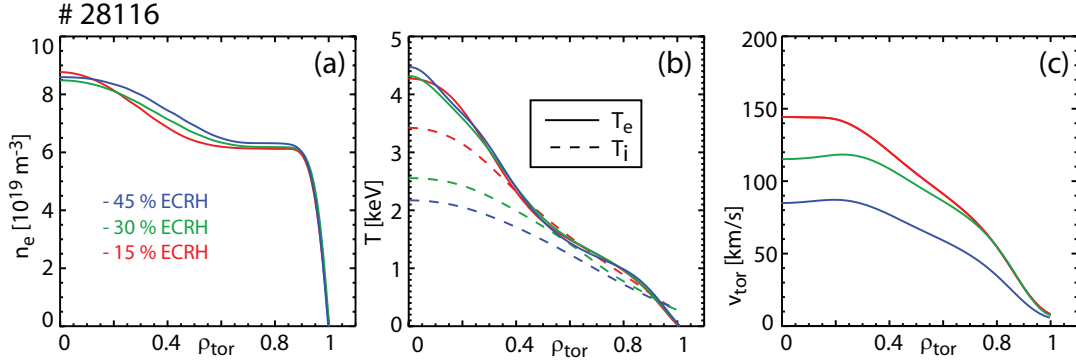


**Figure 5.10:** Averaged kinetic profiles of high power, low collisionality discharge # 28116 during different heating phases: plot (a): electron density; plot (b): electron (solid) and ion (dashed) temperature; plot (c): toroidal rotation.

The electron temperature does not show a variation with varying heating mix (straight lines in plot (b)). The ion temperature shows a strong reduction by 40 % over the entire plasma radius when going from low to high ECRH fractions. This effect of diminished ion temperature is more pronounced than in the low power discharges. It can be understood considering the lower heat exchange from electrons to ions due to lower collisionality.

The toroidal rotation shows the same behaviour as in the low power discharges namely a reduction with decreasing torque input by NBI beams. The overall values are larger due to larger absolute beam power levels. Since the variation of torque input is smaller in this discharge compared to the previously analysed ones also the variation of the rotation is smaller. The rotation velocity/MW beam power fits very well with the values of the low power discharge. The central value of the case with the lowest NBI power of 4 MW of this discharge lies around 90 km/s which is slightly above the value of the highest NBI power contribution of discharge # 27247 with 3.3 MW NBI power. This discharge had a central toroidal velocity of 70 km/s. The central toroidal rotation scales roughly linear with the input beam power respectively with the beam torque input. This holds for the entire database of all performed discharges as one can follow up in chapter 5.5. Neither the edge profiles of the toroidal rotation nor of the poloidal rotation show any variation with changing heating mix.

Also for this high power, low collisionality discharge the power balance analysis was performed. The results are shown in figure 5.11. The ECRH power is deposited even more localised in the centre of the plasma (plot (a)) compared to the high collisionality discharge. The NBI power to electrons and ions is shown in plot (b) and (c). The increased ion heating by NBI compared to the low power discharge is caused by the increased electron temperature of the plasma. The underlying effects are described in chapter 3.1. Because of the reduced collisionality the energy exchange term due to Coulomb collisions  $P_{e \rightarrow i}$  is reduced by a factor of two while the heat fluxes are increased by about a factor of two compared to the low power discharge. This happens despite the increased heating power and larger difference between electron and ion temperature. The variation of  $P_{e \rightarrow i}$  with changing heating mix results in an invariant heat flux in the electron channel  $Q_e$

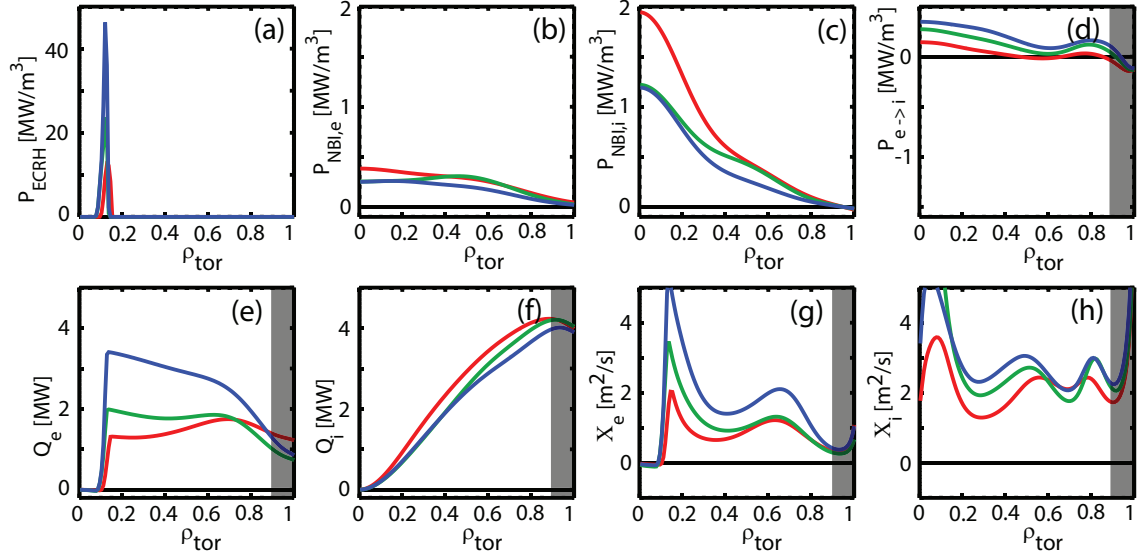


**Figure 5.11:** Power balance analysis of the different heating mixes going from 0 % to 45 % ECRH power for the high power, low collisionality discharge # 28116. Heating power of ECRH  $P_{ECRH}$  (plot (a)), NBI going to electrons  $P_{NBI,e}$  (plot (b)) and to ions  $P_{NBI,i}$  (plot (c)). Energy exchange due to Coulomb collisions  $P_{e \rightarrow i}$  (plot (d)). Heat flux in electron  $Q_e$  (plot (e)) and ion  $Q_i$  (plot (f)) channel. Heat diffusivities of electrons  $\chi_e$  (plot (g)) and ions  $\chi_i$  (plot (h)).

towards the edge for all considered heating mixes (plot (e)) as in the low power discharge. However, the smaller exchange terms does not lead to a complete transfer of the heat from the electron to the ion channel as in the high collisionality regime. A finite value of  $Q_e$  remains at the edge. The heat flux in the ion channel which is unchanged by the heating mix as in the discharge analysed before is shown in plot (f). The electron heat diffusivity shows the same behaviour as in the low power discharge, namely a large peak at the position of the ECRH absorption and an increase with ECRH power (plot (g)). The absolute values are higher compared to the previous case and range from 1 m<sup>2</sup>/s to 2 m<sup>2</sup>/s at mid radius. The ion heat diffusivity (plot (h)) has a value of around 2.5 m<sup>2</sup>/s with a slight tendency towards higher values with increased ECRH fraction. However, this variation lies well within the uncertainties of the measurement and the computation.

Concluding the power balance analysis we observe an important impact of the energy exchange term due to Coulomb collisions. Its increase with ECRH fraction due to a larger  $T_e/T_i$  leads to an ion heat flux, which is independent of the heating mix. For high collisionalities it transfers all energy from the electron to the ion channel towards the edge. However, for lower  $\nu^*$  its influence is reduced and a finite electron heat flux remains. Outside the deposition region of the ECRH power, the ion diffusivity is the dominant contribution to radial heat transport.

The comparison of the time traces from the NBI/ECRH and ICRH/ECRH heated discharges # 27247 and # 27246 did not show any significant differences. In addition the kinetic profiles of the two discharges are compared for the case with 40 % ECRH and

60 % of NBI or ICRH in plot 5.12. No difference of the electron density (plot (a)) can

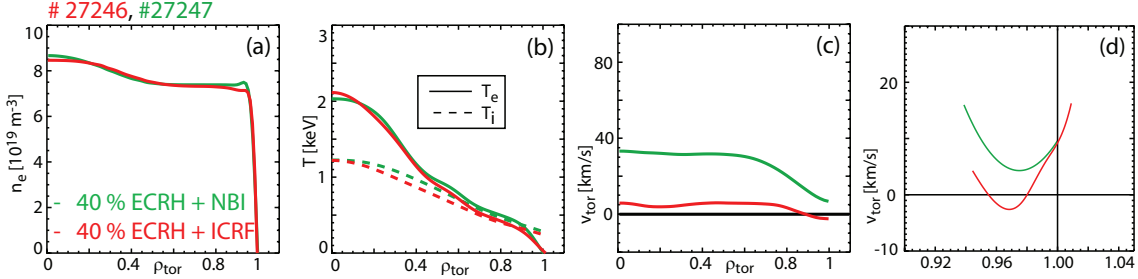


**Figure 5.12:** Averaged kinetic profiles of the NBI/ECRH discharge # 27247 (green) in comparison with the ICRH/ECRH discharge # 27246 (red) for the 40 % ECRH fraction case: plot (a): electron density; plot (b): electron (solid) and ion (dashed) temperature; plot (c,d): toroidal rotation in the core and at the edge.

be seen in the core and at the edge. While the edge values of the electron and ion temperatures (plot (b)) are lower by 20 % in the ICRH discharge, this discrepancy is compensated towards the core, where no difference can be seen between the two discharges. The toroidal rotation in the centre and at the edge is diminished to low intrinsic values in the ICRH case. This is expected due to missing torque input by the lack of NBI power. The poloidal rotation has low values and does not show any difference between the two cases. The replacement of ICRH by ECRH power shows the same behaviour as replacing NBI by ECRH power in discharge # 27247, namely an increased peaking of the electron density, an increase of the central electron temperature and a decrease of the central ion temperature. Also the edge values are unchanged with varying heating mix. In contrast to the NBI/ECRH discharge the toroidal rotation in the centre and at the edge has very low values and is independent of the heating mix. This is expected due to the absence of a change of torque input. Concluding the changed rotation which is the main difference between the NBI and ICRH heated discharges does not have an affect on the stability of the electron density and temperatures profiles in this high collisionality regime.

### 5.3.1 Sensitivity of the power balance analysis to temperatures

In the last chapter it was shown that the prominent influence of the difference between electron and ion temperature and the energy exchange term due to Coulomb collisions  $P_{e \rightarrow i}$  on the power balance analysis is very important. For that reason a sensitivity study of the influence of the input temperatures on the power balance analysis was performed for the low power, high collisionality discharge # 27247 and for the high power, low collisionality discharge # 28116. The electron and ion temperatures were increased and decreased independently by 10 % and 20 %. The temperatures for the TRANSP calculations are not changed, so the deposition profiles of the NBI to electrons and ions are the same. The increase of the electron temperature for the power balance by a factor of 1.1 and 1.2 has almost the same effect as a decrease of the ion temperature by a factor of 0.9

### 5.3. PROFILE BEHAVIOUR INCLUDING POWER BALANCE ANALYSIS

and 0.8 respectively. Viceversa a decrease of the electron temperature by a factor of 0.9 and 0.8 has the same effect as an increase of the ion temperature by a factor of 1.1 and 1.2 respectively. Accordingly the relevant parameter is  $T_e/T_i$ . Only the cases varying the electron temperature are considered in the following.

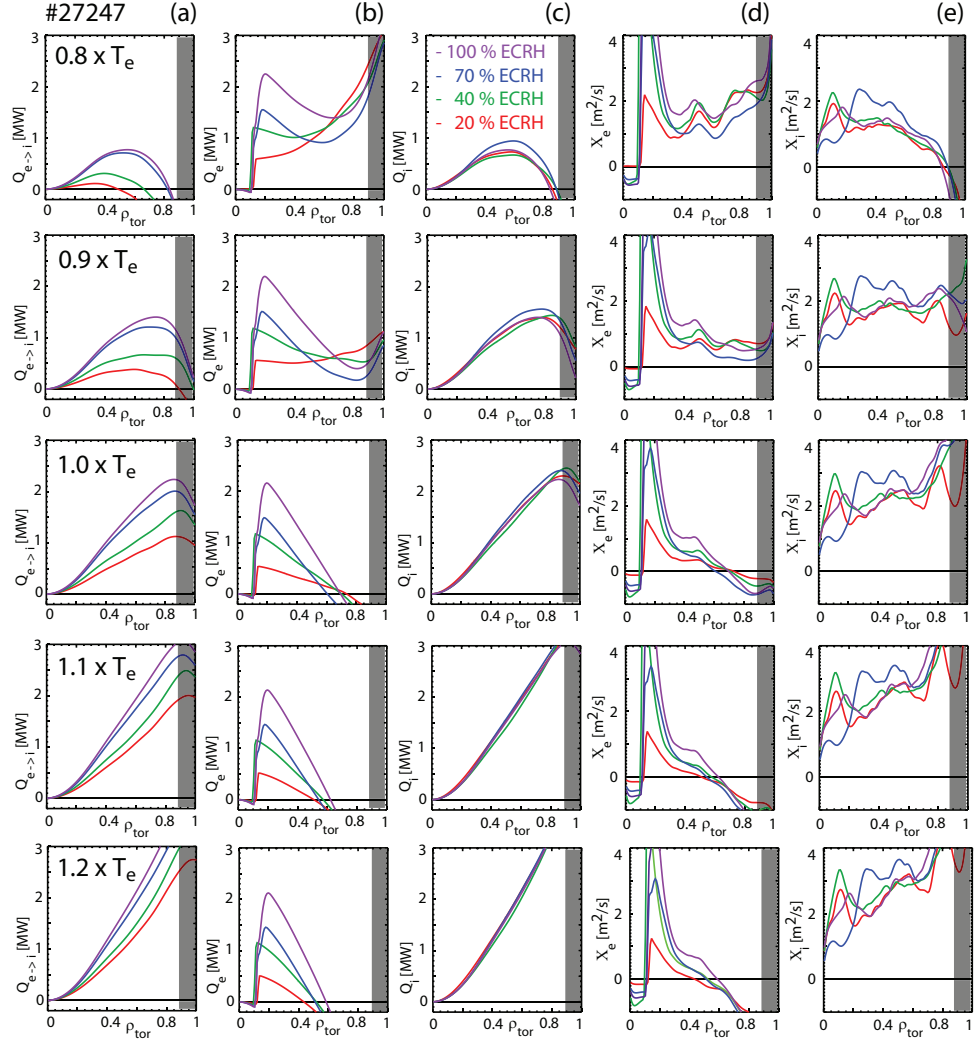


**Figure 5.13:** Sensitivity study of the power balance to  $T_e$  for the low power, high collisionality discharge # 27247. Energy heat exchange due to Coulomb collisions  $P_{e \rightarrow i}$  (plot (a)), heat flux in electron  $Q_e$  (plot (b)) and ion  $Q_i$  (plot (c)) channel and heat diffusivities of electrons  $\chi_e$  (plot (d)) and ions  $\chi_i$  (plot (e)).

The energy exchange term by Coulomb collisions  $P_{e \rightarrow i}$  (column (a)), the electron (column (b)) and ion (column (c)) heat flux and the electron (column (d)) and ion (column (e)) heat diffusivities are shown in figure 5.13. Considered are the cases  $0.8 \times T_e$ ,  $0.9 \times T_e$ ,  $1.1 \times T_e$  and  $1.2 \times T_e$  from top to bottom and the case with original  $T_e$  as comparison in the middle. All four heating mixes considered in the analysis so far are shown in each plot in the previously used colours. The most important change in the analysis is the increase of the heat exchange term by Coulomb collisions due to a larger difference between electron and ion temperature when increasing the electron temperature. Columns (b) and (c) show

a strong variation of the heat transported in the electron and ion channel dependent on the temperature difference. However, for each case the amount of heat in the electron channel at the edge and in the ion channel over the entire radius is independent of the heating mix. The analysis of the spline fitted experimental data in chapter 5.3 showed that non-physical negative heat fluxes occur at the edge in the electron channel. This would imply an inward pinch of heat against the temperature gradients. Several publications report on observations of a heat pinch in experiment e.g. with strong off-axis electron heating or observations of heat pulse propagation by modulated ECRH [115]. However, no negative steady state electron heat flux is observed. In addition under normal discharge conditions the size of the heat pinch is within the uncertainties of the measurement. This is in accordance with theory which predicts a relatively small heat pinch as an off-diagonal contribution to the heat flux [116]. However, it does not predict an overall negative value of the heat flux in the presence of a regular temperature gradient. We believe that the negative heat flux observed in the power balance analysis of the high collisionality discharge is not the proof of a heat pinch, but a consequence of imperfect temperature measurements. The experimental observations show a small, but finite difference of electron and ion temperature in the outer half of the plasma. A small change of either of the temperatures affects the heat exchange term significantly. A systematic decrease of the electron temperature or an increase of the ion temperature by around 5 % is enough to avoid the negative heat fluxes due to a reduced heat exchange term. These modifications of the data lie well within the errors of the ECE (see chapter 4.1) and the CXRS measurements (see chapter 4.3) of 10 % to 15 %, respectively 3 % to 10 %.

The ion heat diffusivity increases by roughly 10 % per 10 %  $T_e$  decrease. In absolute values the electron heat diffusivity experiences a similar decrease with  $T_e$  as  $\chi_i$  experiences an increase. However, due to small original values of the electron heat flux especially towards the edge, the relative change is quite significant and can reach negative values up to mid radius for higher electron temperatures. The equations of the diffusivities do not contain terms for the heat pinch which is believed to be not relevant for the analysed discharges as described in the last paragraph. Therefore the negative values are attributed to the apparent negative heat flux in the electron channel. We conclude, that the general observations during the power balance analysis are quite robust when a large variation of one of the temperatures by 20 % is applied. The heat flux in the ion channel is independent of the heating mix as is the edge heat flux of the electrons. A variation of still 10 % leads to minor modifications of the absolute values but the findings of the power balance are not affected. The heat flux in the electron channel approaches zero towards the edge and the ion heat diffusivity plays the dominant role in the major part of the plasma. Only around the localised deposition location of the ECRH power the electron heat transport is dominant as expected.

The same variation of the electron temperature profiles was also performed for the high power, low collisionality discharge # 28116. The same tendencies can be also observed in this discharge, shown in figure 5.14. With increasing electron temperature and the resulting increase of the difference between electron and ion temperature the heat exchange term due to Coulomb collisions increases. As a result the edge electron heat flux

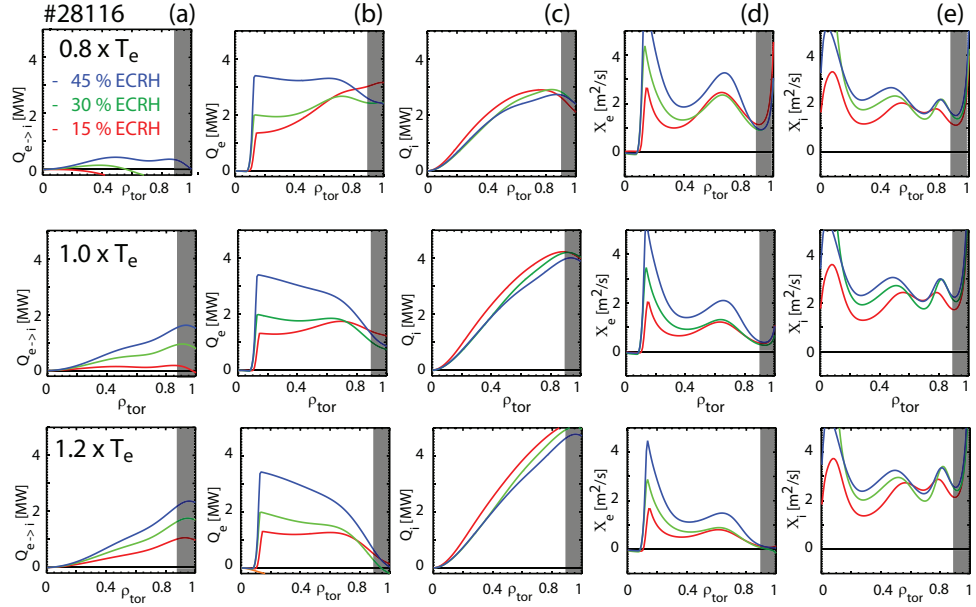


**Figure 5.14:** Sensitivity study of the power balance to  $T_e$  for the high power, low collisionality discharge # 28116. Energy heat exchange due to Coulomb collisions  $P_{e \rightarrow i}$  (plot (a)), heat flux in electron  $Q_e$  (plot (b)) and ion  $Q_i$  (plot (c)) channel and heat diffusivities of electrons  $\chi_e$  (plot (d)) and ions  $\chi_i$  (plot (e)).

approaches zero at the edge for the case of 20 %  $T_e$  increase while the ion heat flux is increased by roughly 1 MW at the edge (column (b) and (c)). The heat diffusivity of the electrons is reduced by  $0.7 \text{ m}^2/\text{s}$  while the ion heat diffusivity is basically unchanged. Decreasing the electron temperature results in the contrary effects. In the case of a 20 % reduction of  $T_e$  the heat exchange term due to Coulomb collisions becomes negative for all cases except the dominant ECRH period (column (a)).  $Q_e$  rises,  $Q_i$  decreases,  $\chi_e$  increases and  $\chi_i$  decreases with decreasing  $T_e$  (column (d) and (e)). The heat exchange term due to Coulomb collisions does play a lesser role in this low collisionality discharge compared to the heating terms. Accordingly the impact of a large change of one temperature by 20 % does also have a smaller impact on the power balance analysis. We conclude that in these discharges the power balance analysis is very robust with regard to a temperature variation.

### 5.3.2 Sensitivity of the power balance analysis to plasma radiation

In addition to the sensitivity of the power balance analysis to the ratio of electron and ion temperature, the influence of a variation of the radiated power was performed. Since the main contributor to the radiated power is the Bremsstrahlung in the analysed cases  $P_{rad}$  is subtracted from the electron power. Accordingly its variation only effects the electron channel in the power balance analysis. The results of the power balance analysis are shown in figure 5.15 for discharge # 27247. The two cases with a reduction and an



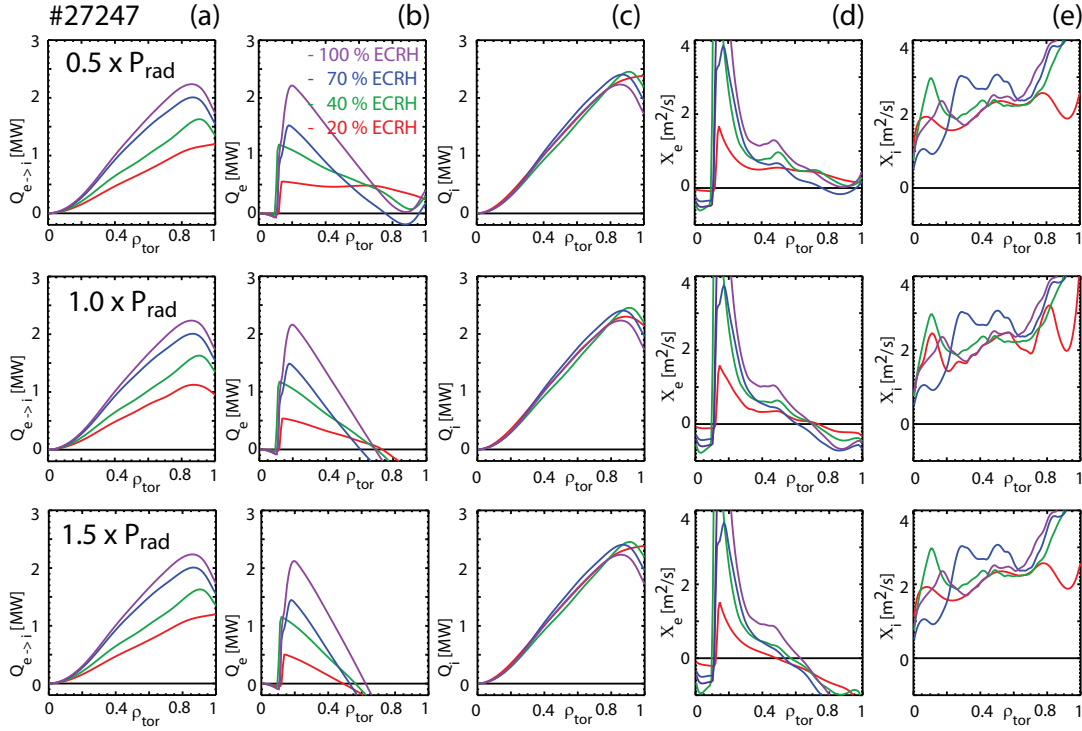


**Figure 5.15:** Sensitivity study of the power balance to  $P_{rad}$  for low power, high collisionality discharge # 27247. Energy heat exchange due to Coulomb collisions  $P_{e \rightarrow i}$  (plot (a)), heat flux in electron  $Q_e$  (plot (b)) and ion  $Q_i$  (plot (c)) channel and heat diffusivities of electrons  $\chi_e$  (plot (d)) and ions  $\chi_i$  (plot (e)).

increase of the radiated power by 50 % are analysed. The reduction removes the non-physical occurrence of a negative heat flux in the electrons channel. In this case the heat flux at the edge approaches zero for all heating mixes. This would solve the issue of negative heat fluxes in the electron channel. Since the maximum error of the plasma radiation can be estimated to 30 % a reduction of the radiation by that value cannot resolve the negative heat fluxes alone. However, the last chapter showed that a variation of the temperatures by about 5 % and hence well inside the error of the measurement can rise the electron heat flux above zero for the entire plasma. A combined effect of radiation over prediction and imperfect temperature measurements is most likely. As consequence from the rise of the electron heat flux above zero the electron heat diffusivity stays also above zero and increases by about  $0.3 \text{ m}^2/\text{s}$  at mid radius. Increasing the plasma radiation by 50 % leads to the opposite effect. The heat flux in the electron channel is reduced and the electron heat diffusivity is decreased to negative values even further inside around  $\rho_{tor} = 0.6$ .

The influence of a 50 % increase of the plasma radiation on the electron quantities ( $Q_e$ ,  $\chi_e$ ) is largely comparable with the influence of an electron temperature decrease by 5 %. The case with  $1.5 \times P_{rad}$  is almost identical with the case of a 10 % increase of the  $T_e$  (see chapter 5.3.1). However, the modification of the radiated power does not influence the heat exchange term and the ion heat fluxes and diffusivities  $Q_{e \rightarrow i}$ ,  $Q_i$ , and  $\chi_i$ .

A sensitivity study for the power balance was also performed for the low collisionality discharge # 28116. It shows the same dependencies. Reducing the radiated power by 50 % increases the heat flux and the heat diffusivity in the electron channel towards the edge while both quantities of the ion channel remain unchanged. Increasing the radiation by 50 % reduces the edge electron heat flux to zero towards the edge and decreases the electron diffusivity at mid radius by  $\approx 0.4 \text{ m}^2/\text{s}$ .

Also in this low collisionality discharge the reduction of the radiated power has a similar influence on the electron quantities as an increase of the electron temperature. However, in this low collisionality discharge the impact on the power balance analysis is smaller from the heat exchange term and larger from the radiated power term. Accordingly the impact of a change of the radiated power corresponds to the impact of a larger temperature modification compared to the high collisionality discharge. A decrease of the radiation by 50 % has a similar impact on the electron heat flux and diffusivity as a reduction of the electron temperature by 5-10 %. The increase of the radiated power by 50 % leads to a similar heat flux in the electron channel as the increase of the electron temperature by 10 %. However, the absolute changes by these temperature variations are small. We note that the ion related quantities are not affected at all.

## 5.4 Radial electric field

This chapter reports on the analysis of the radial electric field conducted for one exemplary discharge (# 27946) which features a very good quality of the data from the edge CXRS measurements. Experimental observations show clear evidence that inside transport barriers a strong radial variation of the radial electric field  $E_r$  occurs [117]. This is true not only for internal but also for edge transport barriers like the H-mode pedestal. The associated shear of the  $E \times B$  velocity is thought to be one of the key players in suppressing turbulent transport and thus enabling the large gradients in these regions. The proposed mechanism for reduced turbulent transport is a diminishing radial extension of temperature and density fluctuations which is consistent with non-linear simulations of turbulent transport and qualitatively found in experiment [6]. Additionally classical and neoclassical transport is lowered by the so called 'orbit squeezing' which reduces the orbit width and thus diminishes the radial transport [6].

Prior to this study the hypothesis was raised that the change in edge rotation by reducing the NBI heating would also reduce the electric field and thus would degrade the H-mode pedestal leading to an undesired reduction of the performance of the discharge. This effect would be disastrous for future devices in which the rotation will be greatly lessened compared to the situation nowadays due to reduction of the torque input compared to an increase of the inertia of the plasma. The analysis of the radial electric field presented in this chapter will investigate this hypothesis.

According to the force balance all ion species have to follow the influence of the electric



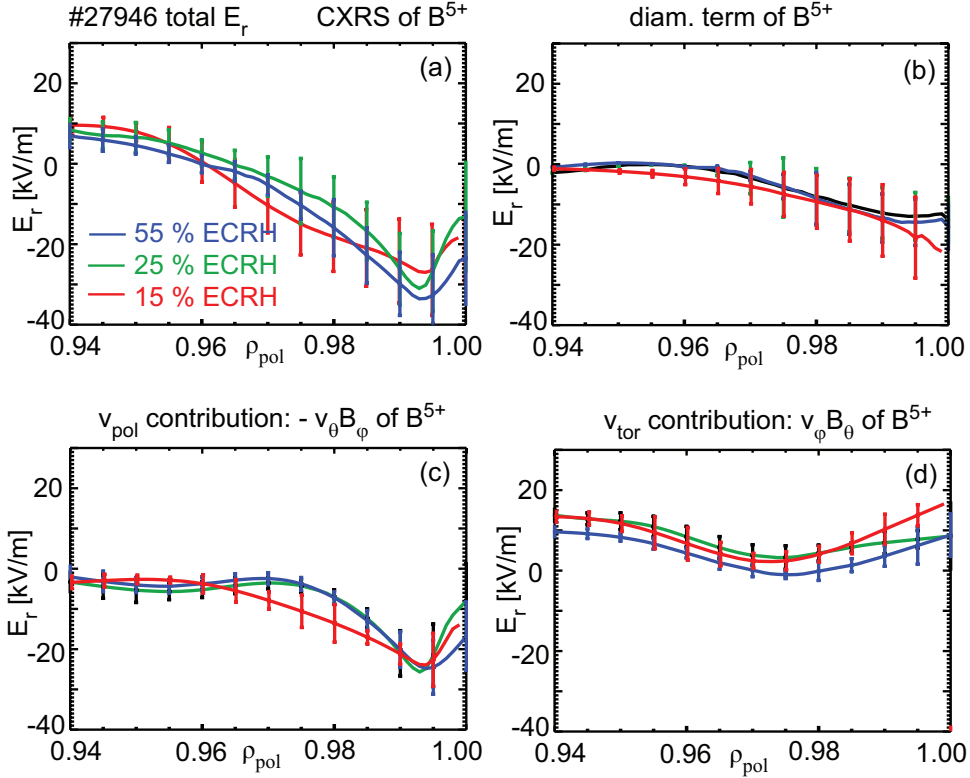


**Figure 5.16:** Plot (a): radial electric field  $E_r$  measured by the CXRS system on  $B^{5+}$  for the medium power discharge # 27946 with  $P_{aux, total} = 5.5$  MW. Also shown are the three contributions of the radial force balance: plot (b): diamagnetic term due to pressure gradient; plot (c): term due to poloidal rotation; plot (c): term due to toroidal rotation. The analysis for 15 % (green), 25 % (black) and 55 % (red) of ECRH is shown.

field identically. Therefore the electric field can be detected by its effect on impurities [118]. The densities, temperatures and velocities of several impurities can be measured precisely by the CXRS system. All ions have to fulfill the radial force balance:

$$-\nabla p_i + e \cdot n_i \cdot Z_i (\vec{E} + \vec{v} \times \vec{B}) = 0 \quad (5.2)$$

For the radial component this can be written as:

$$E_r = \frac{1}{e \cdot n_i \cdot Z_i} \frac{\partial p_i}{\partial r} - v_{\theta,i} \cdot B_\phi + v_{\phi,i} \cdot B_\theta \quad (5.3)$$

As described in [97] the edge CXRS system measures the profiles of the density  $n_i$ , temperature  $T_i$  and rotation velocities in toroidal  $v_{\theta,i}$  and poloidal  $v_{\phi,i}$  direction for a specific impurity species. Typically the measurements of boron  $B^{5+}$  are used for the analysis. The radial resolution of the diagnostic is increased by radial sweeps of the plasma. This allows the determination of the pressure gradient  $\partial p_i / \partial r$  of the impurity species with an

accuracy enabling the evaluation of the local radial electric field. The short measurement periods during beam blips in the low power and ICRH discharges do not allow the analysis of the radial electric field. In these cases not enough radial points are available and the uncertainties are too large caused by the non stationary neutral beam.

The electric field  $E_r$  at the edge for the medium power discharge # 27946 with a total heating power of 5.5 MW is shown in figure 5.16. The analysis was done for ECRH fractions of 15 %, (corresponding to 60 % of electron heating: red), 25 % (60 % electron heating: green) and 55 % (75 % electron heating: blue). The total radial electric field which exhibits the typically observed strong dip shortly inside the separatrix in the steep gradient zone is shown in plot (a) [117]. The location of the error bars do not correspond to individual measurements but indicate a confidence band of the analysis. The measurement volumes overlap each other caused by a sweep of the plasma edge and the high time resolution of the diagnostics. Within these error bars the radial electric fields of the three different heating mixes overlap and do not show a variation with changing heating mix. The other three plots show the three contributions to the electric field:

1. The diamagnetic term:  $\frac{1}{n_i \cdot Z_i \cdot e} \frac{\partial p_i}{\partial r}$
2. The term due to poloidal rotation:  $-\mathbf{v}_{\theta,i} \cdot \mathbf{B}_{\phi}$
3. The term due to toroidal rotation:  $\mathbf{v}_{\phi,i} \cdot \mathbf{B}_{\theta}$

The diamagnetic term does not show any difference with varied heating mix. The contribution due to poloidal rotation which is the main contributor to the radial electric field in the transport barrier for impurity ions has a lower value for the phase with 15 % ECRH around  $\rho_{tor} = 0.98$ . However, the signal to noise ratio (SNR) of this phase is smaller which leads to larger error bars, so that this trend is not significant. The contribution due to toroidal rotation shows a little decrease with increasing ECRH fraction which is barely outside the error bars. However, the variation of the rotation of these cases is not very pronounced and could be larger for high collisionality discharges. Due to experimental constraints mentioned before the electric field could not be analysed for these low power discharges. The heat flux through the separatrix in the ion and electron channel is hardly modified by the variation of the heating mix (see chapter 5.3). Therefore no statement can be made how the variation of this heat flux influences the electric field. In these experiments the major effect of the change from NBI to ECRH is a reduction of the torque and the fast ion losses at the plasma edge which are both proportional to the NBI power. We conclude that both parameters do not affect  $E_r$  in the steep gradient zone within the error bars of the measurement. These results are very much in line with the analysis of  $E_r$  for H-modes under various conditions presented in [117] which shows that  $E_r$  fits generally well to the diamagnetic term of the main ions as expected to zeroth order from neoclassical theory. Accordingly the radial electric field is produced almost entirely by the main ions, which are typically deuterium for ASDEX Upgrade discharges. In other words the rotation of the main ions is found to be a minor contribution to the experimentally observed electric field  $E_r$  at the edge and the hypothesis of a degradation of the edge by a reduction of the rotation due to changing heating mix can not be confirmed.

The analysis of the pedestal and the SOL behaviour was limited in this work to the direct observations of the kinetic profiles presented in chapter 5.3 and the calculations of the radial electric field presented in this chapter. Since the main focuss of this work lies at the understanding of the core transport and its modelling by existing first principle codes, some further observations concerning the outer part of the plasma are presented in the outlook in chapter 8.

## 5.5 Correlations and dependencies

So far the analysis of the experiments has been concentrated mainly on two selected cases which are diagnosed very well and exhibit a large variation of collisionalities. With respect to the comparison of NBI to ICRH heating and the analysis of the electric field two other discharges were shown in the course of this thesis. Altogether a total of 36 discharges were conducted spanning a wide parameter space which can be found in table 5.1. All discharges were conducted in a similar way keeping the total heating power constant while varying the contributions of NBI, ICRH and ECRH to the total heating power. All control parameters like magnetic equilibrium or gas puff were kept as constant as possible during one discharge and were only changed from discharge to discharge. From all constant phases of all discharges a database of a multitude of control parameters and plasma measurements was built in order to find global correlations and dependencies between the various quantities. In the following some of these correlations are presented. The profile data are taken from mid radius at  $\rho_{tor} = 0.5$  outside of the sawtooth mixing radius. The data are averaged over  $\Delta\rho_{tor} = 0.05$  if not stated otherwise. In chapter 6.2 we come back to the database and compare a subset of the experimental data with modelling results of the kinetic profiles.

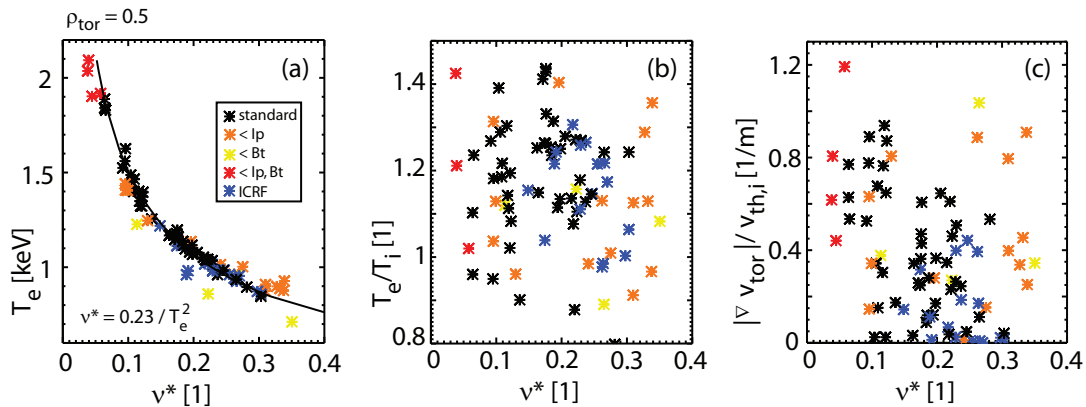


**Figure 5.17:** Correlations between the collisionality and  $T_e$  (plot (a)),  $T_e/T_i$  (plot (b)) and  $|\nabla v_{tor}|/v_{th,i}$  (plot (c)) at  $\rho_{tor} = 0.5$  using mixtures of NBI, ECRH and ICRH (blue). Black and blue symbols:  $q_{95} = 4.0$ ,  $I_p = 1$  MA, red symbols:  $q_{95} = 4.0$ ,  $I_p = 0.75$  MA, yellow symbols:  $q_{95} = 3.0$ ,  $I_p = 1$  MA, orange symbols:  $q_{95} = 5.3$ ,  $I_p = 0.75$  MA.

In figure 5.17 some correlations with the collisionality  $\nu^*$  are shown. In plot (a) the collisionality dependence on the electron temperature is shown. It can be fitted very good with the formula  $\nu^* = k_1/T_e^2$  with  $k_1 = 0.22$ . The experimental data shows almost perfect agreement with this function. This is expected since  $n_e$  is proportional to  $I_p$  at constant magnetic field and hence  $n_e \cdot q$  is constant in the formula for  $\nu^*$  (see chapter 2.2). The ratio  $T_e/T_i$  and  $|\nabla v_{tor}|/v_{th,i}$  do not correlate with  $\nu^*$  caused by a variation of the heating mix and total power. Plot (b) and (c) show the achieved variation of these quantities They were chosen due to their impact on the stability of microturbulences such as ITG, ETG and TEMs as presented in chapter 2.3.

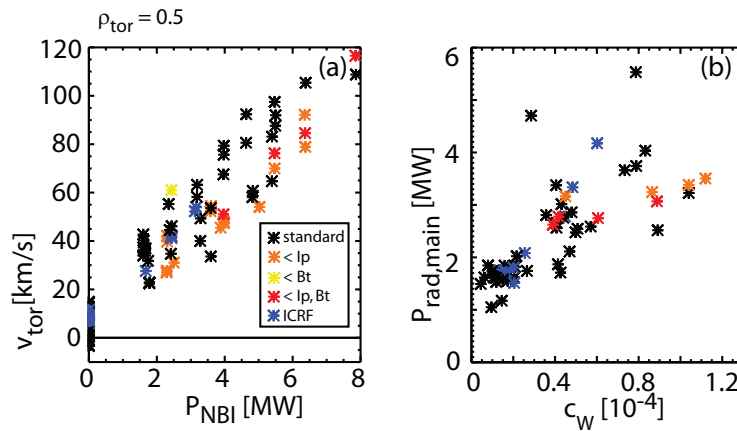


**Figure 5.18:** Plot (a): correlation between the NBI power and the toroidal rotation. Plot (b): correlation between the tungsten concentration of the plasma at temperatures of 1 to 1.5 keV and the radiated power. The data has the same colour coding as in figure 5.17.

In chapter 5.2 it was mentioned that the toroidal rotation scales roughly linear with the input beam power respectively with the beam torque input. This dependence can be seen in figure 5.18 (a) exemplary for a radius of  $\rho_{tor}=0.5$ , albeit it can be found for all radii.

The dependence of the radiated power  $P_{rad,main}$  on the tungsten concentration can be seen in plot 5.18 (b). Only the radiation emitted from the main chamber is taken into account since the divertor radiation is influenced by many factors. The light emitted from the transition from  $W^{21+}$  to  $W^{35+}$  is taken to determine the tungsten concentration  $c_W$ . This transition occurs in a temperature range of 1 to 1.5 keV, localising the measurement typically around mid radius. Only those cases are shown, for which the tungsten concentration was measured. The plasma radiation shows a level of around 1 MW also with negligible tungsten concentration mainly due to hydrogen radiation. The total radiation rises roughly linear with increasing  $c_W$  and shows a growing scatter. This scatter is likely produced by varying concentrations of other impurities.

Since the dominance of the ion heat transport from power balance (see chapter 5.3) points towards ITG dominated plasmas, on one hand the inverse gradient length of  $T_i$  is expected to decrease with  $T_e/T_i$  (see chapter 2.3 for description of ITG. On the other hand, it is expected to depend on the toroidal velocity which acts destabilising on the ITG by the

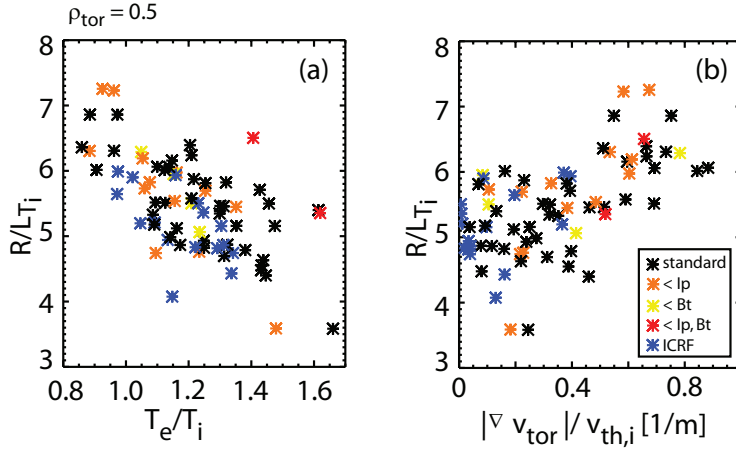


**Figure 5.19:** Dependence of  $RL_{T_i}$  on  $T_e/T_i$  and  $|\nabla v_{tor}|/v_{th,i}$ . Gradients are taken from spline-fitted data. The data has the same colour coding as figure 5.17.

parallel velocity shear  $\nabla v_{\parallel}$  and stabilising by the  $E \times B$  shear. For that reason the influence of  $T_e/T_i$  and  $|\nabla v_{tor}|/v_{th,i}$  on  $RL_{T_i}$  is shown in figure 5.19. The shown data is averaged over  $\Delta\rho_{tor} = 0.2$  to reduce the statistical error in the evaluation of the gradients. The expected trend is indeed found in plot (a) which shows a decrease of  $RL_{T_i}$  with an increase of the fraction of the electron and ion temperatures. For  $|\nabla v_{tor}|/v_{th,i} < 0.4$  no significant effect of the rotational shear on  $RL_{T_i}$  is visible. This is in line with the experimental observations that no degradation of the performance of the discharges is evident when switching from NBI to ICRH heating. Since the ICRH power is limited to  $P_{ICRH} < 3$  MW, the exchange of ICRH by ECRH power could only be analysed at low powers, respectively low rotations and normalised rotation gradients in the NBI discharges. Above  $|\nabla v_{tor}|/v_{th,i} = 0.4$  a stabilising effect can be seen resulting in an increase of the inverse gradient length. These data link to an older study on the branch  $0.7 \leq T_e/T_i \leq 1.05$  at AUG still with the uncoated C-tiles as plasma facing components allowing significantly lower densities [27]. Therein a combined effect of  $T_e/T_i$  and  $R\nabla v_{tor}/v_{th,i}$  (range: 0.8-1.5) could be identified describing the  $RL_{T_i}$  quantitatively well stressing the importance of  $E \times B$ -shear stabilisation of the ITG. Both dependencies of the entire database indicate the role of the ITG as dominant microinstability.

# Chapter 6

## Modelling results

This chapter reports about the analysis and modelling of the discharges presented in the last chapter by several codes. The trapped gyro-Landau fluid transport model TGLF (see chapter 2.5) was used within ASTRA (see chapter 2.4) to model the electron and ion temperature alone and together with the electron density. Sensitivity studies were performed by varying both temperature profiles as starting and boundary condition. Additionally the influence of  $P_{rad}$  on the modelling was analysed. In the second part linear gyrokinetic simulations are presented. They were performed with the code GS2 (see chapter 2.6) to identify the dominant microinstability responsible for radial heat transport.

### 6.1 Modelling of kinetic profiles

The electron and ion temperature and the electron density profiles presented in the last chapter were modelled with the trapped gyro-Landau fluid transport code TGLF (see chapter 2.5) to check how far existing first principle codes can predict plasma performance. It is a first principle based model and is embedded in the ASTRA package. In the following the results are presented and compared to the experimental data to verify the accuracy of the modelling.

The modelling of the profiles uses the same inputs as the power balance analysis. For the quantities that are modelled ( $T_e$ ,  $T_i$  and  $n_e$ ) the experimental profiles are used as starting conditions. The experimental values of  $T_e$ ,  $T_i$  and  $n_e$  at the pedestal top ( $\rho_{tor} = 0.85$ ) are taken as boundary condition. So far no code is available in the framework of ASTRA, which can model the H-mode pedestal including its transport barrier with high gradients. The toroidal rotation is prescribed from experimental measurements and is thus not modelled.

### 6.1.1 Treatment of sawtooth oscillations

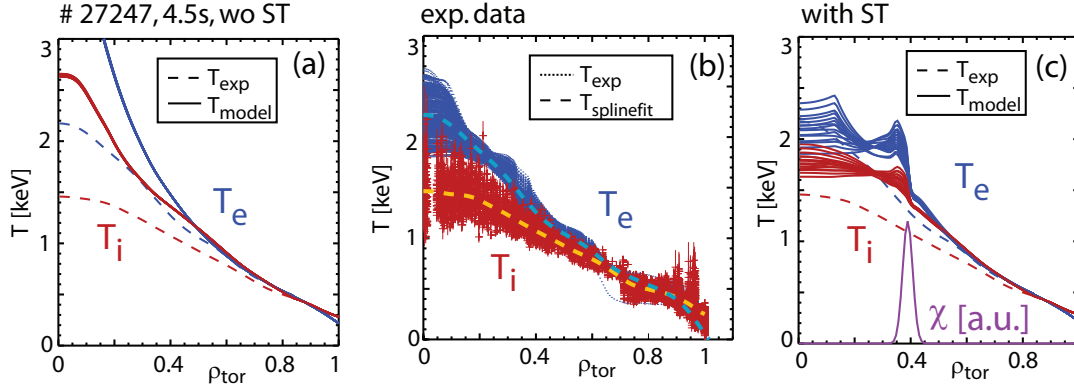


**Figure 6.1:** Influence of sawtooth oscillations on the modelling of  $T_e$  and  $T_i$ . The dashed curves show the averaged experimental profiles, while the solid curves show the modelled data ( $T_e$ : solid,  $T_i$ : dashed). Plot (a): modelling without implementation of a sawtooth model for one of the considered cases. Plot (b): experimental variation of the inner part of the profiles by sawtooth oscillations. Plot (c): modelled temperatures with variation by the sawtooth model.

The first modelling attempts showed a strong peaking and an overestimation of the central electron and ion temperatures inside  $\rho_{tor} = 0.5$  by a factor of 1.5 compared to the experimental profiles (see figure 6.1). However, the scatter of the experimental profile data shows a strong sawtooth oscillation especially in the core (plot (b)) which is by default not considered in the modelling. For that reason a Kadomtsev-Porcelli model treating the sawtooth crashes had to be applied. It was only fitted to the experimental sawtooth period leaving the radial extent and the amplitude of the sawtooth crash as free parameters (see chapter 2.4). In plot (c) several time points of the modelling during one sawtooth cycle are shown as different profiles for the electron and ion temperatures shown in red and blue. The application of the sawtooth model introduces a strong perturbation and variation of the temperature profiles in the centre of the plasma which is consistent with the experimental observations. However, the rather crude coupling of TGLF and the sawtooth model introduces non-physical peaks in the temperatures around  $\rho_{tor} = 0.35$  and very large temperature gradients at  $\rho_{tor} = 0.4$ . Only for the low collisionality discharges with long sawtooth periods they are smoothed out by diffusive effects before the next sawtooth crash again builds up the gradients. For the high collisionality discharge the high gradients are not yet dissipated before the next sawtooth crash. This behaviour is not observed in experiment. For that reason an additional artificial Gaussian term is added to both calculated diffusivities of the electrons and of the ions, which is added in plot (c). The diffusivities normally comprise two terms: An turbulent contribution from the TGLF calculations and a neoclassical contribution from the subroutine NCLASS<sup>1</sup> [119, 120]. The Gaussian has a width of 4 % of the minor radius, is located symmetrically around the mixing radius and is introduced only for 30 ms after every sawtooth crash. Applying this measure the disturbing effect of the sawtooth model on the TGLF calculations are

<sup>1</sup>NEOCL4 in ASTRA



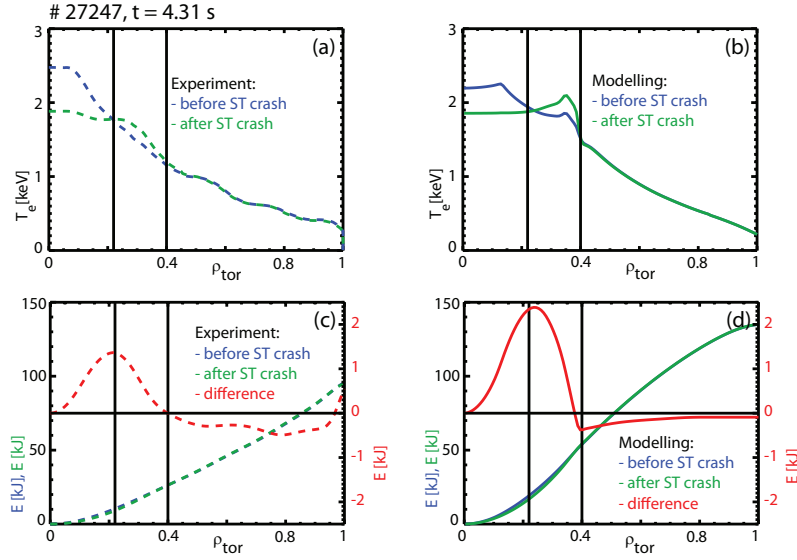


**Figure 6.2:** Influence of a sawtooth crash on the experimental and modelled  $T_e$  profile. Plot (a): experimental  $T_e$  profiles before (blue) and after (green) sawtooth crash. Plot (b): modelled  $T_e$  profiles. Plot (c,d): corresponding kinetic energy content and energy difference between the cases.

minimised and the experimental observations are reproduced. The described approach is applied with the same set of parameters for all modelled cases presented in the following. The influence of the modelled sawtooth crashes on the electron density is less severe. This can be explained by the typical flatness of the profiles in the centre of the plasma.

The sawtooth model is verified by direct comparison of one modelled sawtooth cycle with the experimental data of the electron temperature. Its high temporal resolution and small scatter allows this single profile comparison. The experimental electron temperature profiles just before a sawtooth crash (blue) and just after a crash (green) are shown in figure 6.2 (a). The comparison with the modelled profiles, presented in plot (b), shows a similar behaviour. Both the inversion radius at  $\rho_{tor} = 0.2$  and the mixing radius at  $\rho_{tor} = 0.4$  are reproduced very well by the model (both values are not specified beforehand to the model). The kinetic energy content of the plasma for the electrons is shown in plot (c) for both cases before (blue) and after (green) the sawtooth crash. The difference between these two is drawn in red. It shows an expelled energy by the sawtooth of 1.4 kJ. This rather small value compares to an energy content of the entire plasma of  $\approx 350$  kJ and results from the small volume in the core region of the plasma. Nevertheless, the central electron temperature experiences a drop of 25 %. The same comparison of the energy content of the plasma is shown in plot (d) for the modelled cases. Both the experimental and the modelled data show a good energy conservation by the sawtooth crash, since the difference between the energies is close to zero outside the mixing radius. However, the amount of expelled energy is higher in the modelled case by about 70 % due to a less peaked temperature profile and higher temperature values outside  $\rho_{tor} = 0.1$ . For better comparison, only the averaged experimental profiles are shown in the following, while the modelling results are shown for several time points during one entire sawtooth cycle.



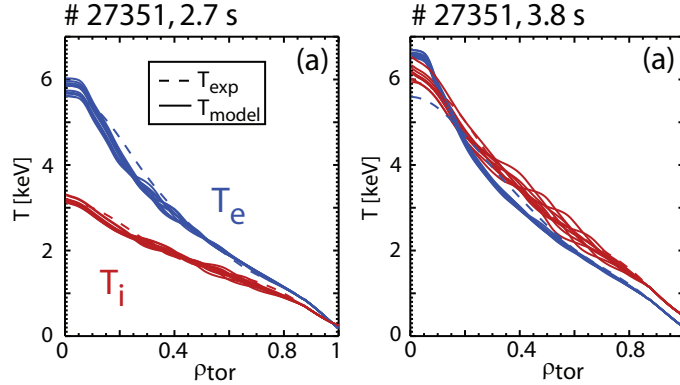


**Figure 6.3:** Verification of the TGLF modelling for two phases of discharge # 27351 without sawtooth activity. Plot (a): 3.2 MW ECRH and 5 MW NBI power. The dashed curves show the averaged experimental profiles, while the solid curves show the modelled data ( $T_e$ : blue,  $T_i$ : red). Plot (b): 5 MW additional NBI power.

In addition an H-mode with broad central counter ECCD (# 27351) was modelled which had sawtooth free phases. The TGLF modelling could be tested without the disturbing treatment of sawtooth crashes by switching off the relevant module. The experimental electron and ion temperature profiles can be seen in figure 6.3 as dashed lines together with the modelled profiles as solid lines. A phase at 2.7 s with 3.2 MW of ECRH and 5 MW of NBI heating is shown in plot (a). A later phase around 3.8 s, in which an additional 5 MW of NBI power was added is shown in plot (b). The temperature profiles including the strong peaking of  $T_e$  are reproduced very accurately for both cases. In the second phase, the additional NBI power leads to a significant increase of the ion temperature, while the electron temperature does not show any change. The resulting reduction of  $T_e/T_i$  is reproduced very good.

In case of sawtooth free discharges the modelling by TGLF reproduces the temperature profiles quite well. In case of sawtooth activity in the experiment an additional routine was employed taking into account the effects of sawtooth crashes also in the modelling. This leads to a good reproducibility of the experimental kinetic profiles.

### 6.1.2 Modelling of electron and ion temperatures

This chapter presents the modelling of the electron and ion temperatures and compares the different heating mixes. The temperature only modelling is presented separately from the combined temperature and density modelling since early modelling attempts did not reproduce the density profiles satisfactory and showed large discrepancies between the temperature profiles of both cases. First the results of the low power, high collisionality discharge # 27247 are presented. The averaged experimental profiles of the temperatures are shown in figure 6.4 (dashed) together with the corresponding modelled profiles (solid) for all four heating mixes with increasing ECRH fraction from (a) to (d). For all cases

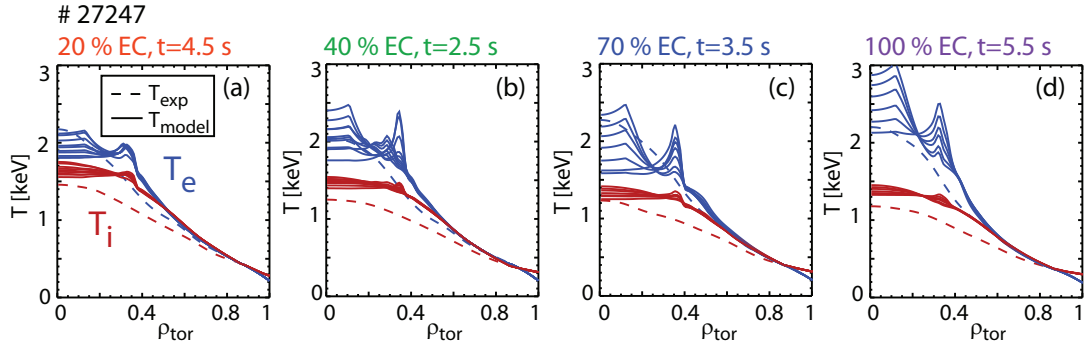


**Figure 6.4:** Plot (a) to (d): comparison of the  $T_e$  (blue) and  $T_i$  (red) modelling by TGLF with the experimental profiles with increasing ECRH fraction of the low power, high collisionality discharge # 27247. Time averaged experimental profiles are shown as dashed lines, modelled profiles as solid lines.

the sawtooth crashes are reproduced very well. The radial extent, the temperature drop and the energy expulsion agrees well with the experiment. The shape of the experimental temperature profiles, the magnitude of the electron temperature profile and the increasing fraction  $T_e/T_i$  is reproduced very well by the modelling. Only the ion temperature is in general slightly overestimated, which results from the stronger coupling of electron and ion channel compared to the experimental observations in the outer half of the plasma. This results in equilibrated temperature profiles up to  $\rho_{tor} = 0.5$  and a drag of  $T_i$  to higher values.

The temperature modelling was also performed for the high power, low collisionality discharge # 28116. The comparison of the resulting profiles with the experimental data is shown in figure 6.5 for all heating phases. The shape of the modelled electron and

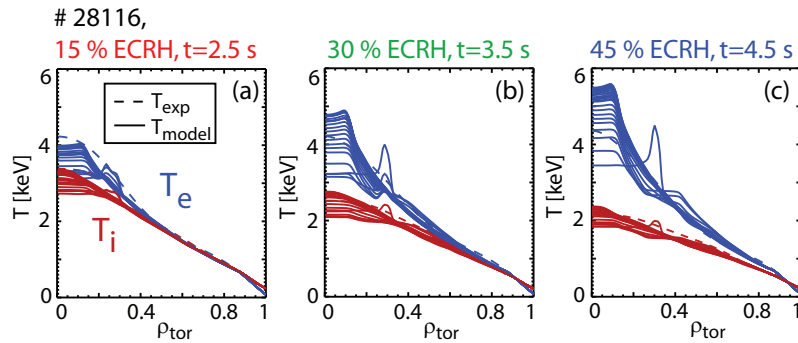


**Figure 6.5:** Plot (a) to (c): comparison of the  $T_e$  (blue) and  $T_i$  (red) modelling by TGLF with the experimental profiles with increasing ECRH fraction of the high power, low collisionality discharge # 28116. Time averaged experimental profiles are shown as dashed lines, modelled profiles as solid lines.

ion temperature profiles, the sawtooth behaviour and the increasing fraction  $T_e/T_i$  with ECRH fraction is reproduced very well. On one side, the latter is generated in the modelling by a decrease of the ion temperature, which is also observed in experiment with the

same magnitude. On the other side, the modelling also shows an increase of the electron temperature with ECRH fraction, which is not observed in the experiment. The experimentally observed low coupling of electron and ion channel in the high ECRH fraction phases, which results in a difference of  $T_e$  and  $T_i$  up to the edge, is reproduced very well.

Summing up, the modelling of the temperature profiles reproduces the experimental observations to a high degree and replicates most of the changes when increasing the ECRH fraction and going from high to low collisionality.

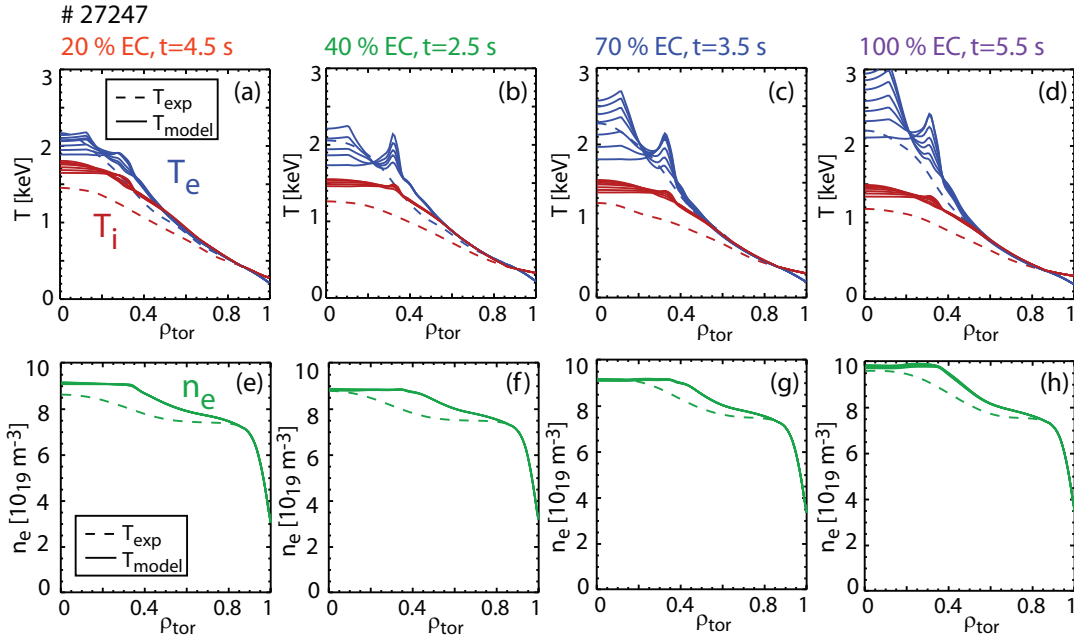


**Figure 6.6:** Plot (a) to (d): comparison of the  $T_e$  (blue) and  $T_i$  (red) modelling by TGLF of the low power, high collisionality discharge # 27247 with the experimental profiles. The time averaged experimental profiles are shown as dashed lines, the modelled profiles as solid lines. Plot (e) to (h): electron density modelling.

The power balance in chapter 5.3 showed, that the ion heat flux  $Q_i$  does not differ with varying heating mix. This is also true for all other analysed discharges. TGLF calculations support that the heat diffusivity of the ions is much larger than the one of the electrons. Therefore the heat is eventually flowing in the ion channel. The reproduction of the experimentally observed behaviour of kinetic profiles and heat fluxes shows the understanding of the underlying mechanisms by theory and the correct implementation in the used codes.

### 6.1.3 Simultaneous temperature and electron density modelling

In addition to the temperature only modelling presented in the last chapter, a simultaneous electron and ion temperature and electron density modelling was performed. Input,

and starting and boundary quantities are the same as described before. The experimental values of the electron density at  $\rho_{tor} = 0.85$  were applied as boundary conditions for the electron density. The particle diffusivity in the transport equation for the electron density consists of a diffusive and a pinch term. The diffusive term comprises an turbulent contribution from TGLF calculations and a neoclassical contribution originating from NCLASS in ASTRA. The pinch term comprises of an turbulent contribution from TGLF calculations and a neoclassical Ware pinch contribution. The resulting temperature and density profiles of the combined modelling are shown in figure 6.6. The electron and ion temperature profiles (plot (a) to (d)) show almost no difference compared to the temperature only modelling presented in the last paragraph. The modelling of the electron density is shown in plot (e) to (h) for the different ECRH fractions. Also in these plots the experimental fitted data are shown as dashed lines, while the several modelled profiles during one sawtooth cycle are shown as solid lines. However, due to flatness of the electron density profile in the core inside the inversion radius of the sawtooth, no variation outside the line thickness can be observed. The peaking of the density profiles and especially the increased peaking with increased ECRH fraction is reproduced.

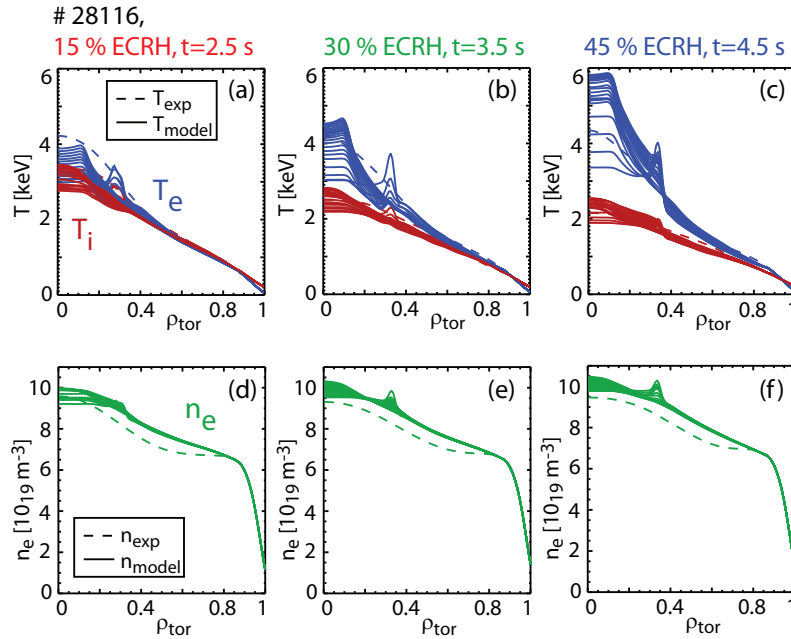


**Figure 6.7:** Plot (a) to (c): comparison of the  $T_e$  (blue) and  $T_i$  (red) modelling by TGLF of the high power, low collisionality discharge # 28116 with the experimental profiles. The time averaged experimental profiles are shown as dashed lines, the modelled profiles as solid lines. Plot (d) to (f): electron temperature modelling.

The combined temperature and density modelling was also performed for the high power, low collisionality discharge # 28116. The results can be seen in figure 6.7. The temperature profiles are the same as in the temperature only modelling (plot (a) to (c)). The modelled electron densities are shown in plot (d) to (f). They show a very good reproduction of the experimental profiles (dashed lines). The experimentally observed large peaking and the invariance of the peaking with ECRH fraction is reproduced. In chapter

6.3 GS2 calculations will analyse the accordance of these findings with linear gyrokinetic theory.

Summing up, the combined electron and ion temperature and electron density modelling shows very good agreement with the experimental observations. While the temperature profiles do not show any difference to the temperature only modelling, the density dependence on collisionality and ECRH fraction is reproduced excellently.

### 6.1.4 Sensitivity of TGLF modelling to starting and boundary conditions

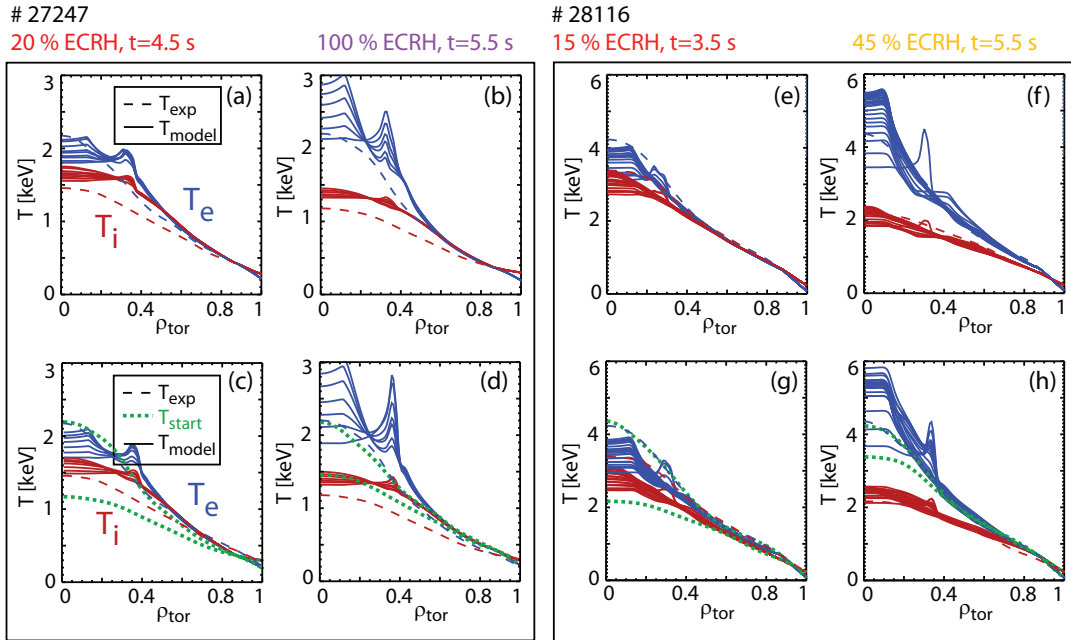


**Figure 6.8:** Sensitivity of TGLF modelling to starting profiles of  $T_e$  and  $T_i$  for the two extreme cases of the low power, high collisionality discharge # 27247 (plot (a) to (d)) and the high power, low collisionality discharge # 28116 (plot (e) to (h)). Plot (a,b, e,f): original modelling (solid lines) as presented in chapter 6.1 in comparison with the experimental data (dashed lines). Plot (c,d, g,h): modelling with exchanged starting conditions (coloured lines) in comparison with the experimental data (dashed lines) and the exchanged starting conditions as green dotted lines.

The sensitivity of the TGLF modelling to a variation of the electron and ion temperatures as input parameters was also analysed during this work. First the results of modifying the starting temperature profiles are presented. For that purpose the two extreme cases of the low power, high collisionality discharge # 27247 were used: the third and last phase with 20 % and 100 % of ECRH fraction. To realise the desired variation, the starting profiles of the two cases were exchanged while all other input data were left unchanged. The resulting modelling can be seen in figure 6.8 as solid lines in comparison with the experimental

data ( $T_e$ : blue,  $T_i$ : red). The modelling with the experimental starting profiles is shown in plot (a) and (b) as presented in chapter 6.1. The modelling with exchanged starting conditions is shown in plot (c) and (d). Together with the modelled data and the experimental profiles the exchanged starting profiles are shown as green dotted lines, which are the experimental profiles of the other case respective. The modelling is not dependent on the starting conditions, but converges also in the case of exchanged starting profiles to the experimentally observed profiles.

The same exchange of starting profiles was also performed for the high power, low collisionality discharge # 28116, which is shown in plot (e) to (h). The starting profiles of the two extreme phases with 15 % and 45 % ECRH power were exchanged. While the original modelling for the two cases is shown in plot (e) and (f), the modelling with exchanged starting temperature profiles is shown in plot (g) and (h). Also in these cases the modelled data is shown as solid lines, the experimental data as dashed lines and the starting profiles as green dotted lines. The modelled profiles with exchanged starting conditions converge to the exact same shape and values independent of the starting profiles of the electron and ion temperature profiles.

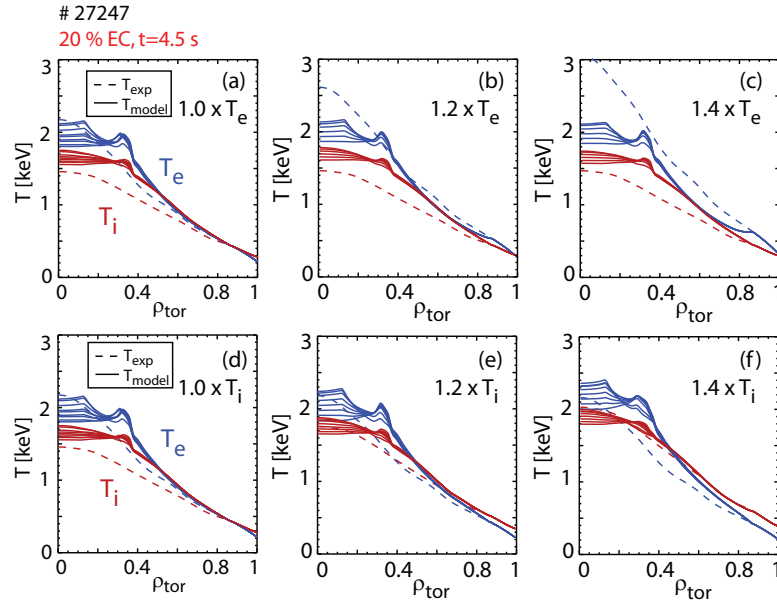


**Figure 6.9:** Sensitivity of TGLF modelling to the boundary values of  $T_e$  and  $T_i$ . Plot (a,d): original modelling (solid lines) as presented in chapter 6.1 for one case of the low power, high collisionality discharge # 27247 with 20 % ECRH in comparison with the experimental data (dashed lines). Plot (b,c): multiplication of the electron temperature by 1.2 and 1.4. Plot (e,f): multiplication of the ion temperature by 1.2 and 1.4.

In addition to the sensitivity study of the modelling to the starting temperature profiles, the sensitivity to the boundary values of  $T_e$  and  $T_i$  at  $\rho_{tor} = 0.85$  was analysed. The analysis presented in the last paragraph showed no sensitivity of the modelling results to the starting conditions. Accordingly the boundary values can be changed by multiplying the whole electron and ion temperature profiles individually by a constant factor (1.2 and 1.4). With these changes the modelling can be performed as usual. The results with changed

boundary conditions are shown in figure 6.9 for one case of the low power, high collisionality discharge # 27247 with 20 % of ECRH in comparison to the original modelling. Again, the experimental profiles are shown as dashed lines and the modelled profiles as solid lines. The first row shows the results of the modelling with increased electron temperature, in plot (b) by multiplication with 1.2 and in plot (c) with 1.4. Due to strong coupling of electron and ion channel in this high collisionality regime, both temperatures are equilibrated close inside the boundary condition ( $\Delta\rho_{tor} = 0.1$  for the multiplication with a factor of 1.4). Since the ion temperature profiles do hardly change with respect to the original case, the influence of the changed boundary conditions is restricted to  $\rho_{tor} > 0.7$ . The temperature values outside the sawtooth oscillation, the central values and the profile variation by sawtooth crashes are similar to the ones with experimental electron temperature boundary values.

The second row shows the modelling results with an increased ion temperature by a factor of 1.2 in plot (e) and 1.4 in plot (f). In the first case, the electron temperature is unchanged compared to the original modelling while the equilibration of the ion temperature is achieved only shortly outside the mixing radius of the sawtooth crashes. In the case of the multiplication by 1.4, the modelled ion temperature profile follows the input profile more closely and the electron temperature rises to higher values around mid radius than in the original modelling. The two temperatures equilibrate only close to the mixing radius of the sawtooth crashes.

The same analysis of independently increased edge values of the electron and ion temperatures of the high power, low collisionality discharge shows a similar behaviour. The increase of the boundary value of the electron temperature increases the ion temperature only slightly. The electron temperature is elevated only in the outer part ( $\rho_{tor} > 0.7$ ) while the inner part is basically unchanged. However, electron and ion channel are decoupled so far, that no equilibration takes place between the two temperatures. Increasing the boundary value of the ion temperature increases the whole ion temperature profile, while the electron temperature profiles increase only slightly.

The concluding observation is, that the modelled ion temperature profile shows a more resilient behaviour than the electron temperature profile on the variation of the boundary temperature values. Considering a critical gradient model in the TGLF calculations this can be explained by the larger stiffness of the ion temperature profile. As a consequence the electron temperature profiles is bent towards the ion temperature profile in both cases of increased and decreased  $T_e/T_i$ . However, the modelling is not sensitive on the starting profiles and the variation of the boundary condition by 20 % only changes the results marginally. Even a large change of the electron and ion temperature by 40 %, which is far outside the error bars of the ECE and CXRS diagnostics, does not change the resulting profiles seriously.



### 6.1.5 Sensitivity of TGLF modelling to $E \times B$ shear

In chapter 5.3 we drew the conclusion that changes in the rotation and thus changes in the  $E \times B$  shear are too small to have a measurable impact on the kinetic profiles. To verify this on a theoretical basis the  $E \times B$  term was switched off in the modelling of the temperature profiles with TGLF.

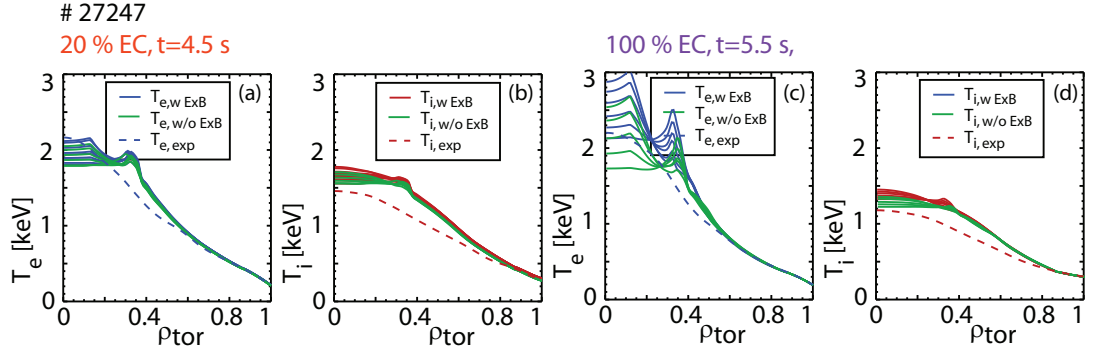


**Figure 6.10:** Influence of the  $E \times B$  shear on the modelling of  $T_e$  and  $T_i$  with TGLF. The two extreme cases of the low power, high collisionality discharge # 27247 are shown. Plot (a): comparison of the original modelling of  $T_e$  in the 20 % ECRH phase (blue) with the modelling without  $E \times B$  stabilisation (green). Plot (b): same comparison of  $T_i$ . Plot (c,d): same comparison for the 100 % ECRH case.

The comparison of the modelling with and without  $E \times B$  shear is shown in figure 6.10 for the two extreme cases of the low power, high collisionality discharge # 27247 of 20 % (plot (a) and (b)) and 100 % (plot (c) and (d)) of ECRH power. The originally modelled electron temperature is shown in plot (a) in blue in comparison with the modelling without  $E \times B$  shear in green and the experimental profile as dashed line. The same comparison for the ion temperature profiles is shown in plot (b). The electron and ion temperature show a slight decrease in the core when the  $E \times B$  velocity shear is switched off. However, the differences are marginal and lie well within the scatter of the experimental data. The same comparison for the discharge phase of 100 % ECRH power is shown in figure (c) and (d). In this case, the same situation is observed. The electron and ion temperatures inside the mixing radius is slightly reduced when switching off the  $E \times B$  shear in the model. The other analysed cases show a similar behaviour, namely a slight decrease of the temperatures without the  $E \times B$  velocity shear. However, in all performed modelling cases the influence was small to negligible. Only in discharges with highest NBI heating powers of 8 MW, resulting in large toroidal rotations, and lowest ECRH fraction of 15 % a tendency to a clear stabilising effect of the  $E \times B$  shear is evident.

In chapter 5.2 we have seen that the variation of the toroidal rotation is large, going to even negative values in the phase of ECRH only power. However, the absolute values of rotation are still small with a maximum value of only 60 km/s in the core for the NBI dominated cases. Accordingly the modelling shows on one side the general stabilising effect of the  $E \times B$  velocity heating as we observe some stabilising effects in the calculations. On the other side, it confirms that the values of rotation and rotational shear are



so small that their effect on the stability of microturbulences can be neglected in most of the analysed cases. In chapter 6.3 we come back to the influence of the  $E \times B$  shear rate and compare it with the growth rates of microinstability inferred from linear gyrokinetic simulations.

## 6.2 Comparison of all modelled discharges with the experimental database

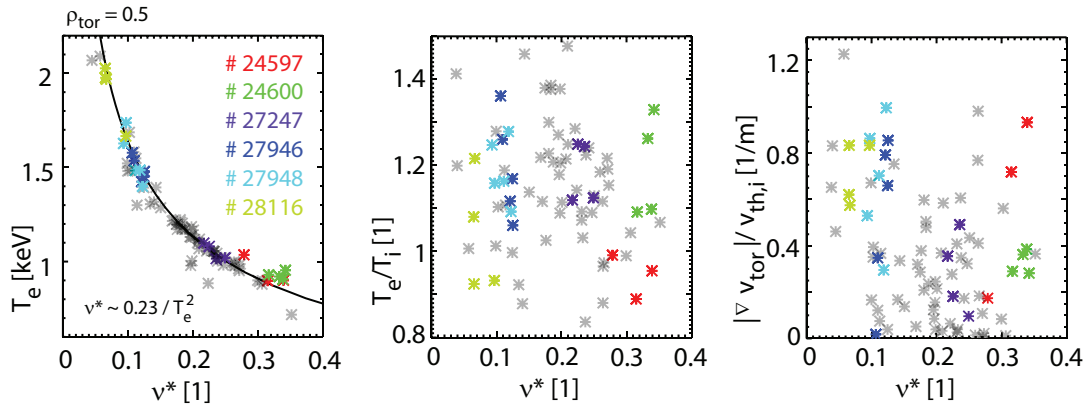
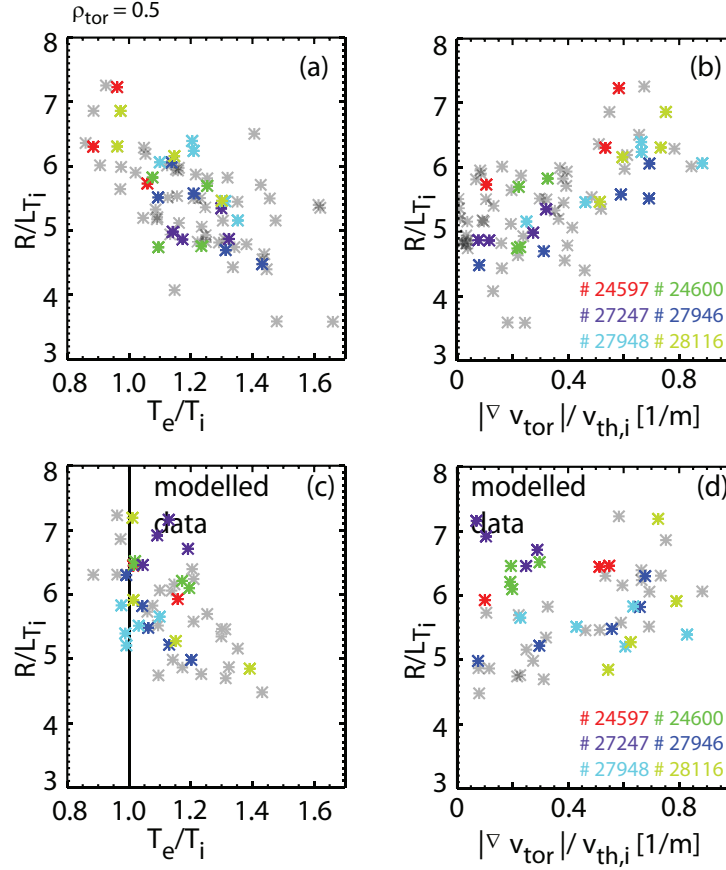


**Figure 6.11:** Subset of the whole database containing all discharges, which were modelled with TGLF in an equal representation as in figure 5.17. Correlations between the collisionality and  $T_e$  (plot (a)),  $T_e/T_i$  (plot (b)) and  $|\nabla v_{tor}|/v_{th,i}$  (plot (c)) at  $\rho_{tor} = 0.5$  using mixtures of NBI, ECRH and ICRH. The colour code depicts the different discharges. The pale black stars represent the whole database of non modelled discharges.

The detailed modelling of the two discharges # 27247 and # 28116 in the last chapters shows a reproduction of the main features and trends arising from a variation of the collisionality and the ECRH heating fraction. The same modelling has been done for a subset of 6 discharges in total covering a wide range of discharge parameters. Since the behaviour of the temperature profiles is almost identical for the temperature only modelling and the combined temperature and density modelling, in the following the results of the combined modelling are presented. The experimental and modelled values are taken at  $\rho_{tor} = 0.5$  if not otherwise stated. Due to the variation of the modelled profiles by sawtooth crashes, the values are averaged over 30 time steps corresponding to 150 ms simulation time and a radius of  $\Delta\rho_{tor} = 0.05$  to smooth out the disturbances of the sawtooth model on the profiles. The same radial average as for the experimental data in chapter 5.5 is used. In figure 6.11 the experimental data of this subset of modelled discharges are shown in colour. As comparison the whole database of non modelled discharges is shown as lucid black crosses. The plots are the same as in figure 5.17 for the whole database of experimental discharges. These plots show, that almost the whole parameter space of

## 6.2. COMPARISON OF ALL MODELLED DISCHARGES WITH THE EXPERIMENTAL DATABASE

$v^*$ ,  $T_e/T_i$  and  $|\nabla v_{tor}|/v_{th,i}$  of the entire database is covered by the subset of modelled discharges.



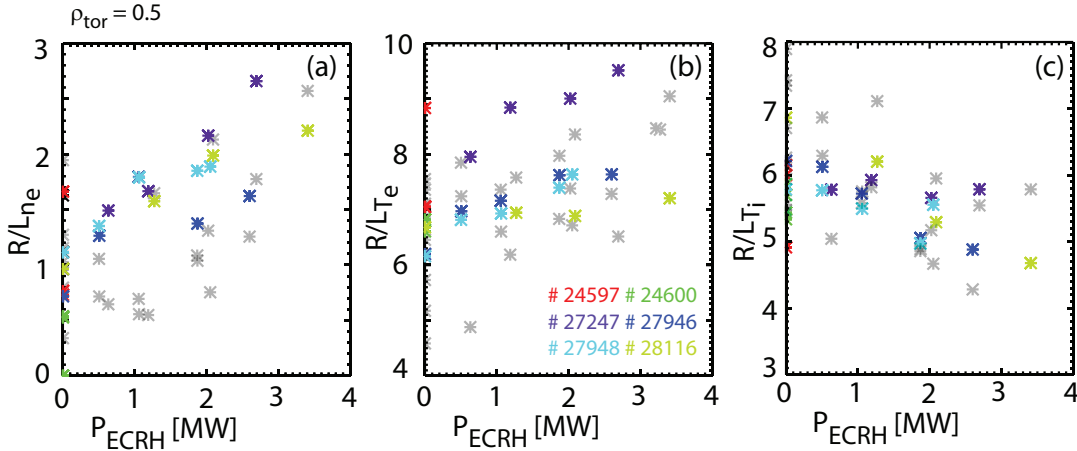
**Figure 6.12:** Comparison of the experimental dependencies shown in figure 5.19 with the modelled values. Plot (a,c) show the dependence of  $RL_{T_i}$  on  $T_e/T_i$  and plot (d,e) the dependence of  $RL_{T_i}$  on  $|\nabla v_{tor}|/v_{th,i}$ . Plot (a,b) show the experimental values of the modelled subset in colour, the whole database of non modelled discharges in pale black. Plot (c,d) show the corresponding values taken from the modelling in colour, the experimental data of the modelled discharges in pale black as comparison. For plot (d) the gradients of the rotation are taken from the experiment while  $v_{th,i}$  is calculated from the modelled values.

Figure 6.12 (a) and (b) show the experimental dependencies of  $RL_{T_i}$  on  $T_e/T_i$  and  $|\nabla v_{tor}|/v_{th,i}$  for the whole database in the same way as in figure 5.19. The experimental values of the modelled discharges are shown in colour, the values of the non modelled discharges are shown in pale black. The shown data is averaged over  $\Delta\rho_{tor} = 0.2$  to reduce the statistical error in the evaluation of the gradients. Also this representation shows the coverage of the whole database by the modelling. In this subset the decrease of the inverse gradient length of the ion temperature with increasing fraction of electron over ion temperature can be seen in plot (a). The increase of achievable inverse ion temperature gradient lengths with increasing normalised rotation can be seen in plot (b). For both dependencies the described trends are not only seen for the whole database but also for the different phases in one individual discharge.

The second row shows the corresponding dependencies for the modelled data in colour in comparison with the experimental data of the modelled discharges in pale black. In plot (c) the same trend can be observed as for the experiments, namely a decrease of  $RL_{T_i}$  with an increase of  $T_e/T_i$ . However, several differences are evident:

- The modelling does not reproduce cases in which the ion temperature lies above the electron temperature at mid radius. These cases would correspond in the experimental data to large inverse gradient lengths. TGLF does not reproduce the large gradients in these cases, which limits the maximum  $T_i$ . This again limits the minimum  $T_e/T_i$ .
- Most cases lie between  $T_e/T_i = 1.0$  to  $1.2$ . Accordingly TGLF has a higher tendency to equilibrate electron and ion temperature than observed in experiment. However, some cases remain which resemble the experimental observed high  $T_e/T_i$  fraction.

In conclusion, the general trend of the experimental data is reproduced, but extreme cases are pushed towards medium values of  $T_e/T_i$ . In plot (d) similar observations are made



**Figure 6.13:** Dependence of the inverse gradient lengths around mid radius with the level of ECRH power. Plot (a):  $RL_{n_e}$ , plot (b):  $RL_{T_e}$  and plot (c):  $RL_{T_i}$ . The experimental data are shown in pale black, the modelled values are shown in colour.

comparing the influence of  $|\nabla v_{tor}|/v_{th,i}$  on  $RL_{T_i}$  of the modelling with the experimental data. The plasma rotation can in principle also be modelled by TGLF, but since this component of the code is still tested by the developers we decided to take the gradients of the rotation from experiment. Since  $|\nabla v_{tor}|/v_{th,i}$  is only influenced by the square root of  $T_i$ , its values basically resemble the experimental data. The scatter of  $RL_{T_i}$  compared to the experimental observations is increased but the values of the modelled  $RL_{T_i}$  lie in the same band as the experimental data. The experimental trend of  $RL_{T_i}$  with increasing normalised rotation gradient is reproduced by the modelling, less pronounced, and with a larger scatter. For this subset, both the experimental and the modelled data show no dependence below  $|\nabla v_{tor}|/v_{th,i} = 0.4$  for the whole database. Above that value an increase

## 6.2. COMPARISON OF ALL MODELLED DISCHARGES WITH THE EXPERIMENTAL DATABASE

of the inverse gradient length is present. Having a closer look at different phases of one single discharge, an increase of  $RL_{T_i}$  with  $|\nabla v_{tor}|/v_{th,i}$  can be seen for all discharges.

The dependence of the inverse gradient length  $RL_{n_e}$ ,  $RL_{T_i}$  and  $RL_{T_e}$  on the injected ECRH power is shown in figure 6.13. The experimental data are shown in pale black, the modelled values are shown in colour code, depicting the different discharges. The inverse gradient length of the electron density in plot (a) and of the electron temperature in plot (b) increase considerably with increased ECRH fraction, which is expected with an increase of electron heating. The inverse gradient length of the ion temperature on the contrary decreases with ECRH fraction in plot (c). These observations can be made independently for the experimental data and the modelled values. The absolute values show a good reproduction of the experimental data by the modelling.

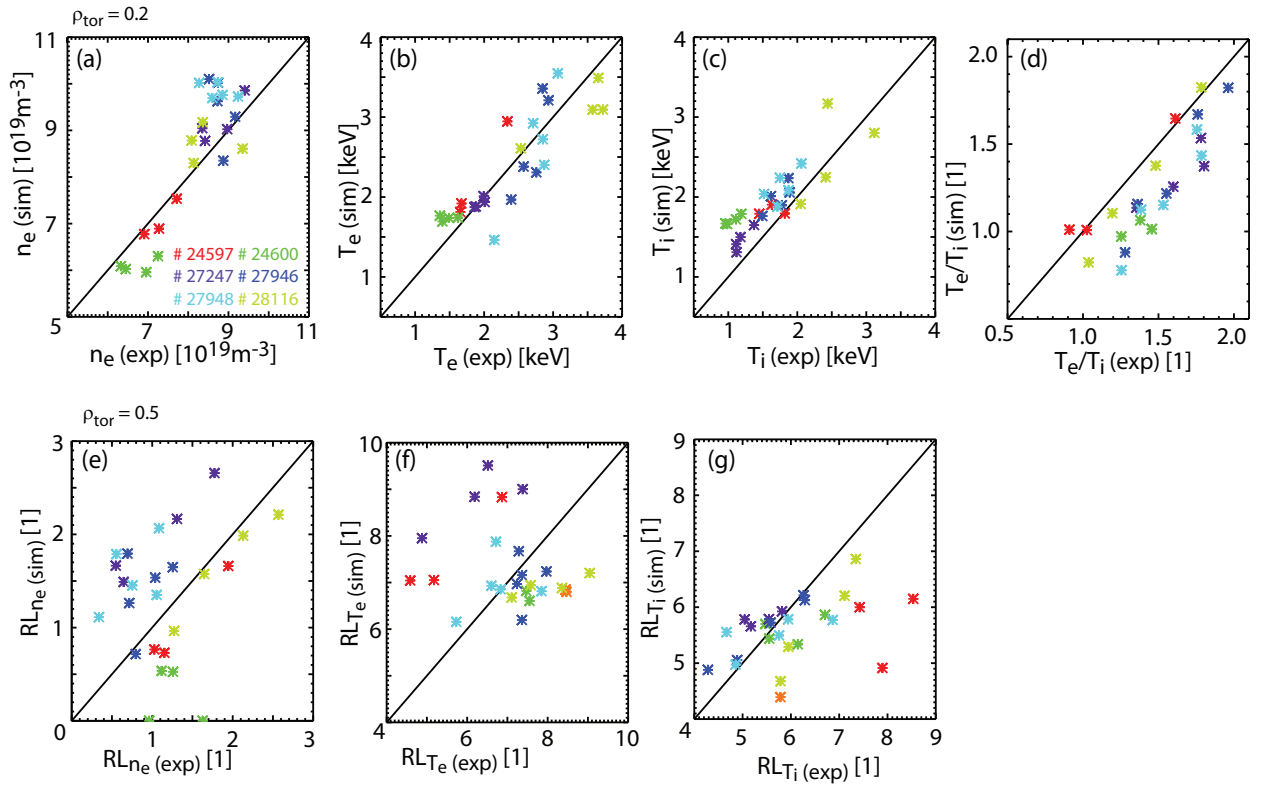


**Figure 6.14:** Comparison of the modelled values of the kinetic quantities with the experimental ones. Plot (a-d) show the values of  $n_e$ ,  $T_e$ ,  $T_i$  and  $T_e/T_i$  in the center at  $\rho_{tor}=0.2$ . Plot (e-f) show the values of  $RL_{n_e}$ ,  $RL_{T_e}$  and  $RL_{T_i}$  at  $\rho_{tor}=0.5$ .

The direct comparison of the modelled kinetic data with the experimental values is shown in figure 6.14 in the centre at  $\rho_{tor}=0.2$  for  $n_e$ ,  $T_e$ ,  $T_i$  and  $T_e/T_i$  in plot (a) to (d) and at  $\rho_{tor}=0.5$  for  $RL_{n_e}$ ,  $RL_{T_e}$  and  $RL_{T_i}$  in plot (e) to (f). A line through origin is added to every plot to better focus on the perfect proportionality. The modelling reproduces the electron density in general good, but tends to overestimate densities around  $9 \cdot 10^{19} m^{-3}$ . Especially the density increase during one discharge with varying ECRH fraction is reproduced clearly. The electron temperature in plot (b) shows good agreement of the modelled data with the experimental one. The ion temperature in plot (c) shows a slight

overestimation of the modelled values. Hence  $T_e/T_i$ , shown in plot (d), experiences an underestimation over the whole range of values. The modelled inverse gradient length of the density around mid radius basically follows the experimental trend but shows a large scatter (plot (e)). The inverse gradient length of the electron temperature shows a large scatter and no clear correlation of all cases with the experimental values in plot (f). The inverse gradient length of the ion temperature (plot (g)) shows a strongly reduced range of modelled values compared to the experimental observations with approximately the same mean value around 5 to 6. As a result, very high and low values differ strongly from their experimental ones. For all shown quantities the following observation holds: Even if the scatter perpendicular to the line through origin for the whole database is large, the simulated data of different phases of one discharge follow the experimental trend very closely. Since TGLF is a first principle based model, which does not rely on fits to experimental databases, and all modelling cases were conducted with exactly the same modelling parameters, this result can be considered very good.

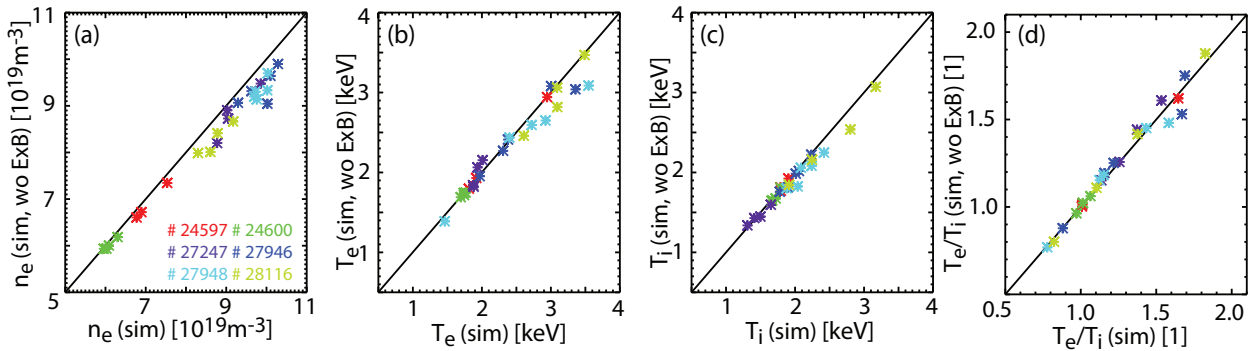


**Figure 6.15:** Comparison of the kinetic quantities of the modelling without ExB shear with the normal modelling presented in figure 6.14. Plot (a-d) show the values of  $n_e$ ,  $T_e$ ,  $T_i$  and  $T_e/T_i$  in the center at  $\rho_{tor}=0.2$ .

The comparison of NBI and ICRH heated discharges in chapter 5.2 and 5.3 showed no apparent influence of the rotation on the global performance of the discharge or the kinetic profiles. Also the sensitivity study of the modelling to the  $E \times B$  shear for single time points presented in chapter 6.1.5 showed no significant change of the modelled temperatures. These observations are confirmed by figure 6.15 in which the kinetic profiles of the normal modelling presented before (x-axis) is compared with modelling calculations in which the ExB shear term is switched off in TGLF (y-axis). High densities are slightly lower without ExB shear, which shows its small stabilising effect. The electron and ion temperatures agree very well between the two modelling cases reassuring our previous observations that this term is either not relevant in this parameter space or the variation is too small to produce a noticeable effect.

## 6.3 Linear gyrokinetic calculations

The main source of heat transport in a tokamak plasma is the turbulent transport. Chapter 2.3 presents the various mechanisms which can contribute to this transport. Computer simulations which solve the gyrokinetic equations can be used to calculate the growth rates and mode frequencies of ITG, ETG and TEM microinstabilities. They can determine the fundamental, most unstable mode which is responsible for the turbulent heat transport in the different analysed phases and heating mixes. Furthermore the calculations allow conclusions on the corresponding heat fluxes. Several gyrokinetic calculations were conducted with the gyrokinetic code GS2 (see chapter 2.6). The code can be run in linear or non linear manner. We decided to use the code in linear mode to reduce the computational times significantly so that several parameter scans could be performed. No statement on the absolute values of the heat fluxes can be made running the code in linear mode. However, the comparison of the quasi linear cross phase between pressure and potential fluctuations, which is a measure of the heat flux, allows a qualitative comparison of the different heating mixes. The calculations were conducted for all heating mixes of two discharges, the low power, high collisionality discharge # 27247 and the high power, low collisionality discharge # 28116. The simulations were performed at several radii to obtain a possible radial dependency of the dominant microinstability.

The ion gyroradius sized instabilities ITGs and TEMs and the electron gyroradius sized instabilities ETGs have different radial extensions and hence different poloidal wave numbers. The distinction is roughly given by the difference of their gyroradii. The mode wave number  $k_y \cdot \rho_i$  was scanned from 0.1 to 30 in the calculations to determine the most unstable mode.  $k_y$  stands for the wave number in poloidal direction and  $\rho_i$  for the ion Larmor radius. This range was chosen since it covers the expected wave numbers of ITGs/TEMs and ETGs. Neglecting finite Larmor radius (FLR) effects the growth rate is proportional to the poloidal (binormal) wave number [121]. This implies a faster growth at smaller scales. On the other side, the gyro-motion of the considered species suppresses the instability and stabilises the mode when scales become comparable to the Larmor radius. This implies a decrease of the growth rate of the ITGs towards zero around  $k_y \cdot \rho_i = 1$ . Naturally both constrains lead to maximal growth rates in the range of  $k_y \cdot \rho_i = 0.3$  to  $0.4$  since  $\gamma$  does not rise monotonously with  $k_y \cdot \rho_i$ . This resembles a radial extent of some ion gyroradii:  $1/k_y = \rho_i / (0.3 \text{ to } 0.4) = 2.5 \text{ to } 3.3 \rho_i$ . For the ETGs the argument is basically the same replacing the ion Larmor radius with the electron Larmor radius. The difference between the Larmor radii of ions and electrons is given for  $T_e = T_i$ :

$$\sqrt{\frac{m_i \cdot T_i}{m_e \cdot T_e}} \approx 60 \quad (6.1)$$

Consequently the maximum growth rates for ETGs are expected around  $k_y \cdot \rho_e = 0.3$  to  $0.4 \approx k_y \cdot \rho_i = 28$  to  $24$ . The calculations show a maximum of the growth rates typically at slightly smaller wave numbers around  $k_y \cdot \rho_i = 10$ . This complies with a radial extent of a few electron gyroradii:  $1/k_y = \rho_i / 10 = 0.1 \rho_i = 6.5 \rho_e$ . The resulting growth rates  $\gamma$

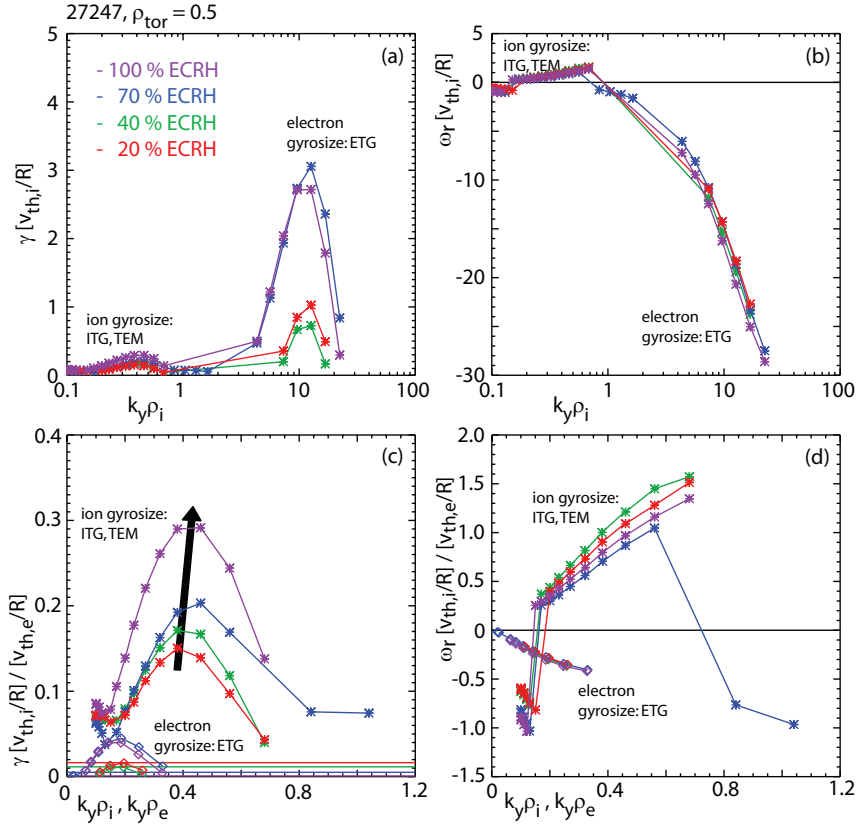


**Figure 6.16:** Linear gyrokinetic simulations of the low power, high collisionality discharge # 27247 with GS2. Plot (a): growth rate in units of  $v_{th,i}/R$  as function of wave number  $k_\theta \cdot \rho_i$ , plot (b): according mode frequency in units of  $v_{th,i}/R$ , plot (c,d): same quantities with ETG part normalised to its natural values: growth rates and frequencies to  $v_{th,e}$  and wave numbers to  $k_y \cdot \rho_e$ . In addition the  $E \times B$  shear rates are shown for comparison.

and the mode frequencies  $\omega_r$  are expressed in units of  $v_{th,i}/R$ . The calculations of growth rates (a) and mode frequencies (b) are shown in figure 6.16 for the low power, high collisionality discharge # 27247 at a radial position of  $\rho_{tor} = 0.6$ . Since the whole spectrum is expressed in units of  $v_{th,i}/R$  as function of the wave number  $k_y \cdot \rho_i$ , the peak around  $k_y \cdot \rho_i = 0.4$  represents the ITG and TEM instabilities, and the peak around  $k_y \cdot \rho_i = 10$  represents the ETG instability as outlined before.

The growth rates and frequencies can be normalised to the corresponding thermal velocities divided by the major radius and the wave numbers to the gyroradii to compare the actual strength of the ion and electron Larmor radius sized instabilities. This estimate is consistent with multi scale non linear simulations, which show relevant heat transport by ETGs only for  $\gamma_{ETG}/\gamma_{ITG} > \sqrt{m_i/m_e}$  [122, 123]. This normalisation allows a meaningful comparison of the growth rates and frequencies of ITG/TEMs and ETGs and to determine the most relevant microinstability for heat transport. This normalisation leads to a division by roughly 60 for the ETG part of the wave numbers, growth rates and frequencies, which lie above a wave number of  $k_y \cdot \rho_i = 1.2$ . The resulting curves can be seen in figure



### 6.3. LINEAR GYROKINETIC CALCULATIONS

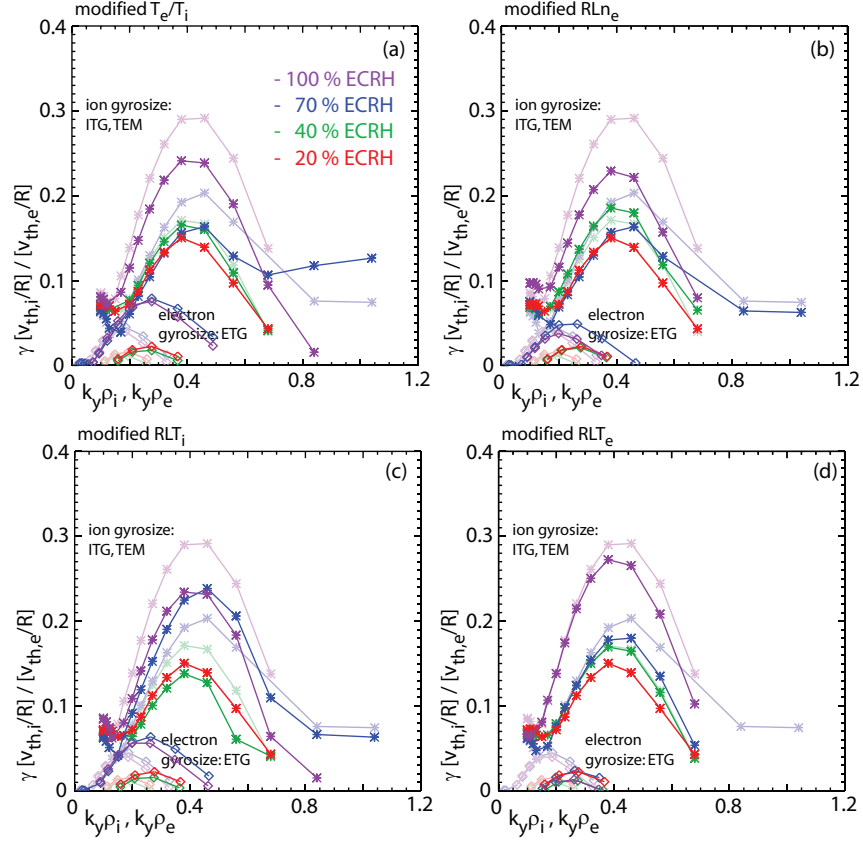


**Figure 6.17:** Linear gyrokinetic simulations of the low power, high collisionality discharge # 27247 with GS2 comparing the impact of different destabilising effects on the growth rate. Therefore the values of  $T_e/T_i$ ,  $RL_{n_e}$ ,  $RL_{T_i}$  and  $RL_{T_e}$  are exchanged individually with the values of the 20 % ECRH phase (red). The resulting growth rates are shown in plot (a) to (d). As comparison in every plot the original calculations from figure 6.16 (c) are shown in pale colour.

6.16 (c) and (d). The growth rates of the ITG/TEM branch of the spectrum clearly exceed the ETG branch by at least a factor of 4 making the most dominant instability an ion gyroradius sized instability (ITG or TEM). The mode frequencies are shown in plot (d). The frequencies of the branch corresponding to ITGs and TEMs show positive values. This implies a rotation in the ion diamagnetic drift direction and identifies the most unstable mode as an ITG mode in all considered cases. This is consistent with power balance analysis presented in chapter 5.3 in which the heat transport in the ion channel clearly dominates over the heat transport in the electron channel around mid radius.

The modelling calculations with TGLF in chapter 6.1.5 showed only a marginal influence of the  $E \times B$  shear on the modelling of the temperature profiles. This is also verified by comparing the  $E \times B$  shear rate with the growth rate calculated by GS2. The  $E \times B$  shear rates for the radial position of  $\rho_{tor} = 0.6$  are shown additionally in plot (c) for all heating mixes. In the NBI dominated case (red) the stabilising effect is around 10 % of the growth rate. This is in line with the findings reported in chapter 6.1.5 where a slight decrease of the modelled temperature without  $E \times B$  stabilisation compared to the normal modelling

is evident in figure 6.10 (a). This stabilising effect in gyrokinetic calculations diminishes down to only 0.3 % of the growth rates for the ECRH only phase (purple). This underlines the former statement that the  $E \times B$  shear rate is not important for the evaluation of heat transport and thus for the build-up of the profiles in these cases of low plasma rotation.

In addition increases of the growth rates towards higher fraction of ECRH power are evident. The linear gyrokinetic growth rates do not permit a direct conclusion as to heat diffusivities but the quasi linear cross phase between pressure and potential fluctuations as a measure for the heat flux can be calculated. It allows a qualitative comparison of the different heating mixes. The ion heat flux determined from this cross phase increases significantly with increasing electron heating fraction. This increase goes in line with the increase of the ion heat diffusivity  $\chi_i$  with ECRH power as described in chapter 5.3.

The gyrokinetic calculations were analysed with regard to the impact of different destabilising effects of ITG modes, i.e.  $T_e/T_i$ ,  $RL_{n_e}$ ,  $RL_{T_i}$ ,  $RL_{T_e}$  and the magnetic shear. For that purpose the calculations of all heating mix phases were performed for a second time, only replacing one of these parameters individually with the value of the 20 % ECRH phase. The resulting growth rates are presented in figure 6.17 and compared with the original calculations from figure 6.16 shown in pale colour. The global structure of the growth rate spectra is not affected by any of the changes and the ITG/TEM branch still shows a pronounced peak around  $k_y \cdot \rho_i \approx 0.4$ . For all cases the ITG/TEM branch is larger at least by a factor of two compared to the ETG branch. The mode frequencies are almost unaffected by the performed changes by up to 5 % at the most. In all cases they have positive values, implying a rotation in the ion diamagnetic drift direction.

The spectral location of the ETG growth rate peaks are shifted and the growth rates increase in some cases. However, a clear domination of the ITG over the ETG as most unstable microinstability is evident for all calculated cases. The exact ETG contribution is still potentially non negligible, but requires multi scale non linear simulations to be determined. The largest impact is achieved by replacing  $T_e/T_i$  (see plot (a)), which reduces the growth rates of the two high ECRH fraction phases by about 20 %. The replacement of  $RL_{n_e}$  has a similar effect shown in plot (b), namely a reduction of the growth rates of the dominantly electron heated phases. The replacement of  $RL_{T_i}$  results in a small increase of the growth rates of the 70 % ECRH phase and a 20 % reduction of the growth rates of the other two phases.  $RL_{T_e}$  reduces the growth rates by less than 5 %. The replacement of the magnetic shear has close to zero influence on the calculation (w/o figure). These calculations show that the changes of  $T_e/T_i$ ,  $RL_{n_e}$  and  $RL_{T_i}$  from dominant NBI to ECRH only heated phases are equally responsible for the increase of the ITG growth rate. The change of  $RL_{T_e}$  carries only a minor contribution.

The same analysis was executed for the high power, low collisionality discharge # 28116 with results shown in figure 6.18. In the plot the data are shown normalised to the corresponding gyroradii and mode numbers. Also in this case the growth rates of the ITG/TEM modes exceed the growth rates of the ETG modes by at least a factor of 2 showing their dominant role in turbulent heat transport. The frequencies of the modes with largest growth rates are positive for all cases, which identifies them as the ITG mode due to its

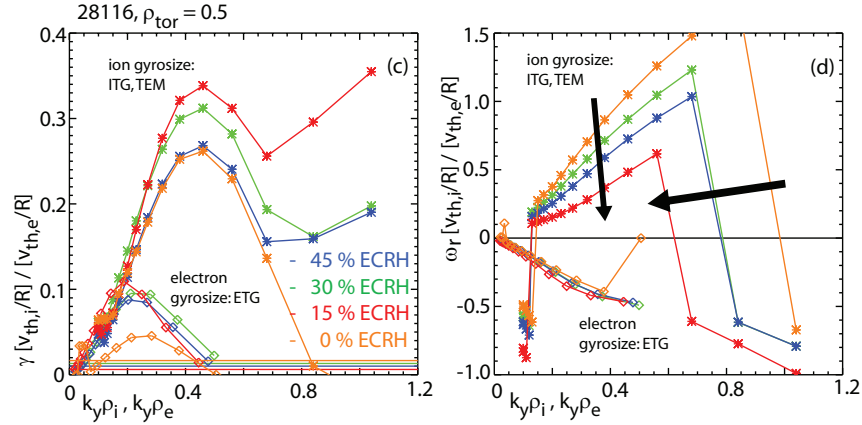


**Figure 6.18:** Linear gyrokinetic simulations with GS2 of low collisionality discharge # 28116. Plot (a): growth rate in units of  $v_{i,th}/R$ ,  $v_{e,th}/R$  as function of wave number  $k_y \cdot \rho_i$ ,  $k_y \cdot \rho_e$ . Plot (b): according mode frequency in units of  $v_{i,th}/R$ ,  $v_{e,th}/R$ . Additionally the  $E \times B$  shear rates are shown, which have insignificant values compared to the growth rates of the microinstabilities.

rotation in the ion diamagnetic drift direction. However, with increasing ECRH fraction from 0 % to 45 % the frequency is reduced by a factor of 2 and approaches zero. This indicates an approach to conditions where TEMs are more unstable. It is also observed that the jump from positive to negative frequencies in figure 6.18 (b) moves towards the range of mode numbers with the largest growth rates. The TEMs are typically more unstable at higher mode numbers than the ITGs. This is another proof for the transition from ITG dominated to TEM dominated heat transport when approaching dominant electron heated conditions by an increase of the ECRH fraction. With increasing electron heating  $T_e/T_i$ ,  $RL_{n_e}$  and  $RL_{T_e}$  are increasing while  $RL_{T_i}$  is decreasing. All of these trends favour the transition from ITG dominated to TEM dominated regime. As shown in chapter 5.3 the peaking of the electron density is large in this discharge and shows no variation with changing heating mix. This behaviour is also reproduced by TGLF modelling presented in 6.1. The invariance of density peaking is expected in this transition region from ITG to TEM dominated microinstability regime and completes the theoretical description of the experimental observations.

Performing the calculations at different radial positions showed for both discharges a more pronounced domination of the ITG modes over the ETGs and TEMs at larger  $\rho_{tor}$ . For  $\rho_{tor} < 0.4$  the analysis indicates similar growth rates for ion and electron gyroradius sized instabilities and a jump to negative frequencies (TEM domination) around  $k_y \rho_i = 0.4$ . However, going towards the core the code converges for less and less mode numbers so that a complete analysis was not possible and general statements can not be given.

In conclusion, all analysed discharges are ITG dominated from mid radius to the edge. At high collisionalities they show an increased heat transport with increasing electron heating which is consistent with experimental observations. At low collisionalities and high electron heating fractions the influence of the TEM grows constantly. With higher ECRH power fractions the transition from ITG to TEM dominated regime might be possible [98].



# Chapter 7

## Summary and conclusions

This work contributes to the study of the influence of the heating mix on discharge performance. The response of the plasma to the change of heating from mixed ion and electron heating to dominant electron heating was analysed in depth.

The thorough investigation is motivated by the change of dominantly heated species going from current fusion experiments to future devices like ITER or DEMO. The ratio of the total heating power deposited to electrons will increase from currently 50 % to around 90 %. On one side, this transition arises from an increased use of ECRH and LH systems, both solely heating the electrons. On the other side, an increase of the NBI beam energy and the rising importance of  $\alpha$ -particle heating will lead to a growing energy transfer from fast ions to electrons. At present the major heating systems of fusion experiments are ICRH and NBI, which both typically transfer their power half to the electrons and half to the ions. This work significantly extends the experimental foundation of the future heating regime of dominant electron heating. In this thesis the change of heating mix was realised by making use of the recently upgraded ECRH system at ASDEX Upgrade. This upgrade enables now the replacement of a great fraction of NBI or ICRH by ECRH power for high power H-mode discharges while keeping the total heating power at constant level.

At low heating power resulting in high collisionality next to no degradation of the global plasma parameters such as  $W_{MHD}$ ,  $\tau_E$ ,  $H_{98}$ ,  $\beta_N$ ,  $H_\alpha$  or  $f_{ELM}$  is observed under transition from mixed ion and electron heating to pure electron heating. The edge values of the electron density and the electron and ion temperatures are unaffected. The electron density shows an increased central peaking with increased ECRH power fraction. In the core the electron temperature increases and the ion temperature decreases with increasing ECRH power fraction. The toroidal rotation in the centre and at the edge decreases to even negative values in the 100 % ECRH phase caused by the missing torque input from the absent NBI contribution and the remaining residual stress. The poloidal rotation at the edge is low and independent of the heating mix.

The power balance analysis shows a large impact of the heat exchange term due to Coulomb collisions on the heat fluxes.  $P_{e \rightarrow i}$  decreases the electron heat flux and increases the ion heat flux. The heat flux in the electron channel is large at the ECRH deposition location and approaches zero towards the edge. Therefore the ions carry all the heat at the edge, and their heat flux in the entire plasma is independent of the heating mix. The electron heat diffusivity is very large at the ECRH deposition location and decreases to small values towards mid radius. It grows slightly with increased ECRH power fraction. The large ion heat flux is the consequence of a domination of ion heat diffusivity over electron heat diffusivity at similar temperatures in most parts of the plasma in all heating mixes. The ion heat diffusivity shows a slight increase with ECRH power fraction.

These observations are in line with gyrokinetic simulations which show a clear dominance of the ITG mode for heat transport. Furthermore these calculations exhibit an increase of the quasi linear cross phase between pressure and potential fluctuations, which is a measure of the heat flux in the ion channel with increasing ECRH power fraction. With the trapped gyro-Landau fluid transport model TGLF the electron temperature and density profiles could be reproduced. To prevent a too peaked electron temperature profile in the modelling a realistic sawtooth model is applied. This way it is possible to reproduce the shape of the profiles, the sawtooth crashes including their radial extension and energy expulsion, and the increasing  $T_e/T_i$  with increasing ECRH power fraction. The comparison of the modelled profiles with the experimental data shows excellent agreement. Only the ion temperature is in general slightly overestimated.

Additional experiments replacing ICRH by ECRH power at the same low total heating power and high collisionality show no difference in global plasma performance and kinetic profiles compared to a similar discharge replacing NBI by ECRH power. The only difference between these two discharges is the toroidal rotation which resides around zero in the ICRH plus ECRH heated discharge. Consequently the rotation and rotational shear does not play a noticeable role in the stability of the discharge in the high collisionality regime.

The analysis of the radial electric field at the edge for a medium power discharge did not show any variation with changing heating mix. This is in line with the unchanged pedestal values of density and temperatures modifying the heating mix.

Discharges at high heating power resulting in low collisionalities showed a slight degradation of global plasma performance with increasing electron heating. Due to tungsten accumulation for NBI only phases and limited ECRH power, only phases between 15 % and 45 % ECRH power could be performed. The plasma radiation increases and the stored energy, energy confinement time, the H-factor and the normalised  $\beta_N$  decrease by 10 % with increasing ECRH power fraction, whereas the  $H_\alpha$  signal and the ELM frequency remain unchanged with varying heating mix. The density profile shows a strong peaking, which stays unchanged when modifying the heating mix. The entire electron temperature profile and the edge value of the ion temperature remain unchanged by a change of the heating mix, whereas the core value of the ion temperature decreases drastically with increasing ECRH power fraction. These features give enough explanation for the reduction

---

of the stored energy. In these plasmas the heat exchange term due to Coulomb collisions shows a smaller impact on the power balance analysis but is sufficient enough to make the ion heat flux independent of the heating mix. Therefore the electron heat flux has a non negative value at the edge. Also in this discharge the ion heat diffusivity is dominant and both heat diffusivities show an increase with ECRH power fraction. Linear gyrokinetic simulations show a dominance of the ITG mode, but a growing importance of the TEM towards larger ECRH power fractions. The modelling of the kinetic profiles shows excellent agreement with the experimental data for this low collisionality discharge.

The analysis of the whole database of performed discharges shows a wide range of plasma parameters, e.g. collisionality,  $T_e/T_i$  and  $|\nabla v_{tor}|/v_{th,i}$  covered by the discharges with varying total heating power and heating mix. In previous studies a degradation of  $RL_{T_i}$  with  $T_e/T_i$  and an elevation with  $|\nabla v_{tor}|/v_{th,i}$  was reported for low  $T_e/T_i$  discharges. These trends are very well confirmed by the analysis of high  $T_e/T_i$  discharges performed in this work. The modelling of the kinetic profiles was done for a subset of 7 discharges in total. Care was taken that they cover the major part of the parameter space of the experimental observations. The previously described behaviour of  $RL_{T_i}$  was reproduced by the modelling, but in a less pronounced way. A direct comparison of the modelled quantities with the experimental observations shows in general a fine agreement. Especially the trends observed for the different phases in each discharge are reproduced very well.

The application of wave heating in the performed experiments does not result in a severe degradation of global plasma parameters. However, for low collisionalities the ion temperature decreases significantly. Decreasing the collisionality further towards ITER values seems at first to further increase the separation of ion and electron temperature. Also a negative global effect on the plasma performance is to be expected approaching high ECRH power fractions. In ITER the collisionality will be smaller by an additional factor of 5 to 10 compared to the lowest achieved collisionalities in this work depending on the scenario [34]. Since ITER will already be dominantly electron heated it could be assumed based on the previously available database of mixed ion and electron heated plasmas that these considerations point towards an exaggerated prediction of the ITER performance.

However, in ITER also the energy confinement time is expected to be larger compared to values typical today. The estimated ITER  $\tau_E$  value of 3.4 s [6] equals a factor 20 to 70 larger compared to the  $\tau_E$  values of the discharges conducted in this work which had energy confinement times in the range of 50 to 160 ms. Since the increase of the collision time is overcompensated by the increase of the confinement time, the equilibration between electron and ion channel will be also increased. Despite less frequent collisions of electrons and ions, there is more time to exchange energy. These basic considerations are backed by the modelling of electron and ion temperatures of ITER with GLF23 [60] and NCLASS [119] models, which show a small difference of only a few percent between the temperatures [124].

The situation is different for high performance preparatory experiments for ITER at available smaller devices. On one side the collisionalities are pushed towards low, ITER rele-



vant values. On the other side, and quite contrary to the expectations for ITER, the energy confinement times are typically reduced due to their negative dependence on the heating power which is not compensated by other effects, e.g. the size of the devices. The combination of these two effects results in a poorer performance of the discharges than is expected for ITER when applying large amounts of ECRH. The evaluation of such experiments and the projection towards ITER have to be carried out carefully, and the effects described previously have to be taken into account.

This work shows that the influence of changing the heating mix from mixed electron and ion heating to dominant electron heating on the discharge performance increases with decreasing collisionality. The observed phenomena can be modelled to a great extent with available first principle codes showing the understanding and the computational implementation of the major effects on profile stability outside the pedestal region. Since discharges conducted at present can only approach ITER relevant values for singular parameters, direct interpolations to ITER plasmas are not advisable. The results of this work draw a consistent picture of the observed phenomena. The findings of the main topics discussed support the fundamental assumption that the used codes allow reliable predictions as to performance and achievable parameter space of future fusion devices.

# Chapter 8

## Outlook

During the preparation of this thesis several topics arose for additional investigations and are presented in the following as an outlook to further analysis:

- Detailed ELM analysis

First already existing analysis show an influence of the heating mix on the ELM behaviour [106]. The comparison of the ELMs from three phases of one discharge

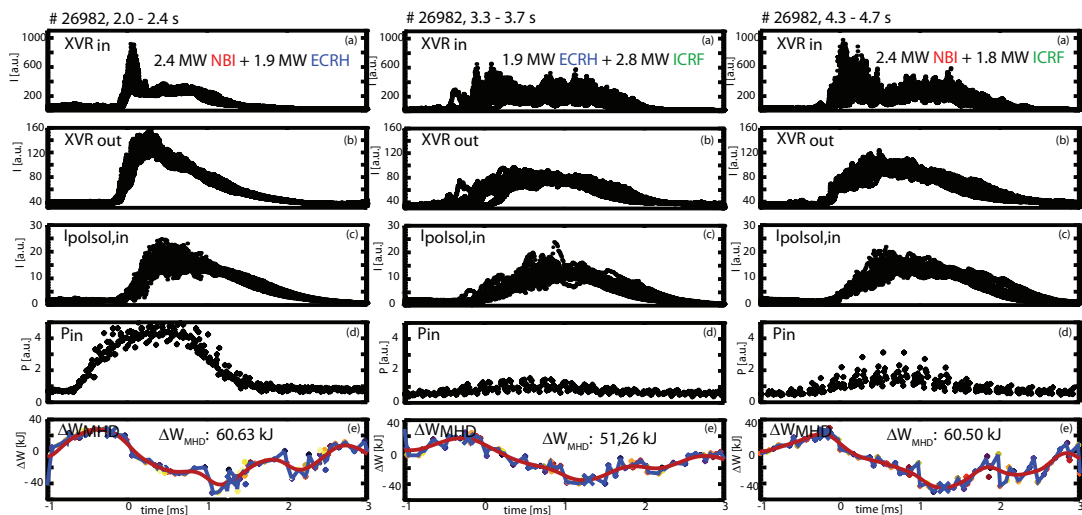


**Figure 8.1:** ELM onset synchronised time traces for discharge # 26982: plot (a) and (b): diode bolometer looking from the top to the inner and outer divertor; plot (c): SOL currents to the inner divertor; plot (d): deposited power on the inner divertor, measured with the thermography; plot (e): loss of stored energy.

with very similar total heating powers of 4.5 MW but varying heating mix is shown in figure 8.1: NBI + ECRH in column 1, ECRH + ICRH in column 2 and NBI +

ICRH in column 3. Plot (a) and (b) show the bolometer signal originating from the inner and outer divertor, plot (c) shows the SOL currents to the inner divertor, plot (d) shows the deposited heat load on the inner divertor and plot (e) shows the loss of stored energy per ELM. The plots contain the time traces of all ELMs during a 0.4 s time window synchronised on the start of the ELM. The almost perfect overlay of all ELM traces shows the similarity of all ELMs in each phase. The first phase shows a very pronounced burst in all measurements which has a duration of only 20  $\mu$ s in the bolometer signal. The NBI + ICRH phase shows a less pronounced peak at the start of the ELM and a slower increase of the measured values. A candidate for the observed behaviour could be the fast ion contribution in the plasma which is expelled by the ELMs. A detailed analysis on the topic including changing divertor conditions could verify this hypothesis.

- TGLF modelling of ITER discharge

The current version of TGLF is well tested and reproduces experimental observations of ASDEX Upgrade very well. Therefore the modelling of a discharge with ITER vessel dimensions and expected parameters could be performed to affirm existing modelling results, e.g. the modelling of ITER temperature profiles with TGLF presented in [125].

- Analysis of discrepancy between TGLF modelling and experimental observations

The comparison of modelled kinetic profile data with experimental observations presented in chapter 6.1 showed good agreement. However, slight deviations could be observed. The analysis of these differences between modelled and experimental data gives the opportunity to examine additional physic effects which are not yet covered by the code. Their identification and implementation would also lead to an improved understanding of the transport mechanisms in plasmas.

- Temporal behaviour of change of heating mix

This work concentrates on the steady state analysis of different heating mixes. In addition the analysis of the temporal behaviour at the moment of heating mix switch could be of interest. First analysis leads to the following qualitative sequence of change from dominant NBI to dominant ECRH heating: The increased electron heating leads to an increased electron temperature, especially in the core. The following decrease of the ion temperature can be explained by an increased heat flux in the ion channel due to a decreased threshold of the ITG instability caused by the increase of  $T_e/T_i$ . The further increase of  $T_e/T_i$  leads to a larger heat exchange due to Coulomb collisions from electrons to ions, which reduces the electron temperature to values close to the ones before the change of heating mix.

- Modulation experiments

Heat pulse analysis can be performed with the modulation of ECRH power. The short and localised deposition of its power induces a heat wave travelling perpendicular to the flux surfaces. From the measurement of the propagation velocity and the amplitude decay, further insight of the heat flux could be gained.

---

- Enhancement of ECRH

A further Upgrade of the ECRH system at ASDEX Upgrade currently under construction will lead to a total ECRH power of 8 MW for 10 s. This upgrade will allow the exchange of the entire NBI by ECRH power for high power discharges. Partial replacement experiments will be feasible at even higher total heating powers decreasing the collisionality even further. Both measures are expected to induce a transition from ITG to TEM dominated plasma regime. With this transition the heat fluxes are expected to change significantly. A valuable confirmation of the predictive capability of TGLF would be the correct modelling of the kinetic profiles also in these discharges.

- Upgrade of ICRH

An upgrade is planned in 2014 for two of the four ICRH antennas to equip each of them with three straps to reduce the electric fields near the antennas [76]. This is expected to allow a total ICRH power of 5 MW without a destructive increase of tungsten concentration in the plasma. This upgrade will enable the analysis of medium power H-modes replacing ICRH by ECRH power. The influence of rotation and rotational shear on the plasma performance and the kinetic profiles in this low collisionality regime could be investigated, which might differ from the behaviour at high collisionalities reported in this work. This would help to disentangle the change of the plasma due to different heating by NBI and ECRH and the different torque input at higher heating powers.

These investigations would pursue the analysis of the influence of the heating mix on discharge performance. They would help to enlarge the knowledge of the underlying physical mechanisms further and could increase the predictability of future fusion devices.



# Acknowledgements

Last but not least I want to express my deep gratitude to all people who helped and supported me during the last three years. Without you this thesis would not have been possible.

First of all I want to thank Prof. Dr. Hartmut Zohm as my academic advisor who gave me the possibility to execute this work at the Max Planck Institute für Plasmaphysik, Garching. The discussions with you were always reassuring how my work fits in the global scientific programme of the institute and brought up new aspects and directions to look into.

Next I want to thank Dr. Jörg Stober, my direct supervisor. You introduced me to the whole topic of heat transport and heating systems, especially the ECRH. You always had time to discuss questions about my thesis, the current status of my work and in which direction I should investigate further. You helped to plan and execute the experiments. On one side you gave me the time and freedom to follow a specific direction or topic for a while. On the other side you brought me to see the whole picture of my work, and to combine the different parts and topics to a whole. The torbeam GUI builds on a programme developed by you.

My thanks goes to Dr. Clemente Angioni, the leader of the transport task force at ASDEX Upgrade who organised this part of the experimental campaign. You made the experiments possible and supported me with suggestion of further investigations. In addition you supplied me with the access to GS2, explained the structure of the input file and helped with the interpretation of the results in numerous discussions.

I want to thank the late Dr. Gregory Pereverzev for providing me with ASTRA and teaching me the preparation of the input data and usage of the code. This was continued by Dr. Emiliano Fable who supplied me with the new version of ASTRA 7 and the equilibrium solver SPIDER. You implemented TGLF in its newest version in ASTRA and made that available to me. I especially want to thank you for our countless discussion about optimising the input to ASTRA, finding errors in the model file and interpreting the obtained results. You were always available for questions and discussion and responded to requests for enhancements of the code immediately.

## CHAPTER 8. OUTLOOK

---

I thank Dr. Giovanni Tardini for facilitating the use of TRANSP for me and teaching me how to prepare the input data and the namelist. Very helpful in this respect was your programme `trgui` for largely automated input generation for TRANSP and also for ASTRA. You were always available for questions about TRANSP and to extend your programmes.

Furthermore my thank goes to Matthias Bernert, who prepared the bolometric deconvolution for me. I thank Dr. Volodymyr Bobkov for the help in planning and execution of the ICRH experiments. I thank Andreas Burckhart, who provided shotfiles for the ELMs and sawtooth crashes. I want to thank Livia Casali and Dr. Alexander Mlynek for correcting the DCN interferometer data due to fringe jumps. I want to thank Dr. Rainer Fischer for providing me with IDA data. My gratitude goes to Dr. Rachael McDermott for the beam blip analysis of CXRS data. I want to thank Dr. Eleanora Viezzer for the analysis of the edge CXRS data and for the computation of the radial electric field at the edge. My thank goes to Dr. Garrard Conway, who provided me with very helpful code fragments for `tb_gui`.

I want to thank the experimental leaders who conducted the discharges and always had open ears for questions and helped with suggestions to improve the discharges. I thank all the diagnosticians, and scientific and technical staff at ASDEX Upgrade. Everyone of you helped for the successful and smooth execution of the experiments and the preparation of this thesis.

I want to thank all other PhD students and especially the 12:30 lunch group to make these three years not only a professional success, but also an enjoyable personal experience. Your friendship and moral support helped through strenuous phases and the (not always) physics free conversation at lunch prepared for an effective afternoon of work.

My gratitude goes to my mother Helgard Sommer-Klix and my father Klaus Sommer. Both of you supported me in every phase of my work no matter what by encouraging words, a great dinner, fine-tuning the wording or just by appreciating my limited time and following from this, my absence. I want to thank my friends and family who stood by me by listening to my problems and fears, relaxing and refreshing leisure activities and fortifying words.

In the end my biggest gratitude goes to the light of my life, Livia. You support me every day and build me up when I am fatigued after a long day of work. You give me the strength to go on when I am unmotivated and show me the right way when I am about to leave it. When I look at you, all sorrows of the day are forgotten and I can recover from the most strenuous day.

Thanks again to all of you.



# Appendix A

## ASDEX Upgrade

The data, on which this work is based on, are recorded at ASDEX Upgrade. It is a mid size tokamak in the divertor configuration [126]. It has a flexible shaping of the plasma and numerous systems for heating and current drive. Additionally it has a large number of diagnostics to measure a wide variety of plasma parameters. Goal of the research is the clarification of fundamental plasma physical questions and the preparation of ITER [19]. For that reason the research is focussed on transport phenomena, MHD stability and the physics of fast particles.

Another important feature of this plasma experiment is the gapless coverage of the first wall with tungsten since 2007. This allows the investigation of tungsten as high  $Z$  material under ITER relevant conditions. This is a required step since a pure carbon wall cannot be used in a fusion reactor due to its fast erosion and its tendency to retain Tritium.

A schematic representation of the plasma experiment ASDEX Upgrade can be seen in Fig. A.1.

## APPENDIX A. ASDEX UPGRADE

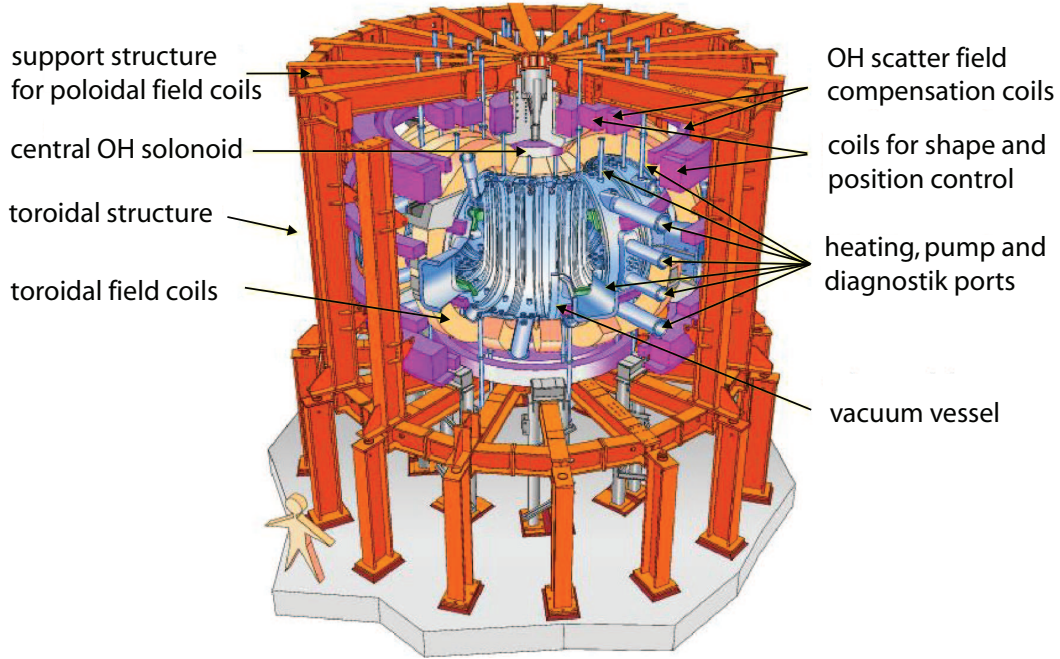


**Figure A.1:** Schematic representation of the tokamak ASDEX Upgrade [127].

General parameters of ASDEX Upgrade are summarised in the following table [127]:

Large plasma radius	$R_0$	1,65 m
Small horizontal plasma radius	$a$	0,5 m
Small vertical plasma radius	$b$	0,8 m
Elongation of plasma	$\kappa = \frac{b}{a}$	1,6
Triangularity	$\delta$	0.4
Aspect ratio	$A = \frac{R}{a}$	3,3
Kind of plasma		Hydrogen, deuterium, helium
Mass of plasma		3 mg
Volume of plasma	$V$	14 m <sup>3</sup>
Plasma current	$I_p$	$\leq 1,6$ MA
Toroidal magnetic field	$B_t$	$\leq 3,9$ T
Heating powers	$P_{aux, total}$	$\leq 27$ MW
	$P_{NBI}$	$\leq 20$ MW
	$P_{ICRH}$	$\leq 5$ MW
	$P_{ECRH}$	$\leq 5,5$ MW
Electron temperature	$T_e$	$\leq 4,0$ keV
Plasma pressure	$\beta_N$	$\leq 5,2$ ; stationary: 3
Duration of discharge	$t$	$\leq 10$ s
Fusion power	$P_{fus}$	$\leq 50$ kW

## Appendix B

### Torbeam graphical user interface

For a more convenient use of the Torbeam code, a graphical user interface (GUI) was developed and optimised during this work, named `tb_gui`. It provides in an easy way the possibility to load the necessary experimental data such as equilibrium, electron temperature profile, electron density profile and ECRH launching parameters from the shotfile system. The programme allows to load and to scale all experimental input data from an individual user specified discharge, time point, shotfile edition or file. The electron density and temperature profiles can be made available by a polynomial. Moreover, a spline-fit of the experimental data was implemented. Additionally all parameters of the ECRH systems such as injection angle, power or heating mode can be changed by direct input or configuration file. These measures allow the calculation of discharges with missing input data as well as the design of discharges with specifically tailored heating power and current drive deposition profiles. After calling the actual computation routine Torbeam [48] the GUI also is equipped with modules to visualise and to store the results of the calculation in various formats for further use either for a single gyrotron or as sum of multiple gyrotrons. The plot routines include the display of the injected power and driven current profiles against  $\rho_{tor}$ ,  $\rho_{pol}$  and the minor radius. The poloidal and toroidal beam paths and absorption areas can be also plotted. The data can be stored as Torbeam specific t-files or u-files used by TRANSP and ASTRA. In addition the beam paths can be exported to load in `augddd` [128], a 3D viewing programme of the vessel of ASDEX Upgrade, and `diaggeom` the corresponding 2D implementation. The programme is now routinely used for discharge design and analysis at the Max-Planck-Institut für Plasmaphysik Garching, Germany.



# Appendix C

## Bibliography

- [1] United Nations. Population challenges and development goals. [ST/ESA/SER.A/248](#), 2005.
- [2] The Geological Society. Climate change: evidence from the geological record. Available online at <http://www.geolsoc.org.uk/climatechange>, 19.08.2013.
- [3] D. Bodansky. The status of nuclear waste disposal. *The American Physical Society*, **35(1)**, 2006.
- [4] R. Anigstein, et al. Radiological assessments for clearance of material from nuclear facilities. *NUREG-Series Publications*, **1640(1)**, 2003.
- [5] OpenStax College. Binding energy. Available online at <http://cnx.org/content/m42640/latest/?collection=col11406/latest>, 03.05.2013.
- [6] J. Wesson. *Tokamaks*. Oxford Science Publications, Oxford, 1997.
- [7] C. Cavaller. Inertial fusion with the LMJ. *Plasma Physics and Controlled Fusion*, **47(12B):B389**, 2005.
- [8] J.D. Lindl, et al. Progress towards ignition on the National Ignition Facility. *Nuclear Fusion*, **51(9):094024**, 2011.
- [9] IPP Garching. ASDEX Upgrade website. Available online at <http://www.ipp.mpg.de/ippcms/eng/for/projekte/asdex/index.html>, 13.08.2013.
- [10] S. Günter. *Plasmaphysik und Fusionsforschung*. Lecture script, Garching, 2008.
- [11] U. Stroth. *Plasmaphysik*. Vieweg + Teubner, Wiesbaden, 2011.
- [12] G. Murtaza and H.U. Rahman. Thermal magnetic fluctuations and anomalous electron diffusion in a mirror-confined plasma. *Physical review A*, **28(3)**, 1983.

## APPENDIX C. BIBLIOGRAPHY

---

- [13] M. Sokoll. MHD-Instabilitäten in magnetisch eingeschlossenen Plasmen und ihre tomographische Rekonstruktion im Röntgenlicht. *Dissertation, TU-München, IPP, IPP report 1/309*, 1997.
- [14] P.W. Terry. Suppression of turbulence and transport by sheared flow. *Review of Modern Physics*, [72:109–165](#), 2000.
- [15] H. Zohm. Edge localized modes (ELMs). *Plasma Physics and Controlled Fusion*, [38\(2\):105](#), 1996.
- [16] A. Kallenbach, et al. Non-boronized compared with boronized operation of ASDEX Upgrade with full-tungsten plasma facing components. *Nuclear Fusion*, [49\(4\):045007](#), 2009.
- [17] M. Shimada, et al. Chapter 1: Overview and summary. *Nuclear Fusion*, [47\(6\):S1](#), 2007.
- [18] R. Aymar, P. Barabaschi, and Y. Shimomura. The ITER design. *Plasma Physics and Controlled Fusion*, [44\(5\):519](#), 2002.
- [19] ITER. General ITER website. Available online at <http://www.iter.org>, 21.11.2012.
- [20] H. Zohm. On the Minimum Size of DEMO. *Fusion Science and Technology*, [58\(2\):613–624](#), 2010.
- [21] P.B. Snyder, et al. Edge localized modes and the pedestal: A model based on coupled peeling–ballooning modes. *Physics of Plasmas*, [9\(5\):2037–2043](#), 2002.
- [22] H.R. Wilson, P.B. Snyder, G.T.A. Huysmans, and R.L. Miller. Numerical studies of edge localized instabilities in tokamaks. *Physics of Plasmas*, [9\(4\):1277–1286](#), 2002.
- [23] C.F. Maggi. Progress in understanding the physics of the H-mode pedestal and ELM dynamics. *Nuclear Fusion*, [50\(6\):066001](#), 2010.
- [24] M. Greenwald, et al. A new look at density limits in tokamaks. *Nuclear Fusion*, [28\(12\):2199](#), 1988.
- [25] P.T. Lang, et al. High-density H-mode operation by pellet injection and ELM mitigation with the new active in-vessel saddle coils in ASDEX Upgrade. *Nuclear Fusion*, [52\(2\):023017](#), 2012.
- [26] A. Manini, et al. Experimental study of electron heat transport in ion heated H-modes in ASDEX Upgrade. *Plasma Physics and Controlled Fusion*, [46\(11\):1723](#), 2004.
- [27] A. Manini, et al. Role of  $T_e/T_i$  and  $\nabla v_{tor}$  in ion heat transport of ASDEX Upgrade H-mode plasmas. *Nuclear Fusion*, [46\(12\):1047–1053](#), 2006.

- 
- [28] T.W. Versloot, et al. Comparison between dominant NB and dominant IC heated ELMy H-mode discharges in JET. *Nuclear Fusion*, [51\(10\):103033](#), 2011.
- [29] F. Wagner, et al. On the heating mix of ITER. *Plasma Physics and Controlled Fusion*, [52\(12\):124044](#), 2010.
- [30] C. Angioni, et al. Theory-based modeling of particle transport in ASDEX Upgrade H-mode plasmas, density peaking, anomalous pinch and collisionality. *Physics of Plasmas*, [10\(8\):3225–3239](#), 2003.
- [31] F. Wagner, et al. Regime of improved confinement and high beta in neutral-beam-heated divertor discharges of the ASDEX tokamak. *Physical Review Letters*, [49:1408–1412](#), 1982.
- [32] M.G. Dunne, et al. Measurement of neoclassically predicted edge current density at ASDEX Upgrade. *Nuclear Fusion*, [52\(12\):123014](#), 2012.
- [33] S. Coda, O. Sauter, M.A. Henderson, and T.P. Goodman. Steady-state, fully bootstrap-sustained discharges in the TCV tokamak. *34th EPS Conference on Plasma Physics*, [CRPP-CONF-2007-061](#), 2007.
- [34] A.C.C. Sips, for the steady state operation and the transport physics topical groups of the international tokamak physics activity. Advanced scenarios for ITER operation. *Plasma Physics and Controlled Fusion*, [47\(5A\):A19](#), 2005.
- [35] B. Coppi and F. Pegoraro. Theory of the ubiquitous mode. *Nuclear Fusion*, [17\(5\):969](#), 1977.
- [36] F. Romanelli. Ion temperature-gradient-driven modes and anomalous ion transport in tokamaks. *Physics of Plasmas*, [1:1018](#), 1989.
- [37] J. Weiland, A.B. Jarmén, and H. Nordman. Diffusive particle and heat pinch effects in toroidal plasmas. *Nuclear Fusion*, [29\(10\):1810](#), 1989.
- [38] B. Coppi and G. Rewoldt. New trapped-electron instability. *Physical Review Letters*, [33:1329–1332](#), 1974.
- [39] F. Jenko, W. Dorland, and G.W. Hammett. Critical gradient formula for toroidal electron temperature gradient modes. *Physics of Plasmas*, [8:4096](#), 2001.
- [40] P.C. Liewer. Measurements of microturbulence in tokamaks and comparisons with theories of turbulence and anomalous transport. *Nuclear Fusion*, [25\(5\):543](#), 1985.
- [41] F. Jenko, W. Dorland, and G. W. Hammett. Critical gradient formula for toroidal electron temperature gradient modes. *Physics of Plasmas*, [8\(9\):4096–4104](#), 2001.
- [42] C. Angioni, et al. Gyrokinetic modelling of electron and boron density profiles of H-mode plasmas in ASDEX Upgrade. *Nuclear Fusion*, [51\(2\):023006](#), 2011.

## APPENDIX C. BIBLIOGRAPHY

---

- [43] G. Pereverzev and P.N. Yushmanov. ASTRA Automated System for TRansport Analysis in a Tokamak. [IPP report 5/98](#), 2002.
- [44] A.A. Ivanov, R.R. Khayrutdinov, S.Yu. Medvedev, and Yu.Yu. Poshekhonov. New adaptive grid plasma evolution code SPIDER. *32th EPS Conference on Plasma Physics*, [29C:P5.063](#), 2005.
- [45] F. Ryter, et al. Electron heat transport studies. *Plasma Physics and Controlled Fusion*, [48\(12B\):B453](#), 2006.
- [46] P.J. Mc Carthy. Analytical solutions to the Grad–Shafranov equation for tokamak equilibrium with dissimilar source functions. *Physics of Plasmas*, [6\(9\):3554–3560](#), 1999.
- [47] P.J. Mc Carthy and ASDEX Upgrade Team. Identification of edge-localized moments of the current density profile in a tokamak equilibrium from external magnetic measurements. *Plasma Physics and Controlled Fusion*, [54\(1\):015010](#), 2012.
- [48] E. Poli, G.V. Pereverzev, and A.G. Peeters. Paraxial Gaussian wave beam propagation in an anisotropic inhomogeneous plasma. *Physics of Plasmas*, [6\(1\):5–11](#), 1999.
- [49] A. Pankin, D. McCune, R. Andre, G. Bateman, and A. Kritz. The tokamak Monte Carlo fast ion module NUBEAM in the National Transport Code Collaboration library. *Computer Physics Communications*, [159\(3\):157–184](#), 2004.
- [50] F. Porcelli, D. Boucher, and M.N. Rosenbluth. Model for the sawtooth period and amplitude. *Plasma Physics and Controlled Fusion*, [38\(12\):2163](#), 1996.
- [51] G.M. Staebler, J.E. Kinsey, and R.E. Waltz. Gyro-Landau fluid equations for trapped and passing particles. *Physics of Plasmas*, [12\(10\):102508](#), 2005.
- [52] G.M. Staebler, J.E. Kinsey, and R.E. Waltz. A theory-based transport model with comprehensive physics. *Physics of Plasmas*, [14\(5\):055909](#), 2007.
- [53] W.M. Tang, J.W. Connor, and R.J. Hastie. Kinetic-ballooning-mode theory in general geometry. *Nuclear Fusion*, [20\(11\):1439](#), 1980.
- [54] G.W. Hammett and F.W. Perkins. Fluid moment models for Landau damping with application to the ion-temperature-gradient instability. *Physical Review Letters*, [64:3019–3022](#), 1990.
- [55] R.E. Waltz, R.R. Dominguez, and G.W. Hammett. Gyro-Landau fluid models for toroidal geometry. *Physics of Fluids B: Plasma Physics*, [4\(10\):3138–3151](#), 1992.
- [56] W. Dorland and G.W. Hammett. Gyrofluid turbulence models with kinetic effects. *Physics of Fluids B: Plasma Physics*, [5\(3\):812–835](#), 1993.



- 
- [57] R.E. Waltz, G.D. Kerbel, J. Milovich, and G.W. Hammett. Advances in the simulation of toroidal gyro-Landau fluid model turbulence. *Physics of Plasmas*, 2(6):2408–2416, 1995.
- [58] M.A. Beer and G.W. Hammett. Toroidal gyrofluid equations for simulations of tokamak turbulence. *Physics of Plasmas*, 3(11):4046–4064, 1996.
- [59] M.A. Beer and G.W. Hammett. Bounce averaged trapped electron fluid equations for plasma turbulence. *Physics of Plasmas*, 3(11):4018–4022, 1996.
- [60] R.E. Waltz, et al. A gyro-Landau-fluid transport model. *Physics of Plasmas*, 4(7):2482–2496, 1997.
- [61] Jr.T.M. Antonsen and B. Lane. Kinetic equations for low frequency instabilities in inhomogeneous plasmas. *Physics of Fluids*, 23(6):1205–1214, 1980.
- [62] G.M. Staebler and J.E. Kinsey. Electron collisions in the trapped gyro-Landau fluid transport model. *Physics of Plasmas*, 17(12):122309, 2010.
- [63] J. Candy and R.E. Waltz. An Eulerian gyrokinetic-Maxwell solver. *Journal of Computational Physics*, 186(2):545–581, 2003.
- [64] M. Kotschenreuther, G. Rewoldt, and W.M. Tang. Comparison of initial value and eigenvalue codes for kinetic toroidal plasma instabilities. *Computer Physics Communications*, 88(2-3):128–140, 1995.
- [65] W. Dorland, F. Jenko, M. Kotschenreuther, and B.N. Rogers. Electron Temperature Gradient Turbulence. *Physical Review Letters*, 85:5579–5582, 2000.
- [66] X.Q. Xu. Tokamak drift-wave instabilities (ITG, ETG, CTEM): nonlinear theory & simulations. *Chinese Summer School on Plasma Physics*, Lawrence Livermore National Laboratory, 2009.
- [67] B. Streibl, P.T. Lang, F. Leuterer, Jean-Marie Noterdaeme, and A. Stabler. Chapter 2: Machine design, fueling, and heating in ASDEX upgrade. *Fusion science and technology*, 44(3):578–592, 2003.
- [68] H. Faugel, et al. The ASDEX Upgrade ICRF system: Operational experience and developments. *Fusion engineering and design*, 74(1-4):319–324, 2005.
- [69] J. Stober, et al. ECRH on ASDEX Upgrade - system status, feed-back control, plasma physics results. *EPJ Web of Conferences*, 32:02011, 2012.
- [70] PPPL. TRANSP website. Available online at <http://w3.pppl.gov/transp>, 26.04.2013.
- [71] R.J. Hawryluk. An empirical approach to tokamak transport. *Physics of Plasmas close to thermonuclear conditions*, 1:19–46, 1980.

## APPENDIX C. BIBLIOGRAPHY

---

- [72] J. Ongena, M. Evrard, and D. McCune. Numerical transport codes. *Transactions of Fusion Technology*, 33(2), 1998. Proceedings of the Third Carolus Magnus Summer School on Plasma Physics, (Spa, Belgium, Sept. 1997).
- [73] R. Bilato, et al. Simulations of combined neutral beam injection and ion cyclotron heating with the TORIC-SSFPQL package. *Nuclear Fusion*, 51(10):103034, 2011.
- [74] R. Bilato, M. Brambilla, D.A. Hartmann, and A. Parisot. Influence of an evanescence layer in front of the antenna on the coupling efficiency of ion cyclotron waves. *Nuclear Fusion*, 45(2):L5, 2005.
- [75] M.L. Mayoral, et al. On maximizing the ICRF antenna loading for ITER plasmas. *23rd IAEA Fusion Energy Conference*, ITR/P1-11:1–8, 2010.
- [76] V. Bobkov, et al. ICRF operation with improved antennas in ASDEX Upgrade with W wall. *Nuclear Fusion*, 53(9):093018, 2013.
- [77] R. Bilato and R. Kleiber. *Skript IPP Summer University for Plasma Physics*. Max-Planck-Institut für Plasmaphysik, Garching, 2012.
- [78] M. Brambilla. Numerical simulation of ion cyclotron waves in tokamak plasmas. *Plasma Physics and Controlled Fusion*, 41(1):1, 1999.
- [79] R. Prater. Heating and current drive by electron cyclotron waves. *Physics of Plasmas*, 11(5):2349–2376, 2004.
- [80] M. Seki M. Sawahata M. Terakadoand T. Fujii T. Kobayashi, S. Moriyama. Achievement of 1.5 MW, 1 s oscillation by the JT-60U gyrotron. *Plasma and Fusion Research*, 3(014):1–3, 2008.
- [81] M. Thumm, W. Kasperek, D. Wagner, and A. Wien. Reflection of modes at open-ended oversized circular waveguide. *Antennas and Propagation, IEEE Transactions on*, 61(5):2449–2456, 2013.
- [82] D. Wagner, et al. Status of the new multi-frequency ECRH system for ASDEX Upgrade. *Nuclear Fusion*, 48(5):054006, 2008.
- [83] S.N. Vlasov and I.M. Orlova. Quasi-optical transformer which transforms the waves in a waveguide having a circular cross-section into a highly-directional wave beam. *Radio Physics and Quantum Electronics*, 17:115–119, 1974.
- [84] S.N. Vlasov, L.I. Zagryadskaya, and M.I. Petelin. Transformation of a whispering gallery mode, propagating in a circular waveguide into beam of waves. *Radio Engineering and Electron Physics*, 20:14–17, 1975.
- [85] M. Thumm. Development of output windows for high-power long-pulse gyrotrons and EC wave applications. *International Journal of Infrared and Millimeter Waves*, 19:3–14, 1998.

- 
- [86] K. Sakamoto, A. Kasugai, M. Tsuneoka, and et al. *Proceedings of the 10th Joint Workshop on Electron Cyclotron Emission and Electron Cyclotron Heating*, page 463, 1997. Ameland, Netherlands, edited by T. Donne and T. Verhoeven.
- [87] D. Wagner, et al. Feed forward polarization control during ECRH discharges at ASDEX Upgrade. *Fusion Science and Technology*, [58\(2\):658–665](#), 2010.
- [88] M. Schubert, et al. Monitoring millimeter wave stray radiation during ECRH operation at ASDEX Upgrade. *EPJ Web of Conferences*, [32:02013](#), 2012.
- [89] M. Reich, A. Bock, M. Maraschek, and ASDEX Upgrade Team. NTM localization by correlation of Te and dB/dt. *Fusion Science and Technology*, [61\(4\):309–313](#), 2012.
- [90] F. Ryter, R. Dux, P. Mantica, and T. Tala. Perturbative studies of transport phenomena in fusion devices. *Plasma Physics and Controlled Fusion*, [52\(12\):124043](#), 2010.
- [91] A. Lorenz. ASDEX Upgrade database/vacuum vessel system. *Max-Planck-Institut für Plasmaphysik*, [page 1](#), 2004.
- [92] F. Leuterer, et al. Operation Experience with the ASDEX Upgrade ECRH System. *Fusion Science and Technology*, [55\(1\):31–44](#), 2009.
- [93] S. K. Rathgeber, et al. Estimation of edge electron temperature profiles via forward modelling of the electron cyclotron radiation transport at asdex upgrade. *Plasma Physics and Controlled Fusion*, [55\(2\):025004](#), 2013.
- [94] J. Boom. Characterization of edge localized modes in tokamak plasmas. *Dissertation*, [IPP report 10/47](#), 2012.
- [95] H. Murmann, S. Götsch, H. Röhr, H. Salzmann, and K.H. Steuer. The Thomson scattering systems of the ASDEX upgrade tokamak. *Review of Scientific Instruments*, [63\(10\):4941–4943](#), 1992.
- [96] B. Kurzan and H. D. Murmann. Edge and core Thomson scattering systems and their calibration on the ASDEX Upgrade tokamak. *Review of Scientific Instruments*, [82\(10\):103501](#), 2011.
- [97] E. Viezzer, T. Pütterich, R. Dux, R.M. McDermott, and ASDEX Upgrade Team. High-resolution charge exchange measurements at asdex upgrade. *Review of Scientific Instruments*, [83\(10\):103501](#), 2012.
- [98] R.M. McDermott, et al. Core momentum and particle transport studies in the ASDEX Upgrade tokamak. *Plasma Physics and Controlled Fusion*, [53\(12\):124013](#), 2011.
- [99] M. Willensdorfer, et al. Improved chopping of a lithium beam for plasma edge diagnostic at ASDEX Upgrade. *Review of Scientific Instruments*, [83\(2\):023501](#), 2012.

## APPENDIX C. BIBLIOGRAPHY

---

- [100] E. Wolfrum, et al. Fast lithium-beam spectroscopy of tokamak edge plasmas. *Review of Scientific Instruments*, [64\(8\):2285–2292](#), 1993.
- [101] A. Mlynek, et al. Design of a digital multiradian phase detector and its application in fusion plasma interferometry. *Review of Scientific Instruments*, [81\(3\):033507](#), 2010.
- [102] A. Burckhart J.C. Fuchs L. Giannone A. Kallenbach R.M. McDermott B. Sieglin ASDEX Upgrade Team M. Bernert, T. Eich. Bolometry with AXUV diodes at ASDEX Upgrade. *Review of Scientific Instruments*, [submitted](#), 2013.
- [103] K.F. Mast, et al. A low noise highly integrated bolometer array for absolute measurement of vuv and soft x radiation. *Review of Scientific Instruments*, [62\(3\):744–750](#), 1991.
- [104] M. Bernert. Personal communication. 22.08.2013.
- [105] R. Fischer, et al. Integrated Data Analysis of Profile Diagnostics at ASDEX Upgrade. *Fusion Science and Technology*, [58\(2\):675–684](#), 2010.
- [106] F. Sommer, et al. H-mode characterization for dominant ECRH and comparison to dominant NBI and ICRF heating at ASDEX Upgrade. *Nuclear Fusion*, [52\(11\):114018](#), 2012.
- [107] J. Stober, et al. Dominant ECR heating of H-mode plasmas on ASDEX Upgrade using the upgraded ECRH system and comparison to dominant NBI or ICRF heating. *24rd IAEA Fusion Energy Conference*, [IAEA-CN-197, EX/1-4](#), 2012.
- [108] F. Sommer, et al. H-mode characterization for dominant ECRH and comparison to dominant NBI or ICRF heating at ASDEX Upgrade. *RFPPC Conference*, 2013. submitted to AIP.
- [109] R. Neu, et al. Impurity behaviour in the ASDEX Upgrade divertor tokamak with large area tungsten walls. *Plasma Physics and Controlled Fusion*, [44\(6\):811](#), 2002.
- [110] D.P. Schissel, M.A. Mahdavi, J.C. DeBoo, and M. Le. Decoupling the effects of plasma current and plasma density on DIII-D H mode energy confinement. *Nuclear Fusion*, [34\(10\):1401](#), 1994.
- [111] F. Ryter, et al. H-mode threshold and confinement in helium and deuterium in ASDEX Upgrade. *Nuclear Fusion*, [49\(6\):062003](#), 2009.
- [112] A. Mlynek. Real-time control of the plasma density profile on ASDEX Upgrade. *Ludwig-Maximilians-Universität München*, [Dissertation](#), 2010.
- [113] C. Angioni, et al. Intrinsic toroidal rotation, density peaking, and turbulence regimes in the core of tokamak plasmas. *Physical Review Letters*, [107:215003](#), 2011.

- 
- [114] T. Pütterich, E. Wolfrum, R. Dux, and C.F. Maggi. Evidence for strong inversed shear of toroidal rotation at the edge-transport barrier in the ASDEX Upgrade. *Physical Review Letters*, [102:025001](#), 2009.
- [115] P. Mantica, et al. Investigation of electron heat pinch in ASDEX-Upgrade. *Plasma Physics and Controlled Fusion*, [48\(3\):385](#), 2006.
- [116] X. Garbet, et al. Turbulent fluxes and entropy production rate. *Physics of Plasmas*, [12\(8\):082511](#), 2005.
- [117] E. Viezzer, et al. High-accuracy characterization of the edge radial electric field at ASDEX Upgrade. *Nuclear Fusion*, [53\(5\):053005](#), 2013.
- [118] W.M. Stacey. A neoclassical model for toroidal rotation and the radial electric field in the edge pedestal. *Physics of Plasmas*, [11\(6\):3096–3099](#), 2004.
- [119] W.A. Houlberg, K. C. Shaing, S. P. Hirshman, and M. C. Zarnstorff. Bootstrap current and neoclassical transport in tokamaks of arbitrary collisionality and aspect ratio. *Physics of Plasmas*, [4\(9\):3230–3242](#), 1997.
- [120] S.P. Hirshman and D.J. Sigmar. Neoclassical transport of impurities in tokamak plasmas. *Nuclear Fusion*, [21\(9\):1079](#), 1981.
- [121] C. Angioni. Personal communication. 22.08.2013.
- [122] T. Görler and F. Jenko. Multiscale features of density and frequency spectra from nonlinear gyrokinetics. *Physics of Plasmas*, [15\(10\):102508](#), October 2008.
- [123] T. Görler and F. Jenko. Scale Separation between Electron and Ion Thermal Transport. *Physical Review Letters*, [100\(18\):185002](#), May 2008.
- [124] R.V. Budny, et al. Predictions of H-mode performance in ITER. *Nuclear Fusion*, [48\(7\):075005](#), 2008.
- [125] R.V. Budny, et al. PTRANSP tests of TGLF and predictions for ITER. *Submitted to: Proceedings of the 24th IAEA Fusion Energy Conference*, [EFDA-JET-CP\(12\)06/10](#), 2012.
- [126] H. Zohm, et al. Overview of ASDEX Upgrade results. *Nucl. Fusion*, [49\(10\):104009](#), 2009.
- [127] IPP Garching. ASDEX Upgrade parameters. Available online at <https://www.aug.ipp.mpg.de/wwwaug>, 13.08.2013.
- [128] T. Lunt, et al. A new 3D viewer as an interface between the ASDEX Upgrade CAD models and data from plasma modelling and experiment. *Nuclear Instruments and Methods in Physics Research Section A: Accelerators, Spectrometers, Detectors and Associated Equipment*, [623\(2\):812 – 814](#), 2010.

## APPENDIX C. BIBLIOGRAPHY

---

# Appendix D

## Abbreviations

ASDEX Upgrade	Axialsymmetrisches Divertor Experiment Upgrade
ASTRA	Automated system for transport analysis
AXUV	Absolute extreme ultraviolet
cw	Continuous wave
CXRS	Charge exchange recombination spectroscopy
DEMO	DEMONstration power plant
DCN	Deuterium cyanide laser for density measurement
ECCD	Electron cyclotron resonance current drive
ECE	Electron cyclotron resonance emission
ECRH	Electron Cyclotron resonance heating
ELM	Edge localised mode
EOC shape	Edge optimised shape
GLF	Gyro-Landau fluid equations
GUI	Graphical user interface
H-mode	High confinement mode
HFS	High field side
ICRH	Ion cyclotron resonance frequency heating
IDA	Integrated data analysis
ITER	International thermonuclear experimental reactor/Latin for "the way"
L-mode	Low confinement mode
LIB	Lithium beam emission spectroscopy
LFS	Low field side
LOS	Line of sight
MHD	Magneto hydrodynamic
NBI	Neutral beam injection

## APPENDIX D. ABBREVIATIONS

---

NW NBI	North west neutral beam injector (93 keV)
PFC	Plasma phasing component
SE NBI	South east neutral beam injector (60 keV)
SNR	Signal to noise ratio
SOL	Scrape off layer
tokamak	Toroidalnaja Kamera ss Magnitnimi Katuschkami Russian for toroidal chamber with magnetic coils
TGLF	Trapped gyro-Landau fluid transport model